Computational Methods for Medical Image Registration

by

Mia Carmela Mojica

A thesis submitted to the
School of Graduate and Postdoctoral Studies in partial
fulfillment of the requirements for the degree of

Doctor of Philosophy in Modelling and Computational Science

Faculty of Science
University of Ontario Institute of Technology (Ontario Tech University)

Oshawa, Ontario, Canada

April 2021

Thesis Title: Computational Methods for Medical Image Registration

An oral defense of this thesis took place on March 18, 2021 in front of the following examining committee:

Examining Committee:

Chair of Examining Committee	Dr. Lennaert Van Veen
Research Supervisor	Dr. Mehran Ebrahimi
Examining Committee Member	Dr. Sean Bohun
Examining Committee Member	Dr. Faisal Qureshi
Examining Committee Member	Dr. Mihaela Pop
University Examiner	Dr. Min Dong
External Examiner	Dr. João Sanches
	University of Lisbon, Portugal

The above committee determined that the thesis is acceptable in form and content and that a satisfactory knowledge of the field covered by the thesis was demonstrated by the candidate during an oral examination. A signed copy of the Certificate of Approval is available from the School of Graduate and Postdoctoral Studies.

Abstract

A significant amount of research has been dedicated to the improvement of techniques in the field of medical image analysis. Imaging modalities have been improved and new acquisition methods have been introduced to reveal greater anatomical detail and to allow for more information to be extracted from medical images. However, certain challenges remain when processing and analyzing information from medical images.

Image registration is a technique to find a reasonable transformation that best aligns a pair or group of images. Of particular interest in this thesis is the use of image registration in three main categories: cardiac fiber atlas construction from healthy porcine hearts, motion correction in contrast-enhanced image sequences, and the development of novel computational techniques that improve the performance of existing medical image registration methods.

We provide an overview of each of the problems that we tackled, followed by a discussion of the underlying motivation and theory behind the proposed methods, and extensive validations.

Most importantly, this work highlights the central role that image registration plays in biomedical research – from producing clinically relevant image-based predictive models, to enabling accurate diagnosis of diseases and the analysis of treatment response.

Keywords: image registration; cardiac fiber atlas; motion correction; landmark detection; contour matching

Author's Declaration

I hereby declare that this thesis consists of original work of which I have authored. This is a true copy of the thesis, including any required final revisions, as accepted by my examiners.

I authorize the University of Ontario Institute of Technology (Ontario Tech University) to lend this thesis to other institutions or individuals for the purpose of scholarly research. I further authorize University of Ontario Institute of Technology (Ontario Tech University) to reproduce this thesis by photocopying or by other means, in total or in part, at the request of other institutions or individuals for the purpose of scholarly research. I understand that my thesis will be made electronically available to the public.

_____   Mia Carmela Mojica

Statement of Contributions

I hereby declare that I performed the majority of the formulation of the models and methodologies, validation, and writing of the manuscript.

This thesis resulted in the following publications, abstracts, and presentations:

1. Part of the work described in Chapter 3 has been published and/or presented as

   (a) M. Mojica (*), M. Pop, M. Sermesant, and M. Ebrahimi. **Multilevel Non-Parametric Groupwise Registration in Cardiac MRI: Application to Explanted Porcine Hearts**. In: Lecture Notes in Computer Science, Proceedings of Statistical Atlases and Computational Modeling of the Heart (STACOM). Quebec City, Canada: Springer, Sept. 2017, pp. 60–69. [112]

   (b) M. Mojica (*), M. Pop, M. Sermesant, and M. Ebrahimi. **Groupwise Registration and Diffusion Tensor Reorientation in Cardiac MRI: Application to Explanted Porcine Hearts**. In: Imaging Network Ontario (ImNO) symposium. Toronto, Ontario, Canada, Mar. 2018.

   (c) M. Mojica (*), M. Pop, M. Sermesant, and M. Ebrahimi. **Constructing an Average Geometry and Diffusion Tensor Magnetic Resonance Field From Freshly Explanted Porcine Hearts**. In: Medical Imaging 2019: Image Processing, volume 10949, page 109493C. International Society for Optics and Photonics, 2019. https://doi.org/10.1117/12.2512870. [113]

   (d) M. Mojica (*), M. Pop, M. Sermesant, and M. Ebrahimi. **Novel Atlas of Fiber Directions Built From Ex Vivo DT images of Porcine Hearts**. Event: 27th International Society for Magnetic Resonance in Medicine (ISMRM) Annual Meeting and Exhibition, Montréal, Quebec, May 2019, 3 pages.

   (e) M. Mojica (*), M. Pop, M. Sermesant and M. Ebrahimi. **Mapping Out the Average Fiber Architecture from Diffusion Tensor MR Images of**

Ex-Vivo Porcine Hearts, International Congress on Industrial and Applied Mathematics, ICIAM, July 2019, Valencia, Spain. (Poster Presentation)

(f) M. Mojica (*), M. Pop, M. Sermesant, and M. Ebrahimi. **Novel Atlas of Fiber Directions From Ex-Vivo DT Images of Porcine Hearts**. In: Computer Methods and Programs in Biomedicine (CMPB) Vol. 187 (2020), 12 pages. [114]

2. Part of the work described in Chapter 4 has been published and/or presented as

(a) M. Mojica (*) and M. Ebrahimi. **An Unbiased Groupwise Registration Algorithm for Dynamic Contrast-Enhanced Magnetic Resonance Images**. In: Reconstruction and Analysis of Moving Body Organs (RAMBO) workshop of Medical Image Computing and Computer Assisted Intervention (MICCAI). Granada, Spain, Sept. 2018, 8 pages. [108]

(b) M. Mojica (*) and M. Ebrahimi. **Motion Correction in Dynamic Contrast-Enhanced Magnetic Resonance Images Using Pharmacokinetic Modeling**, SIAM Imaging Science, July 2020. (Poster Presentation)

(c) M. Mojica (*) and M. Ebrahimi. **Motion Correction in Dynamic Contrast-Enhanced Magnetic Resonance Images Using Pharmacokinetic Modeling**. In: Medical Imaging 2021: Image Processing, volume 11596, page 115962S. International Society for Optics and Photonics, 2021. https://doi.org/10.1117/12.2580973. [110]

3. Part of the work described in Chapter 5 has been presented as

M. Mojica (*) and M. Ebrahimi. **Combined Intensity- and Point-Based Cardiac Registration in the Presence of Landmark Errors**.
Event: Statistical Atlases and Computational Modeling of the Heart (STACOM) Workshop of MICCAI. Shenzhen, China, Oct. 2019, 11 pages.

4. Part of the work described in Chapter 6 has been published as

    M. Mojica (*), M. Pop, and M. Ebrahimi. **Automatic Detection of Landmarks for Fast Cardiac MR Registration**. In: Lecture Notes in Computer Science, Proceedings of Statistical Atlases and Computational Modeling of the Heart (STA-COM). Lima, Peru: Springer, Oct. 2020, pp. 87–96. [111]

5. Part of the work described in Chapter 7 has been published as

    M. Mojica (*) and M. Ebrahimi. **A Hybrid Landmark and Contour-Matching Image Registration Model**. In: Journal of Computational Vision and Imaging Systems, Nov. 2020, 4 pages. [109]

Acknowledgements

First of all, I would like to thank my supervisor, Dr. Mehran Ebrahimi, for his unending support and for his encouraging words. It is a privilege to work with a supervisor who cares so much about my work.

I wish to acknowledge Dr. Mihaela Pop of Sunnybrook Research Institute for providing the cardiac DTI data and for her thoughtful recommendations on this dissertation. I would also like to thank Dr. Maxime Sermesant of Inria for his valuable insights on the construction of the cardiac atlas.

I would like to acknowledge Dr. Anne Martel of Sunnybrook Research Institute for great discussions and providing the abdominal DCE-MRI data.

I would also like to express my gratitude to the members of my supervisory committee.

I owe my deepest gratitude to the Ontario Trillium Foundation, not only for providing the funding which allowed me to undertake this research, but also for giving me the opportunity to attend conferences and meet so many interesting people.

Finally, I would like to thank my friends and family for always believing in me!

Contents

List of Tables

List of Figures

List of Symbols

Symbol	Occurrence	Meaning
Ω	Chapter 2	Image domain
$\mathcal{R}$	Chapter 2	Reference image
$\mathcal{T}$	Chapter 2	Template image
$\mathcal{J}$	Chapter 2	Objective function for registration model
$\mathcal{D}$	Chapter 2	Dissimilarity/Distance measure
$\mathcal{S}$	Chapter 2	Regularization term
f	Chapter 2	Registration transformation
w	Chapter 2	Parameter vector for a parametric transformation
x^i	Chapter 2	i^{th} entry/component of a vector x
$\langle x, y \rangle$	Chapter 2	Inner product of vectors x and y
$\lVert \cdot \rVert$	Chapter 2	Euclidean/L^2-norm
$\nabla \mathcal{T}$	Chapter 2	Image gradient
$\nabla^2 f$ or H_f	Chapter 2	Hessian of a function f
$\Gamma(\cdot)$	Chapter 2	Gamma function
$\lfloor \cdot \rfloor$	Chapter 2	Greatest integer/floor function
$\mathcal{T}^l$	Chapter 2	l^{th}-level coarser/finer representation of an image $\mathcal{T}$
$\cup, \cap$	Chapter 2	Set union, set intersection
α	Chapter 2	Regularization parameter
d	Chapter 3	Diffusion coefficient
D_{tensor} or D	Chapter 3	Diffusion tensor
D'_{tensor} or D'	Chapter 3	Reoriented diffusion tensor
$\overline{D}$	Chapter 3	Mean diffusion tensor
$\lambda_1, \ \lambda_2, \ \lambda_3$	Chapter 3	Eigenvalues of a diffusion tensor
N	Chapter 3	Number of images in a dataset

Symbol	Occurrence	Meaning
f_{mean}^n	Chapter 3	Mean transformation at n^{th} iteration
n	Chapter 3	Groupwise iteration
$\mathcal{R}_{\mathrm{mean}}^n$	Chapter 3	Reference image at n^{th} iteration
$\mathcal{R}_{\mathrm{mean}}$	Chapter 3	Groupwise average/Final reference image
FA	Chapter 3	Fractional anisotropy
D	Chapter 4	Injected dose of contrast agent
C	Chapter 4	Gd-DTPA tissue concentration
$m_1,\ m_2$	Chapter 4	Rate constant/s of Gd-DTPA clearance
K^{trans}	Chapter 4	Transfer constant between blood plasma and tissue compartments
v_e	Chapter 4	Extracellular extravascular fraction
k_{ep}	Chapter 4	Ratio of K^{trans} to v_e
$\mathscr{L}(\alpha)$	Chapter 4	Sum of squared residuals at α
J_f	Chapter 4	Jacobian of function f
$\mathrm{diag}(A)$	Chapter 4	Diagonal matrix consisting of the diagonal entries of matrix A
$\Delta\mathrm{SI}$	Chapter 4	Signal intensity displacement
$v_s(x)$	Chapter 4	Smoothness measure for vector x
$\mathcal{T}_i$	Chapter 4	i^{th} frame in DCE image sequence
$\mathcal{T}_p$	Chapter 4	Image in the DCE sequence with highest average intensity
$\lVert\cdot\rVert_\infty$	Chapter 5	Infinity norm/L_∞-norm
$r_j,\ t_j$	Chapter 5	j^{th} (exact) reference and template landmarks
κ	Chapter 6	Curvature
$\rho = 1/\kappa$	Chapter 6	Radius of curvature
$\phi(x_k)$	Chapter 6	Narrowing/interior angle at k^{th} contour point x_k
$a \bmod b$	Chapter 6	Modulo operator; remainder when a is divided by b
N	Chapter 6	Cardinality of an edge/contour C
Δk	Chapter 6	Window size for computing narrowing at a contour point

Symbol	Occurrence	Meaning
R	Chapter 6	Roundedness/compactness measure
A	Chapter 6	Area of a segment
P	Chapter 6	Perimeter of a segment
$\mathcal{C}$	Chapter 7	Contour matching term
K	Chapter 7	Number of exact/major landmarks
L	Chapter 7	Number of contour-approximating landmarks
$\overset{*}{r}_j,\ \overset{*}{t}_j$	Chapter 7	j^{th} reference, template contour-approximating landmarks
$v[\overset{*}{x}_j]$	Chapter 7	Unit vector parallel to vector passing through consecutive contour-approximating landmarks $\overset{*}{x}_j$ and $\overset{*}{x}_{j+1}$

Chapter 1

Introduction

A significant amount of research has been dedicated to the improvement of techniques in the field of medical imaging. Imaging modalities have been improved and new acquisition methods have been introduced to reveal greater anatomical detail and to allow for more information to be extracted from medical images. However, certain challenges remain when processing and analyzing information from medical images. In this thesis, we aim to use image registration as a tool to address some of these challenges.

Image registration is a technique that seeks to find a reasonable transformation that geometrically deforms a moving image and aligns it to a fixed image [106]. It has numerous applications especially in the field of medical imaging. For instance, it can be used to analyze the motion in body tissues and aid in surgical planning when the location of a region of interest (ROI) in the pre-surgical magnetic resonance scan of a patient changes during surgery due to different patient positions or other physiological processes. Provided that the alignment process is done correctly, image registration can be used to accurately pinpoint the location of a tumor, allowing for a minimally invasive surgical incision [144].

Image registration is also used as a pre-processing tool in the analysis of tumor heterogeneity. Eliminating motion in a sequence of images acquired before and after the administration of a contrast agent is a necessary first step in pharmacokinetic analysis, which uses the dynamics of concentration curves to reveal information about the underlying tumor biology. Image registration has been demonstrated to be effective in obtaining a motionless dataset from a sequence of dynamic contrast-enhanced magnetic resonance (DCE-MR) images and, thus, is vital in understanding the possible response and resistance of tumors to cancer therapies [83].

New imaging techniques that add more dimension to existing modalities also require registration to produce clinically relevant image-based models. Consider, for instance, the MR acquisition technique called diffusion-weighted (DW) imaging [57]. DW images are a set of MR images sensitized with different diffusion-encoding gradients to reveal information about the diffusion pattern of water molecules. Currently, there are ongoing efforts to construct statistical atlases for various anatomies which seek to provide quantitative representations of variability in anatomical structures and functions, as well as models against which similar anatomies with possible abnormalities may be compared. Image registration plays a key role in spatially normalizing anatomical information from different subjects.

Our goal in this research is to come up with novel registration methods for the following problems in medical image analysis:

1. **Intensity-based inter-subject registration**

    Inter-subject image registration involves the spatial alignment of images from different patients or species. This is the starting point for the construction of atlases, which entails the registration of groups of images to build an average geometry. Atlases enable the statistical analysis of anatomical shapes [157]. Here, we discuss a classical intensity-based groupwise registration framework for building an anatomical model [55, 64, 129]. More specifically, we demonstrate its usefulness in understanding cardiac function by building a cardiac fiber atlas from *ex-vivo* diffusion-weighted images of healthy porcine hearts.

    Cardiovascular disease continues to be the leading cause of death, accounting for 30% of mortality worldwide [1]. There has been an increasing demand to understand the mechanical and electrical activities of the heart through the construction of atlases that model healthy hearts, against which pathological hearts can be compared. However, the availability of explanted human hearts is scarce. Thus, studying large hearts (e.g. canine and pig hearts) could provide a good alternative

as the cardiac anatomies and functions of the three species are very similar.

Nowadays, most translational cardiovascular experiments and simulation-based predictive modelling are carried out using porcine models. This motivates us to develop the first high-resolution diffusion tensor imaging-based porcine fiber atlas through groupwise registration. Cardiac fiber atlases could be beneficial for various preclinical studies, ranging from disease assessment to electro-mechanical simulations.

2. **Intensity-based intra-subject registration of DCE-MR images**

We then turn our focus to the alignment of multiple images of the same subject taken at different times. When applied to DCE image sequences, intra-subject registration could facilitate the accurate analysis of contrast-enhancement curves, and consequently shed light onto the underlying tissue or tumor vasculature.

Brought about by the uptake of the contrast agent and different tissue response properties, structures in DCE images that would typically be used to guide image registration could exhibit varying intensities at different frames in the sequence. This implies that some of the commonly used image similarity measures would not be applicable when aligning pairs of DCE images. We will address this challenge by

(a) coming up with registration methods that can cater to intensity differences between contrast-enhanced images and to extend such methods to correct motion in a sequence of contrast-enhanced images.

(b) including pharmacokinetic modelling in the image registration problem. Specifically, we will use pharmacokinetic modelling to generate a sequence of synthetic reference images from the starting DCE sequence, with each synthetic image mimicking the expected overall signal intensity of a motionless reference at different stages in the absorption process. Generating such a sequence eliminates the issue of aligning features between pairs of images that exhibit

different signal intensities.

3. **Improvement of Landmark-Based Registration of Medical Imaging Data**

   We will also address some of the challenges that are associated with handling medical data that involve landmark information by proposing

   (a) Hybrid landmark- and intensity-based registration

   The lack of sufficient landmark information and the presence of landmark localization errors in some medical data is sometimes unavoidable. To mitigate this problem, we introduce a combined intensity- and landmark-based registration method that seeks to maximize the post-registration overlap between the reference and transformed template images. Utilizing additional intensity information serves to improve the image similarity away from defined landmarks and in areas where misregistration could result due to landmark localization errors.

   (b) Automatic landmark detection for fast registration

   Landmark-based registration of medical images can be challenging and prone to errors since the selection of landmarks highly depends on the ability of the physician to mentally integrate information from different images [97]. In addition, some medical images like the heart only has few spatially accurate and repeatable anatomical landmarks to guide the transformations [129]. Landmarks are typically aligned only as a pre-registration step. Intensity information is then employed to handle large deformations and further increase image overlap.

   However, even with these hybrid techniques, minimizing the amount of misregistration can still be tricky. For this, we propose a method to automatically detect landmarks for fast registration. These landmarks will allow the partitioning of the contour traced by an image edge and the identification of an

ordered set of contour-tracing landmarks. The proposed landmark detection method reduces the need for an expert to manually delineate points of interest landmarks and the possible introduction of landmark localization errors. On the other hand, obtaining equally-spaced points along the edges of the hearts allows us to approximate their contours.

(c) Landmark- and contour-based registration

Following the introduction of a landmark detection scheme, our next aim is to introduce a novel registration model that uses landmark and contour information to boost image similarity between the reference and transformed template. We will demonstrate that the model addresses some issues associated with point-based registration methods, more specifically the Thin Plate Spline technique [175, 35, 17]. In addition, we will also show that, similar to the hybrid registration method, this landmark- and contour-matching model (LCM) also provides accurate registration results even in the presence of landmark localization errors.

This thesis is organized as follows. In Chapter 2, we discuss the registration problem and the computational components necessary to solve one. The chapter also covers different types of local and global transformations used to align medical data with landmark information.

Here, we prioritize registration accuracy over computational efficiency. In order to avoid the issues associated with landmark-based registration (Chapter 2), we opted to use intensity-based registration methods as the starting point for inter- and intra-subject registration. We will address the issues associated with landmark-based registration in the latter chapters.

Chapters 3 and 4 revolve around intensity-based registration for medical applications. In particular, Chapter 3 tackles the inter-subject registration of explanted porcine hearts for constructing a cardiac fiber atlas. Chapter 4 explores multi-temporal intra-subject

```
┌─────────────────────────────────┐          ┌──────────────────────┐
│   Medical Image Registration    │          │  Image-Based (Car-   │
└─────────────────────────────────┘          │  diac) Models (Ch.3) │
                                              └──────────────────────┘
  ┌──────────────┐        ┌──────────────────┐
  │  Landmark-   │        │    Intensity-    │
  │ Based (Ch.2) │        │ Based (Ch.3,4)   │
  └──────────────┘        └──────────────────┘
                                              ┌──────────────────────┐
        ┌──────────────────────────┐          │ Motion Correction    │
        │   Hybrid LM- and Int.-   │          │      (Ch.4)          │
        │ Based Registration (Ch.5)│          └──────────────────────┘
        └──────────────────────────┘
        ┌──────────────────────────┐
        │    Automatic Interest    │
        │  Point Detection (Ch. 6) │
        └──────────────────────────┘
        ┌──────────────────────────┐
        │  Landmark- and Contour-  │
        │ Based Registration (Ch. 7)│
        └──────────────────────────┘
```
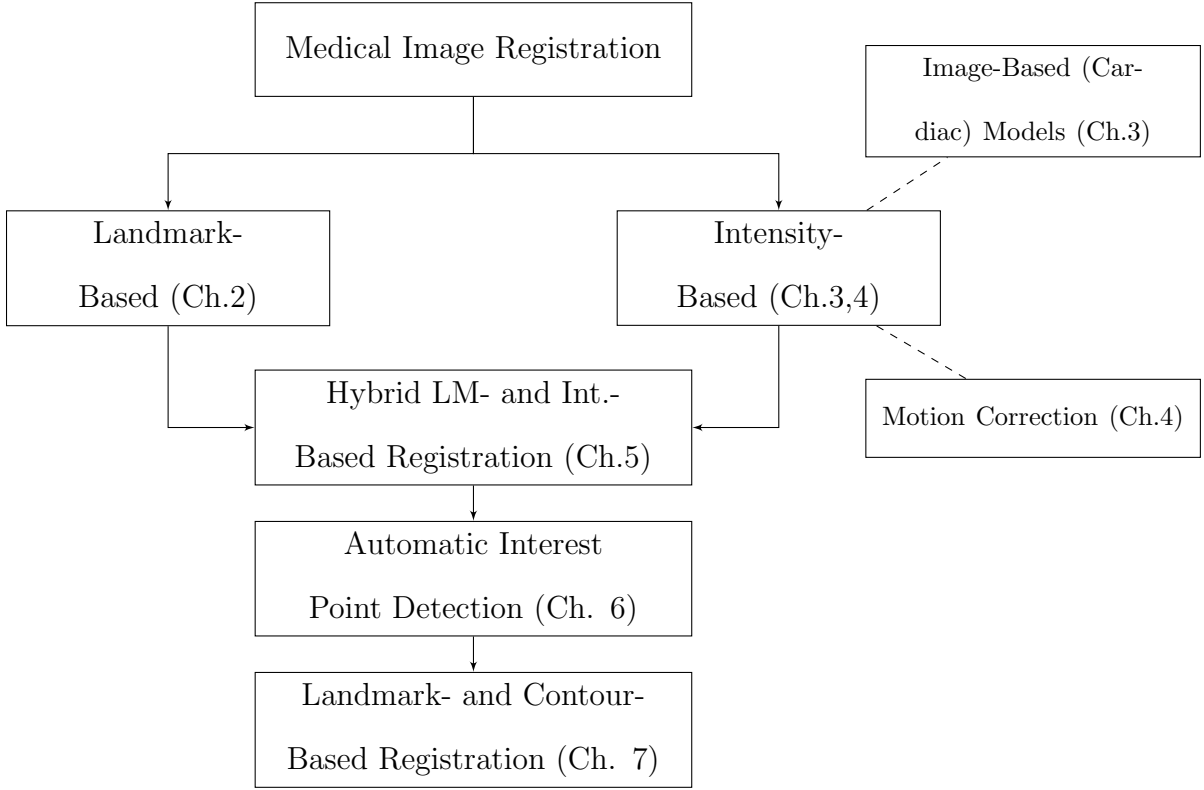
Figure 1.1: Organization of the thesis. Chapter 2: Image registration preliminaries; Chapter 3: Intensity-based inter-subject registration and its application to building image-based models; Chapter 4: Intensity-based intra-subject DCE registration for motion correction; Chapter 5: Hybrid landmark- and intensity-based registration; Chapter 6: Automatic detection of feature points and approximate contour information; Chapter 7: Registration Model for Landmark- and Contour-Matching.

registration and its role in eliminating motion within DCE sequences. We will present two novel registration methods for obtaining a motion-corrected dataset.

Chapter 5 reiterates the issues associated with handling medical data that involve landmark information and the need for more robust approaches that maximize image similarity between registered images. We will propose a hybrid landmark- and intensity-based registration model that addresses some of these issues.

In Chapter 6, an automatic interest point detection method will be presented. This serves two purposes. The first is to reduce the need for defining landmarks manually,

thereby reducing the possibility of introducing localization errors in the data. The automatic detection of feature points also supplies additional structural information – both exact and approximate – that could further guide the alignment process and allow the use of a computationally efficient registration model.

Finally, data generated from the implementation of the aforementioned interest point detection method will be used in the setup of a novel landmark- and contour-matching model, which we will introduce in Chapter 7. This model is designed to increase the flexibility of traditional landmark-based methods, is computationally efficient, and most importantly, provides accurate registration results comparable to those of intensity-based methods. We will validate the LCM model on 2D medical images and also discuss how to extend it to accommodate 3D cardiac images.

A diagram depicting the organization of this thesis is provided in Figure 1.1.

Chapter 2

Preliminaries

Image registration is the process of aligning a template or moving image to a fixed image, also called the reference image. It has applications in the fields of astronomy, cartography, art, and medicine, among others [107]. In this section, we discuss image registration in detail and present the required components to solve an image registration problem.

2.1   Image Registration

Given a template image $\mathcal{T} : \Omega \subset \mathbb{R}^n \to \mathbb{R}$ and a reference image $\mathcal{R} : \Omega \subset \mathbb{R}^n \to \mathbb{R}$, we wish to find a reasonable transformation such that a transformed version of the template $\mathcal{T}$ is similar to the reference $\mathcal{R}$ [107]. Mathematically, this can be modelled by solving the optimization problem

$$\min_f \mathcal{J}\left[f\right] = \min_f \mathcal{D}\left[\mathcal{T}\left[f\right], \mathcal{R}\right] + \mathcal{S}\left[f\right], \tag{2.1}$$

where $f : \Omega \to \mathbb{R}^n$ is the transformation that registers $\mathcal{T}$ to $\mathcal{R}$, and $\mathcal{T}\left[f\right]$ is a transformed version of the template image $\mathcal{T}$ under the transformation f.

The first term $\mathcal{D}$ in the joint functional $\mathcal{J}$ is called the distance measure. It measures the level of alignment between the two images and thus helps determine if there is a reasonable match between the image features. The second term $\mathcal{S}$ is the regularization term. It serves to provide additional information to help with the selection of the optimal solution.

2.2   Interpolation

Intensity values on the original template image $\mathcal{T}$ are typically defined on a uniform grid. Interpolation is required in order to deform a template image given a transformation and

its associated displacement field.

Widely used image interpolation methods include the nearest neighbor, bilinear, cubic, and spline interpolation. Each method has its own advantages and drawbacks in terms of ease-of-use, computational complexity, and accuracy. A detailed listing and discussion of the image interpolation methods mentioned above can be found in [107].

2.3 Intensity-Based Registration

2.3.1 Transformations

Since the goal in image registration is to find the optimal transformation mapping the template to the reference image, we need to be able to parametrize the optimal transformation f based on the original grid x in order to describe exactly where each point on the original grid of the template image is mapped under said transformation, and interpolate the intensity values of the template image on the transformed grid. That is, we wish to express f in terms of functions f of parameters w and basis functions Q such that

$$f = Q(x)f(w).$$

1. Translations. Translations describe horizontal and/or vertical shifts of an image. Consider a point $x = [x^1; x^2] \in \mathbb{R}^2$. A translation $f = [f^1; f^2]$ of x may be denoted by

$$f^1 = x^1 + w_1 \quad \text{and} \quad f^2 = x^2 + w_2. \tag{2.2}$$

More compactly, we can represent a 2D translation f as

$$f = x + Q(x)w, \quad \text{with} \quad Q(x) = \begin{bmatrix} 1 & 0 \\ 0 & 1 \end{bmatrix}. \tag{2.3}$$

2. Rotations. A counterclockwise rotation of w radians in $\mathbb{R}^2$ is represented by the transformation matrix

$$R = \begin{bmatrix} \cos w & -\sin w \\ \sin w & \cos w \end{bmatrix}. \tag{2.4}$$

It then follows that under this transformation, a point $x = [x^1; x^2] \in \mathbb{R}^2$ gets mapped to $f = Rx$.

3. Rigid Transformations. Rigid transformations are composed of rotations and translations. 2D rigid transformations can be expressed as

$$\begin{aligned} f^1 &= \cos(w_1)x^1 - \sin(w_1)x^2 + w_2 \\ f^2 &= \sin(w_1)x^1 + \cos(w_1)x^2 + w_3 \end{aligned}. \tag{2.5}$$

4. Shearing. Shearing refers to a push or a displacement of a point in a fixed direction by an amount proportional to its signed distance from a line that is parallel to that direction [178]. For instance, a shearing in the x^1-direction is given by

$$\begin{bmatrix} f^1 \\ f^2 \end{bmatrix} = \begin{bmatrix} 1 & 1 \\ 0 & 1 \end{bmatrix} \begin{bmatrix} x^1 \\ x^2 \end{bmatrix} = \begin{bmatrix} x^1 + x^2 \\ x^2 \end{bmatrix}. \tag{2.6}$$

5. Affine Linear Transformations. An affine linear transformation allows for rotation, shearing, and individual scaling [107]. Parallelism is preserved by affne transformations. In $\mathbb{R}^2$, affine transformations are parametrized as

$$\begin{aligned} f^1 &= w_1 x^1 + w_2 x^2 + w_3 \\ f^2 &= w_4 x^1 + w_5 x^2 + w_6 \end{aligned}. \tag{2.7}$$

As such, the above parametrization can be rewritten as $f = Q(x)w$, with

$$Q(x) = \begin{bmatrix} x^1 & x^2 & 1 & 0 & 0 & 0 \\ 0 & 0 & 0 & x^1 & x^2 & 1 \end{bmatrix} \tag{2.8}$$

and $w = [w_1, \ldots, w_6]^\mathrm{T}$.

Examples of parametric transformations applied to a hand Xray image from [4, 107] are shown in Figure 2.1.

| (a) Hand Xray | (b) Translation | (c) Rotation | (d) Horizontal Shear |
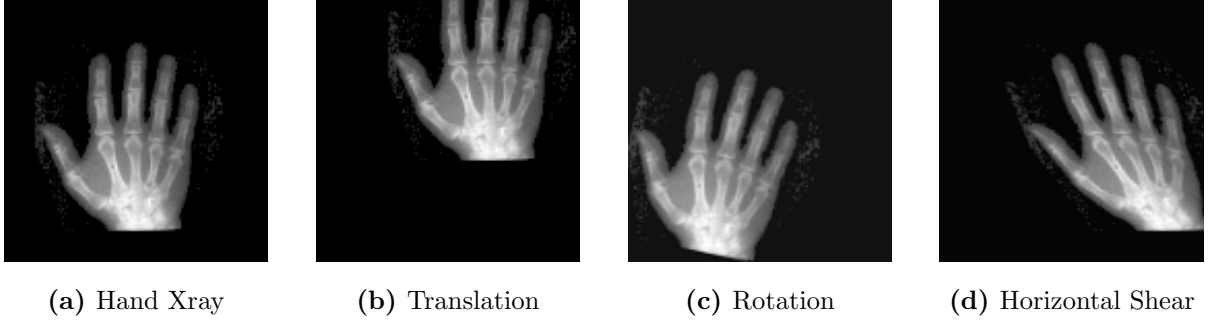
Figure 2.1: Parametric transformations applied to a hand Xray. (a) Original image, (b) translation, (c) rotation about the center of the image domain, (d) horizontal shear.

2.3.2   Similarity Measures

The first term in the objective function in the image registration model (2.1) measures the similarity between the transformed template $\mathcal{T}[f]$ and the reference image $\mathcal{R}$. Several similarity measures for intensity-based registration are being used in practice today. Among these are the Sum of Squared Distances, Normalized Gradient Field, Normalized Cross Correlation, and Mutual Information, to name a few [107].

1. Sum of Squared Differences

   The Sum of Squared Distances is one of the most commonly used distance measures in image registration. It is ideal for aligning images whose corresponding features have the same intensity. The SSD between the template and the reference image is defined as

$$\mathcal{D}^{\text{SSD}}\left[\mathcal{T}, \mathcal{R}\right] = \frac{1}{2} \int_{\Omega} \left(\mathcal{T}(x) - \mathcal{R}(x)\right)^2 dx. \tag{2.9}$$

2. Cross-Correlation

   The cross-correlation of two images $\mathcal{R}$ and $\mathcal{T}$ is given by

$$\langle \mathcal{R}, \mathcal{T} \rangle = \int_{\Omega} \mathcal{R}(x)\mathcal{T}(x)dx. \tag{2.10}$$

   Maximizing image similarity through cross-correlation essentially transforms the template image $\mathcal{T}$ such that the sum of the product of intensities at each x in the

image domain is maximized. Cross-correlation adapts naturally to situations where locally varying intensity occurs [12].

Correlation, however, is intensity-dependent. To circumvent this, the normalized cross-correlation (NCC) may instead be maximized. NCC is given by

$$\text{NCC}\,[\mathcal{R}, \mathcal{T}] = \frac{\langle \mathcal{R}, \mathcal{T} \rangle}{\|\mathcal{R}\| \, \|\mathcal{T}\|}. \tag{2.11}$$

3. Mutual Information

Mutual information quantifies the dependence of two variables in terms of their joint distribution and the distribution associated to the case of complete independence [95]. In terms of image similarity, mutual information is given by

$$I(\mathcal{R}, \mathcal{T}) = \sum_{r,t} p_{\mathcal{RT}}(r, t) \log \frac{p_{\mathcal{RT}}(r, t)}{p_{\mathcal{R}}(r) p_{\mathcal{T}}(t)}, \tag{2.12}$$

where

- r and t are image intensity values in the reference and template images,

- $p_{\mathcal{R}}(r)$ and $p_{\mathcal{T}}(t)$ denote the marginal probability distributions of $\mathcal{R}$ and $\mathcal{T}$, and

- $p_{\mathcal{RT}}(r, t)$ is the joint probability distribution.

This similarity measure is useful in multi-modal medical image registration, where corresponding tissues do not necessarily have the same intensity nor have a linear dependence. The goal when using mutual information is to find the transformation f that maximizes $I(\mathcal{R}, \mathcal{T}[f])$.

4. Normalized Gradient Field

For pairs of images where corresponding features do not necessarily have the same intensities, such as contrast-enhanced images, a suitable similarity measure is the normalized gradient field. With this distance measure, the assumption is that

intensity changes appear at corresponding positions. Since intensity changes are given by the image gradient $\nabla \mathcal{T}$, this is a quantity to look at [107]. However, since we are only concerned with the locations where the intensity changes occur and not the strength of the intensity changes, we look at $\nabla \mathcal{T} / |\nabla \mathcal{T}|$ instead. The NGF is defined as follows:

$$\mathcal{D}^{\text{NGF}}\left[\mathcal{T}, \mathcal{R}\right] = \text{NGF}\left[\mathcal{T}, \mathcal{R}\right] = \int_{\Omega} 1 - \left(\text{NGF}\left[\mathcal{T}(x)\right]^{T} \text{NGF}\left[\mathcal{R}(x)\right]\right)^{2} dx \qquad (2.13)$$

where $\text{NGF}\left[\mathcal{T}\right]$ denotes the normalized gradient field of $\mathcal{T}$, given by

$$\text{NGF}\left[\mathcal{T}\right] = \text{NGF}\left[\mathcal{T}, \eta\right] = \frac{\nabla \mathcal{T}}{\sqrt{|\nabla \mathcal{T}|^{2} + \eta^{2}}}, \qquad (2.14)$$

and η is an edge parameter.

2.3.3   Regularization

Registration is an ill-posed inverse problem. Oftentimes, the mathematical model for the problem allows for relative extrema, and the accuracy of the numerical results could be sensitive to the choice of starting point, noise in the data, or the optimization method, to name a few [107].

Regularization is an approach to address the ill-posedness of the registration problem. It can be done implicitly or explicitly. In the case of registration problems modelled by parametric transformations, regularization is imposed implicitly by applying restrictions on the parameters characterizing the transformations.

For non-parametric registration, regularization is often physical or model-based and seeks to introduce prior knowledge about the desired transformation. Explicit regularization is normally imposed through a penalty term that discourages unreasonable transformations [143].

Regularizers traditionally used in image registration include the elastic, fluid, diffusion, and curvature regularizers. We refer the reader to the following texts for more

information on regularization of image registration and other inverse problems: [34, 107, 143, 147, 152, 177].

2.4   Landmark-Based Registration

Registration algorithms are either feature- or intensity-based. As discussed in the previous section, intensity-based approaches involve the optimization of the similarity measure based on the image intensities [127]. On the other hand, feature-based methods rely on the matching of image features such as points, contours, and surfaces.

In the case of landmark-based medical image registration, point sets from both the reference and template images normally denote unique anatomical landmarks. This effectively converts the problem of finding the optimal transformation to either an interpolation or a data-fitting problem, with the landmarks serving as data points. Because of the sparsity of the landmark information compared to the amount of intensity information from the original content, landmark-based methods make for relatively fast optimization procedures [96].

Landmark-based registration completely ignores structural information and focuses only on matching corresponding landmarks. Unless a dense point correspondence is provided, the overlap within an image region typically declines as its distance from the landmarks increases. In addition, the accuracy of the registration results also depends on the accuracy of the delineation of image features provided by the identified point correspondences. In practice, however, these anatomical landmarks are usually defined manually. This could make the alignment of images susceptible to localization errors.

We now briefly discuss some transformations and interpolating functions that are used in landmark-based image registration.

2.4.1 Polynomial Transformations

1. **Affine Linear Transformations.** The primary goal is to find the vector of parameters $w = [w_1, w_2, \ldots, w_6]$ of the transformation

$$
\begin{aligned}
f^1 &= w_1 x^1 + w_2 x^2 + w_3 \\
f^2 &= w_4 x^1 + w_5 x^2 + w_6
\end{aligned}
\tag{2.15}
$$

   that minimizes the distance between the transformed template landmarks $\{f(t_j)\}_{j=1}^{K}$ and their corresponding target reference landmark locations $\{r_j\}_{j=1}^{K}$.

2. **Quadratic transformations** involve higher degrees of freedom than linear transformations. In particular, for a 2D landmark registration problem, this transformation is parametrized by

$$
\begin{aligned}
f^1 &= w_1^1 x^1 + w_2^1 x^2 + w_3^1 (x^1)^2 + w_4^1 (x^2)^2 + w_5^1 x^1 x^2 + w_6^1 \\
f^2 &= w_1^2 x^1 + w_2^2 x^2 + w_3^2 (x^1)^2 + w_4^2 (x^2)^2 + w_5^2 x^1 x^2 + w_6^2
\end{aligned}
\tag{2.16}
$$

   See Figure 2.2 for examples of polynomial transformations.

2.4.2 Interpolating Radial Basis Functions

In landmark-based registration, it is possible to impose strict landmark matching by interpreting the registration merely as an interpolation problem, with the optimal transformation being the interpolant passing through each control point while satisfying other constraints.

The use of radial basis functions (RBF) [46] is one way of forcing the Euclidean distance between reference and transformed template landmarks to zero out. Transformations described by RBFs are composed of a linear combination of radially symmetric functions ρ, each centered at a specific landmark. In addition, radial basis function values are dependent on the distances of points on the image domain from the landmarks or RBF centers.

(a) $\mathcal{R}$ with $\{r_j\}_{j=1}^{11}$ **(b)** Linear Transf f_{linear} **(c)** Quadratic Transf f_{quad}

(d) $\mathcal{T}$ with $\{t_j\}_{j=1}^{11}$ **(e)** $\mathcal{T}[f_{\text{linear}}]$ **(f)** $\mathcal{T}[f_{\text{quad}}]$
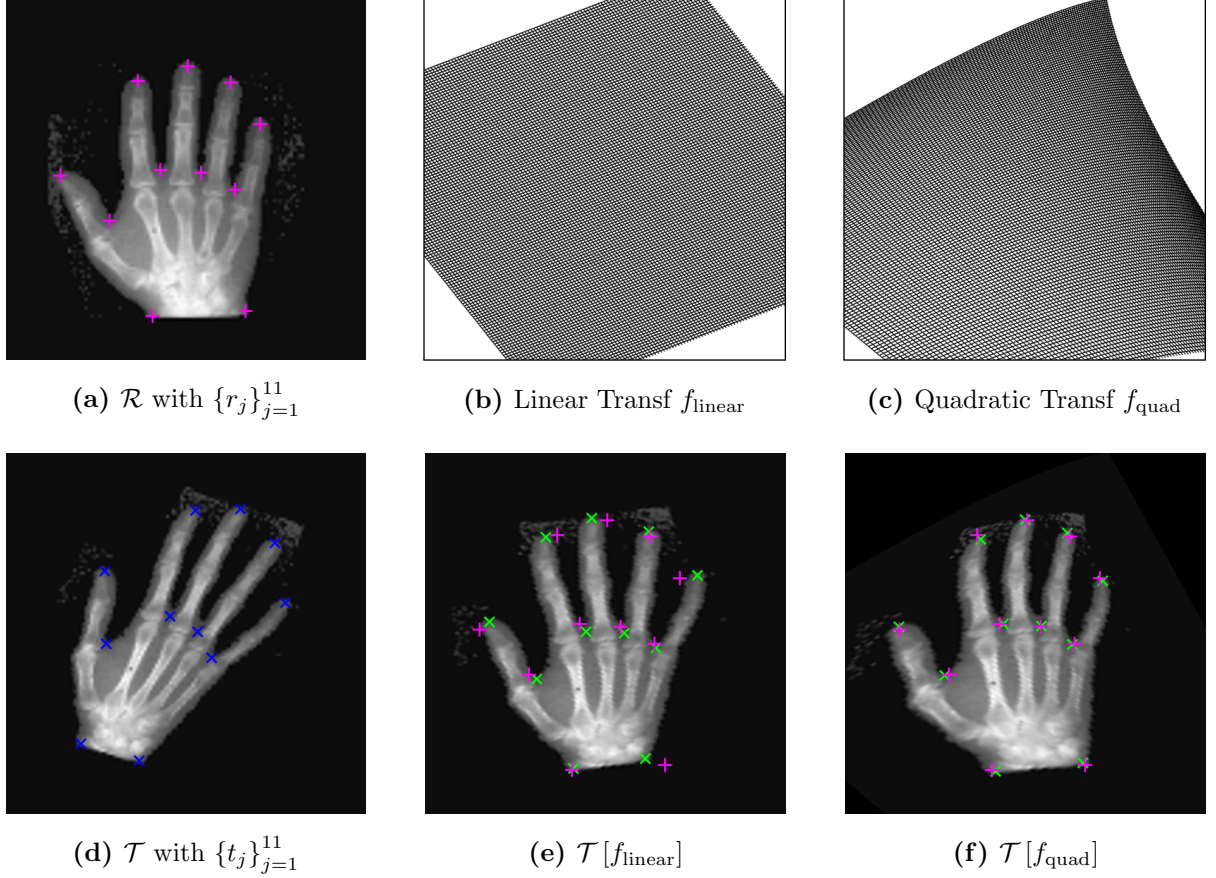
Figure 2.2: Landmark-based registration parametrized by polynomial transformations. (a) Reference image and landmarks, (b)-(c) linear and quadratic transformations minimizing the sum of landmark distances, (d) template image and landmarks, (e)-(f) transformed template images $\mathcal{T}[f_{\text{linear}}]$ and $\mathcal{T}[f_{\text{quad}}]$. Pink, blue, and green markings denote the landmarks defined on the reference, template, and transformed template, respectively.

RBFs can either be global or local, depending on the spatial range of influence by an additionally used landmark pair [46]. In this section, we enumerate some of the widely used RBFs in image registration.

1. Thin Plate Splines (Polyharmonic)

    The transformation that minimizes the bending energy of a thin plate spline corresponds to the optimal solution of the following problem:

$$\min_f \mathcal{S}^{\text{TPS}}[f] := \min_f \int_\Omega \langle \nabla^2 f(x), \nabla^2 f(x) \rangle \, dx \tag{2.17}$$

$$\text{subject to } \mathcal{D}^{\text{LM}}[f] := \sum_{j=1}^K \|f(t_j) - r_j\|^2 = 0. \tag{2.18}$$

    For a d-dimensional registration problem, the optimal solution of (2.17) has the form $f = [f^1, \ldots, f^d]^T$, where

$$f^i(x) = \sum_{j=1}^K c_j^i \rho\left(\|x - t_j\|\right) + w_0^i + w_1^i x^1 + \ldots + w_d^i x^d, \tag{2.19}$$

    and c_j^i, $w_l^i \in \mathbb{R}$ for $i \in \{1, \ldots, d\}$, and $l \in \{0, \ldots, d\}$.

    In particular, for $d = 2$ and $d = 3$,

$$\rho(r) = \begin{cases} r^2 \log r & \text{if } d = 2 \\ r & \text{if } d = 3 \end{cases}. \tag{2.20}$$

    Given K distinct data interpolation points $\{(x_j, y_j)\}_{j=1}^K$, the method of Thin Plate Splines (TPS) leads to a closed-form solution. More specifically, the parameters of the TPS interpolant in Equation (2.19) satisfy the following system of equations:

$$A c^i + B w^i = y^i \tag{2.21}$$

$$B^T c^i = 0, \tag{2.22}$$

    where

- the (p, q) entry of the kernel matrix $A \in \mathbb{R}^{K \times K}$ is given by

$$A_{p,q} = \rho \left(\| x_p - x_q \| \right), \tag{2.23}$$

- the array $B \in \mathbb{R}^{K \times (d+1)}$ is defined as

$$B = \begin{bmatrix} 1 & x_1^1 & \cdots & x_1^d \\ 1 & x_2^1 & \cdots & x_2^d \\ \vdots & \vdots & \ddots & \vdots \\ 1 & x_K^1 & \cdots & x_K^d \end{bmatrix}, \tag{2.24}$$

- $i = 1, \ldots, d.$

The set of equations in (2.22) restrict the solution within the spline space and ensure that the elastic part of the transformation tends to zero at infinity [107, 141].

2. Multiquadric and Gaussian Radial Basis Functions

Multiquadric and Gaussian functions are infinitely smooth radially symmetric functions that have a shape parameter $\sigma \geq 0$.

The multiquadric RBF is given by

$$\rho(r) = \sqrt{r^2 + \sigma^2}, \tag{2.25}$$

while the Gaussian RBF is given by

$$\rho(r) = e^{-(\sigma r)^2}. \tag{2.26}$$

For both of these RBFs, a smaller σ-value implies a "flatter" or "wider" basis function [116].

3. Wendland Functions

Introduced by Holger Wendland in [179], Wendland functions are piecewise polynomial functions that have compact support. These RBFs are uniquely defined for a given spatial dimension d and a smoothness parameter $k > 0$ [29].

The Wendland functions have the form

$$\rho_{l,k}(r) = \begin{cases} \dfrac{1}{\Gamma(k)2^{k-1}} \displaystyle\int_r^1 s(1-s)^l(s^2-r^2)^{k-1}ds & \text{if } 0 \leq r \leq 1 \\ 0 & \text{otherwise} \end{cases}. \tag{2.27}$$

In Equation (2.27), l is a function of both d and k given by

$$l(d,k) := \left\lfloor \frac{d}{2} + k \right\rfloor + 1, \tag{2.28}$$

where $\Gamma(\cdot)$ and $\lfloor \cdot \rfloor$ are notations for the Gamma and greatest integer functions, respectively. Wendland functions are defined to be nonzero only on the interval $[0,1]$. For practical applications, we note that the local influence of any compactly supported function ρ can be rescaled by instead considering the function $\rho^{[a]}$ of rescaled distances

$$\rho^{[a]}(r) = \rho\left(\frac{r}{a}\right), \tag{2.29}$$

with a denoting the desired radius of support.

Shown in Figure 2.3 are transformed versions of the template image obtained by aligning the reference and template landmarks in Figure 2.2 using the interpolating radial basis functions discussed above.

For a more detailed discussion on radial basis functions, we refer the reader to [175, 17, 46, 146, 21, 29, 26, 116, 107].

2.5 Optimization

Solving a registration problem involves the maximization of the similarity between the reference and transformed template images, be it a feature-based or an intensity-based approach. This calls for a numerical optimization scheme.

In this work, we use Gauss-Newton with Armijo line search, Gradient Descent, and Newton's method to solve constrained and unconstrained registration problems. For a

(a) $\mathcal{R}$ with $\{r_j\}_{j=1}^{11}$ **(b)** $\mathcal{T}$ with $\{t_j\}_{j=1}^{11}$ **(c)** f_{TPS} **(d)** $\mathcal{T}(f_{\mathrm{TPS}})$

(e) f_{MQ}, $\sigma = 500$ **(f)** $\mathcal{T}[f_{\mathrm{MQ}}]$, $\sigma = 500$ **(g)** f_{G}, $\sigma = 1/1500$ **(h)** $\mathcal{T}[f_{\mathrm{G}}]$, $\sigma = 1/1500$

(i) f_{W}, $a = 20$ **(j)** $\mathcal{T}[f_{\mathrm{W}}]$, $a = 20$ **(k)** f_{W}, $a = 100$ **(l)** $\mathcal{T}[f_{\mathrm{W}}]$, $a = 100$
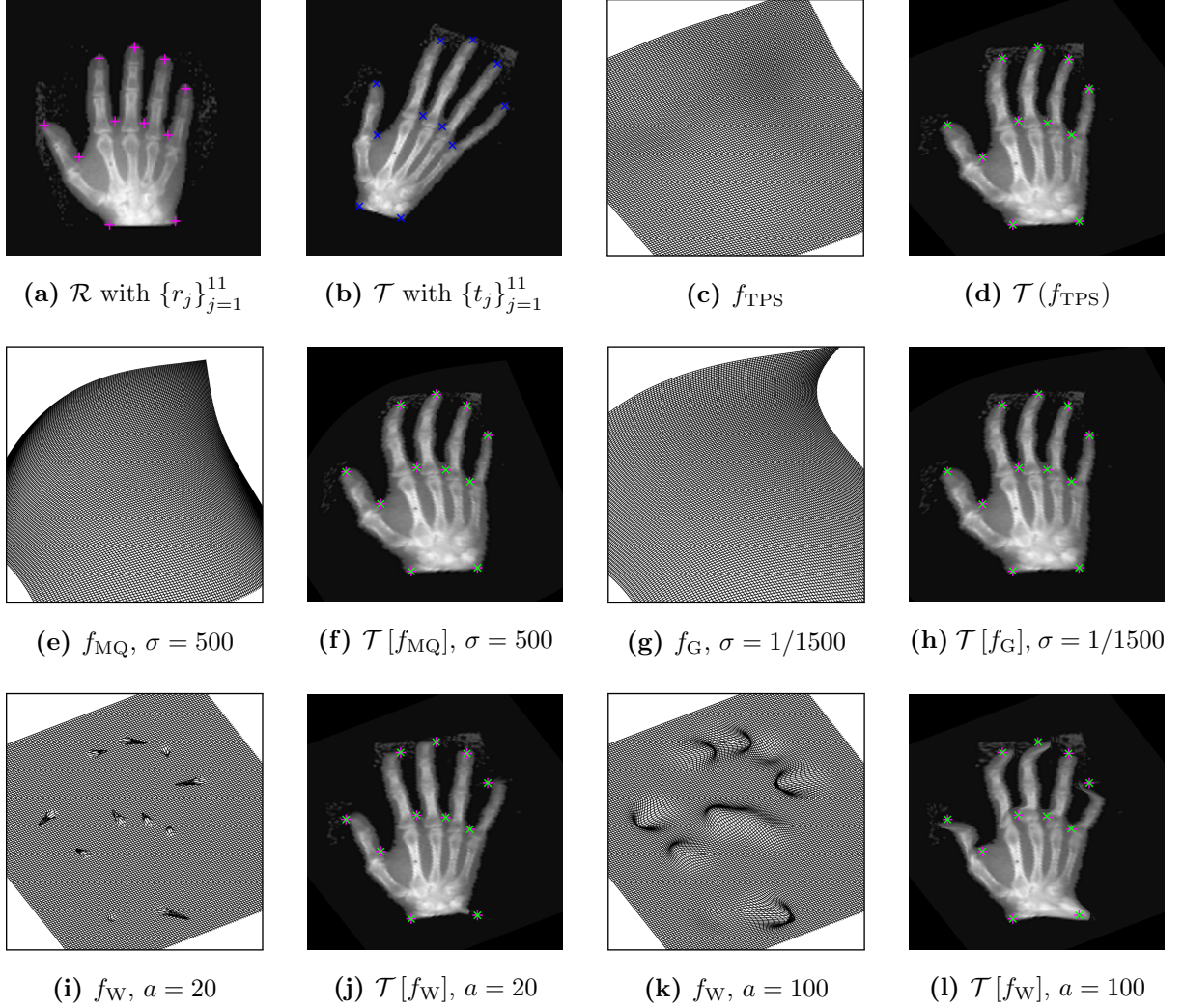
Figure 2.3: Landmark-based registration with radial basis interpolating functions. (a)-(b) Reference and template images, (c)-(d) thin plate spline transformation and transformed template, (e)-(f) multiquadric transformation and transformed template, (g)-(h) Gaussian transformation and transformed template, (i)-(l) Wendland transformations with compact support $a = 20, a = 100$ and resulting transformed templates. Pink, blue, and green markings denote the landmarks defined on the reference, template, and transformed template, respectively.

more detailed discussion on various numerical optimization methods, we refer the reader to [106, 122].

2.6 Multilevel Registration

The objective functions modelling the image registration problem are, in general, not differentiable or even continuous [41]. Mathematically, this is akin to solving an optimization problem on a non-convex set where a local minimizer does not necessarily equate to a global solution.

One approach to help eliminate the problem of running into local minima in image registration is a multilevel representation of data. A multilevel approach to image registration makes use of a coarser representation of the data to yield a smoother objective function. In addition, computations on coarser levels are relatively cheaper compared to those on finer levels.

With a multilevel approach, we start by solving the minimization problem in (2.1) on a coarser level and then progress onto finer levels. The solutions on the coarser levels serve as starting guesses for the next (finer) levels.

The intensity values of adjacent pixels are averaged in order to obtain a smoothed measurement of an image. For instance, let $L \in \mathbb{N}$ and $m = 2^L$. A multilevel representation of a vector $T \in \mathbb{R}^m$ is $\{T^l \mid l = 0, \ldots, L\}$. Here, the coarser levels are given by

$$T^{l-1} = \frac{T^l (1 : 2 : m - 1) + T^l (2 : 2 : m)}{2}.$$ (2.30)

Multilevel representation of data can also be implemented on 2D and 3D data. A detailed discussion on the computation of a multilevel representation of a 3D MR image can be found in [107].

An example of multilevel representation of 2D data is shown in Figure 2.4.
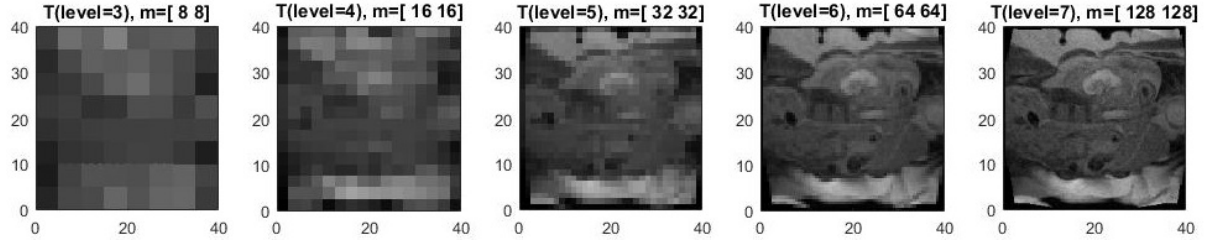
Figure 2.4: Multilevel representation of an image with 128×128 discretization points on the finest level.

2.7   Measures of Accuracy

We briefly present the measures of accuracy that are commonly used in image registration [156].

1. Dice Similarity Coefficient

   The Dice similarity coefficient (DSC), also known as the Sorensen-Dice coefficient or the overlap index, is a statistic that measures the similarity of two images $\mathcal{R}$ and $\mathcal{T}$. It is given by

   $$D(\mathcal{R}, \mathcal{T}) = \frac{2\,|\mathcal{R} \cap \mathcal{T}|}{|\mathcal{R}| + |\mathcal{T}|}. \tag{2.31}$$

   In the above equation, $|\cdot|$ denotes set cardinality.

2. Jaccard Similarity

   The Jaccard index $J(\mathcal{R}, \mathcal{T})$ is given by the ratio of the intersection of the two images to their union, i.e.,

   $$J(\mathcal{R}, \mathcal{T}) = \frac{|\mathcal{R} \cap \mathcal{T}|}{|\mathcal{R} \cup \mathcal{T}|} = \frac{|\mathcal{R} \cap \mathcal{T}|}{|\mathcal{R}| + |\mathcal{T}| - |\mathcal{R} \cap \mathcal{T}|}. \tag{2.32}$$

   Note that the Jaccard index can be calculated given the Dice similarity coeffiecient as follows:

   $$J(\mathcal{R}, \mathcal{T}) = \frac{D(\mathcal{R}, \mathcal{T})}{2 - D(\mathcal{R}, \mathcal{T})}. \tag{2.33}$$

   Also, the values of both the Jaccard and Dice coefficients range between 0 and 1.

3. Target Registration Error (TRE)

   In cases where a ground truth image is available, the target registration error may be used to assess the accuracy of the registration result. Simply put, TRE is the distance of a pixel from its correct location in the ground truth.

   Given a transformation f registering a template image to a reference image, the pre- and post-registration TREs at a point t and with respect to its target location r are given by $\|t - r\|$ and $\|f(t) - r\|$, respectively. Here, $\|\cdot\|$ denotes the Euclidean norm. A smaller post-registration TRE implies a more accurate registration.

2.8   A Preview of the Next Chapters

In this work, we prioritize registration accuracy over computational efficiency. In order to avoid the issues associated with landmark-based registration discussed in the preceding section, we opted to employ intensity-based registration methods as our starting point for medical applications involving inter- and intra-subject registration (Chapters 3 and 4, respectively).

In Chapters 5 through 7, we aim to address the computational and registration accuracy issues associated with intensity-based and landmark-based methods. We do so by first formulating in Chapter 5 a hybrid model that boosts image similarity and reduces the need for a pre-registration step. Then, in Chapter 6, we introduce a method to automatically assign exact and approximate point correspondences that works two-fold: It supplies missing edge information in between exact landmarks and simultaneously enables the implementation of a fast point-based registration pipeline. Chapter 7 serves as a logical next step to the methods instroduced in Chapter 6. Specifically, we will introduce a landmark- and contour-matching model that increases the flexibility of traditional purely landmark-based techniques, is computationally efficient, and most importantly, provides accurate registration results comparable to those of intensity-based methods.

Chapter 3

Intensity-Based Inter-Subject Registration of Magnetic Resonance Images: Application to the Construction of a Cardiac Fiber Atlas

The structural remodelling of the myocardial fibers is a main determinant of cardiac function as electrical propagation within the heart is highly anisotropic and occurs fastest in the long axis of the fibers [23, 61, 148]. For instance, discontinuities in the laminar arrangement of cardiac myocytes could trigger a nonuniform and potentially asymmetric spread of electrical activation in the ventricles and could ultimately lead to cardiac arrhythmia [65]. Thus, developing more insights on the connections between fibers and the underlying physiological structure of the heart could help in the diagnosis of cardiovascular diseases (CVD) [142].

Until recently, myocardial fiber directions have only been mapped out through histological slices [148, 66, 121, 129]. Diffusion tensor (DT) MR imaging now provides an alternative and less invasive way to characterize fiber orientations in healthy state, which can in turn be integrated into predictive image-based heart models [135, 137] and statistical atlases [164, 166].

Statistical atlases of cardiac anatomy have been built from DT images of human, canine, and rat hearts [92, 129, 131]. Of particular interest in this chapter is constructing one from pig hearts, which could provide a good alternative to human and canine hearts as the cardiac anatomies of the three species are very similar [112].

In [129], Peyrat et al. presented a detailed computational framework to build a statistical fiber atlas from 9 *ex-vivo* canine hearts. Their framework started with a groupwise registration of the anatomical MR images of the subjects, followed by a transformation of

associated DT fields. They then proceeded to compute the mean DT fields and measured the variability of eigenvalues and eigenvectors, which indicate the magnitude and preferential direction of diffusion. They also computed DT statistics characterizing cardiac fiber and laminar sheet orientations. Most importantly, they found good inter-species stability of fiber orientations between the canine and human atlases.

Lombaert et al. [92] built the first atlas of the human heart from *ex-vivo* DT-MRI acquisitions of 10 healthy hearts. Their pipeline involved the segmentation of myocardium and blood mass on each subject, construction of a morphological atlas through an iterative reference update process coupled with Symmetric Diffeomorphic Log-Demons on the unweighted images and myocardium masks, and deformation of tensor fields to the morphological atlas. They found that the fiber orientation dispersion across the population concurred with results from previous studies on mammals. Another atlas of the human heart – this time from *in-vivo* acquisitions – was built by Toussaint et al. [164], where they used sparse 2D DTI slices and the Prolate Spheroidal model of the heart to create a 3D reconstruction of the fiber architecture in the left ventricle (LV).

In [131], rat and dog myocardial atlases (also obtained through Log Demons) were used to estimate the Generalized Helicoid Model [130, 132] and to characterize the properties of the local arrangement of myofibers via three biologically meaningful curvature parameters. It was concluded that the turning of fibers within a transmural penetration from epicardium to endocardium is an important descriptor of fiber bundle variability.

Nowadays, most translational cardiovascular experiments and associated simulation-based predictive modelling are carried out using porcine models of normal and diseased hearts [154, 136, 137]. Porcine heart models mimic normal human heart anatomy, physiology and pathology very well, which motivates us to develop a high-resolution DTI-based porcine fiber atlas that could be beneficial for various preclinical studies (i.e., from disease assessment to electro-mechanical simulations).

Here, we present a pipeline employing anatomical and fiber information from DTI

to map out fiber directions in healthy pig hearts. To accomplish this, we build both a morphological and a fiber atlas through a combination of groupwise registration and DT transformation techniques that are both easy to implement and effective in retaining the diffusion information from each subject. The groupwise algorithm is coupled with a pairwise registration method that uses only intensity information to match the subjects to the reference volumes, thereby eliminating the need for landmarks and speeding up the computation of a representative cardiac volume. It also provides the displacement fields necessary to fuse information from different diffusion tensor fields and allows for analysis of diffusion properties within the population.

3.1 Diffusion Tensor Imaging

In the presence of a lesion or injury in a tissue, the axons are spaced apart and the water molecules in that tissue defy the expected direction of diffusion. Diffusion-weighted imaging is an MR technique that can quantify molecular diffusion in the body.

We can make an image sensitive to diffusion by acquiring a series of images with different duffision-encoding gradients. An example of a series of diffusion-weighted images is shown in Figure 3.1.

Le Bihan et al. suggested in [101, 87] that the signal attenuation S in DW images is influenced only by the MR acquisition parameters – namely, proton density (P), repetition and echo times (TR and TE), signal decay times after excitation (T_1 and T_2), and the diffusion-sensitive b-factors. The magnitude of the MR signal in a so-called spin-echo image is given by

$$S = P \left(1 - e^{-TR/T_1}\right) e^{-TE/T_2} e^{-bd}. \tag{3.1}$$

S is the information we obtain from MR scanners and can be interpreted as the magnitude of signal from water [118]. TR, TE, T_1, and T_2 are all measured in milliseconds
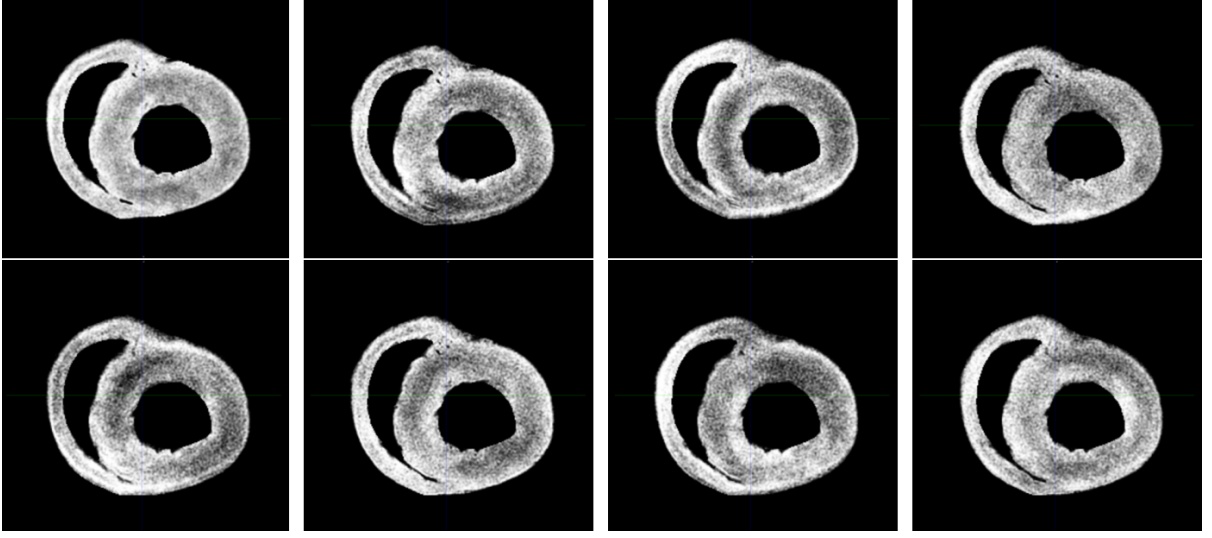
Figure 3.1: A series of diffusion-weighted images.

(ms), b is measured in s/mm^2, and d in mm^2/s.

Two separate experiments are performed to compute the diffusion coefficient d at every voxel. Keeping all the parameters fixed (with the exception of the diffusion-weighting factor) and letting $S_0 := P\left(1 - e^{-TR/T_1}\right)e^{-TE/T_2}$ yields

- $S_1 = P\left(1 - e^{-TR/T_1}\right)e^{-TE/T_2}e^{-b_1 d} = S_0 e^{-b_1 d}$ and

- $S_2 = P\left(1 - e^{-TR/T_1}\right)e^{-TE/T_2}e^{-b_2 d} = S_0 e^{-b_2 d}$.

Solving for d from the above equations leads to

$$d = -\ln\left(\frac{S_2}{S_1}\right) \bigg/ (b_2 - b_1).$$
(3.2)

The diffusion coefficient signifies the translational motion of water molecules, which is random thermal motion [68]. The information derived from DTI is dominated by static anatomy and is less influenced by physiology. It has been shown that DTI of live and fixed brains provide similar results, i.e., water molecules move, even in postmortem brains [118].

The diffusion coefficient is computed at every voxel for each sensitization or gradient direction applied to the MR image.

When water molecules are sensitized to diffusion along a single direction, the highest signal amplitude occurs along areas that are perpendicular to the direction of sensitization, and lowest in areas where diffusion is parallel to the direction of sensitization. It follows that darker voxels in a DWI would mean that water molecules passing through that voxel move parallel to the gradient direction. Lighter voxels, on the other hand, mean that there is less movement parallel to the gradient direction. In practice, at least 6 different encoding gradients are applied to cover the 3D space in order to accurately measure the amount of diffusion at every voxel [76, 77].

3.1.1 Diffusion Tensors

For a diffusion-weighted image obtained using six sensitization directions, diffusion at every voxel may be represented by a diffusion tensor. A diffusion tensor is a 3×3 symmetric positive definite matrix

$$D_{\text{tensor}} = \begin{bmatrix} d_{xx} & d_{xy} & d_{xz} \\ d_{xy} & d_{yy} & d_{yz} \\ d_{xz} & d_{yz} & d_{zz} \end{bmatrix}, \tag{3.3}$$

where d_{ij} refers to the diffusion coefficients obtained from the 6 sensitization directions, for $i, j \in \{x, y, z\}$. These tensors contain local information on the type, orientation and magnitude of diffusion. It also enables the computation of a 3D trajectory of diffusion.

The matrix D_{tensor} is characterized by its eigenvalues and eigenvectors. When the eigenvalues are ordered as $\lambda_1 \geq \lambda_2 \geq \lambda_3$, the eigenvector corresponding to the largest eigenvalue λ_1 is the principal direction of diffusion. If the eigenvalues are significantly different from each other, diffusion is said to be anisotropic [57]. On the other hand, diffusion is said to be isotropic when $\lambda_1 \approx \lambda_2 \approx \lambda_3$ [170, 76].

Each diffusion tensor can then be represented as a diffusion ellipsoid. The orientation of the ellipsoid is determined by the principal diffusion direction or eigenvector, while the girth of the ellipsoid is dictated by the homogeneity of diffusion. In the case of anisotropic

diffusion, where the eigenvalues are significantly different from each other, the associated diffusion ellipsoid is long and slender. For regions with isotropic diffusion, the associated diffusion ellipsoid is spherical and smaller.
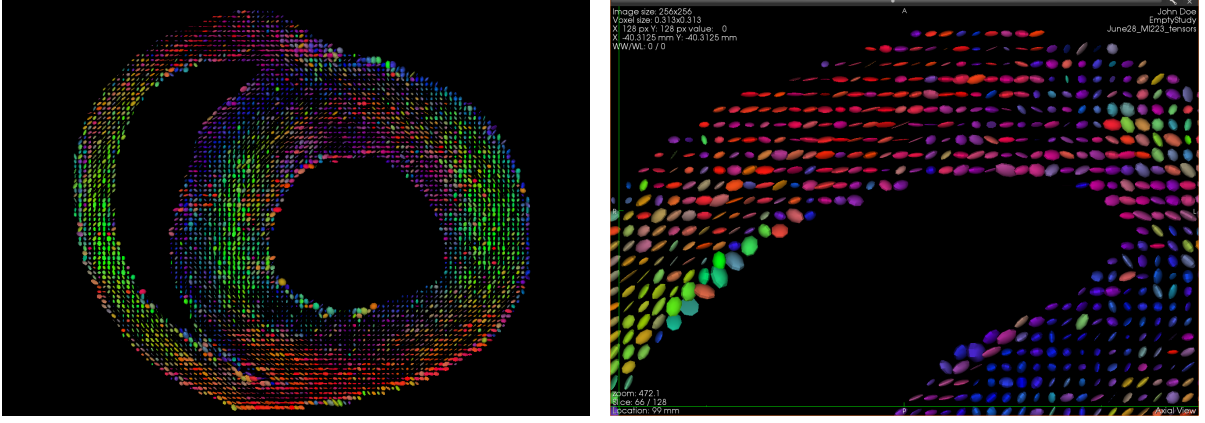
Figure 3.2: (L-R) Superior view of the diffusion tensors of a porcine heart and a close up view of the diffusion ellipsoids representing the tensors. Porcine heart images provided by Sunnybrook were processed in MedInria.

3.2   Methods

A diagram of our workflow is shown in Figure 3.3. High-resolution DT images were acquired to determine the voxel-wise preferential direction of diffusion. A mean cardiac volume was then generated through groupwise registration. The original DT fields were transformed via the rotation component of the final registration transformations and the mean of the transformed DT fields was calculated, which enabled us to map out the fiber directions. Finally, tensor and fiber statistics were computed from the atlas.

3.2.1   Heart Preparation and Diffusion-weighted MR Imaging

In this work, $N = 8$ healthy juvenile Yorkshire pigs weighing $30 - 40$ kg were used following an animal protocol that was approved by Sunnybrook Research Institute (Toronto, Canada).
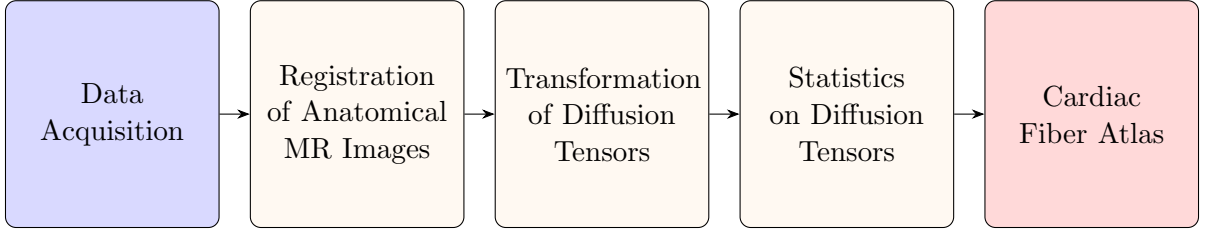
Figure 3.3: Key steps to building a cardiac fiber atlas. DT-MR images were acquired, and then a groupwise registration was performed to normalize the anatomical structures of the 8 subjects. Tensors were reoriented and averaged to determine the preferential direction of diffusion at every voxel, leading to the construction of the fiber atlas.

Following animal sacrifice, the hearts were fixed in formalin for a few days and then placed in a Plexiglas phantom box with Fluorinert (FC-770, 3M$^{\text{TM}}$, USA) to avoid susceptibility artefacts at the heart-air interface as in [134]. The diffusion-weighted (DW) MR studies were then performed by placing the phantom in a high-resolution head coil. A fast-spin echo (FSE) gradient sequence was also employed instead of an echo-planar imaging sequence (EPI). Thus, typical DWI artifacts due to eddy-currents were not observed.

In our experiments, all high-resolution DW MR images were acquired on a 1.5T GE Signa Excite scanner using the following parameters: TE = 35 ms, TR = 700-800 ms, echo train length = 2, FOV = 10-12 cm, b-value = 0 for the unweighted MR images and b = 500-600 s/mm^2 for the diffusion gradients, respectively. The total MR imaging time was approximately 8-10 hours per heart, which is not feasible for *in-vivo* patient studies.

Finally, the symmetric diffusion tensor consisting of the diffusion coefficients d measured along the x-, y-, and z-axes of the scanner for each gradient direction applied to the DW MR image was computed using MedInria [165].

The diffusion tensor characterizes voxel-wise the type, magnitude, and direction of diffusion [124, 118]. More specifically, the principal eigenvector of the diffusion tensor corresponds to myocardial fiber direction.

3.2.2   Construction of an Average Cardiac Geometry through Registration

In this section, we discuss the process of constructing an average geometry through group-wise registration. Every groupwise iteration is initialized by a set of pairwise registrations that map the unweighted ($b = 0$) anatomical MR volumes to the current reference volume. The set of deformations resulting from the pairwise registration step are then used to update the current reference volume until the groupwise registration algorithm ultimately converges to an average geometry that represents the average cardiac morphology of the dataset.

Pairwise Elastic Registration

Mathematically, the task of finding the optimal transformation f^* from a subject $\mathcal{T}_i$ to a reference $\mathcal{R}$ volume is given by the following minimization problem:

$$\min_f \mathcal{J}[f] = \min_f \ \mathcal{D}[\mathcal{T}_i[f(x)], \mathcal{R}] + \mathcal{S}[f(x)], \qquad (3.4)$$

where x refers to a physical point in the image domain Ω and $\mathcal{T}_i[f]$ is a transformed version of the ith subject.

In our experiments, we used the Sum of Squared Differences (SSD) as the similarity measure $\mathcal{D}$ and the elastic potential of the transformation f as the regularizer $\mathcal{S}$.

A more detailed discussion of elastic registration can be found in [107] and also in our previous work [112].

Groupwise Registration Model

Groupwise registration was used to normalize the cardiac measurements and obtain an average cardiac volume. Every iteration in the groupwise algorithm was initialized by a collection of pairwise transformations that align each heart to the current reference

geometry.

After mapping each heart to the current reference geometry $\mathcal{R}^n_{\mathrm{mean}}$, an update is computed as follows:

$$\mathcal{R}^{n+1}_{\mathrm{mean}}(x) = \frac{1}{N} \sum_{i=1}^{N} \mathcal{T}_i \left(f_i^n \circ [f^n_{\mathrm{mean}}]^{-1}(x) \right), \tag{3.5}$$

where

- N refers to the number of (unweighted) MR volumes $\mathcal{T}_i$ in the dataset,

- f_i^n is the transformation that registers the ith heart to the nth reference $\mathcal{R}^n_{\mathrm{mean}}$,

- the mean of the transformations registering the hearts to $\mathcal{R}^n_{\mathrm{mean}}$ is denoted by

$$f^n_{\mathrm{mean}} = \frac{1}{N} \sum_{i=1}^{N} f_i^n, \tag{3.6}$$

and

- $f_i^n \circ [f^n_{\mathrm{mean}}]^{-1}$ refers to the composition of f_i^n with the inverse of the mean transformation.

In our implementations, we assumed that the transformation f and displacement d obtained when aligning a template image to a reference image are related by the equation $f(x) = x + d(x)$. An inverse for the transformation f may be approximated by

$$\begin{aligned} [f(x)]^{-1} &\approx x - d(x) \\ &= x - (f(x) - x) \\ &= -f(x) + 2x. \end{aligned} \tag{3.7}$$

Thus, an approximation of the inverse for the average transformation field f^n_{mean} is

$$[f^n_{\mathrm{mean}}(x)]^{-1} \approx -f^n_{\mathrm{mean}}(x) + 2x. \tag{3.8}$$

Repeating the update process in Equation (3.5) converges to a stable mean geometry $\mathcal{R}_{\mathrm{mean}}$ [55] and a collection of transformations $\{f_i\}_{i=1}^{N}$ aligning the anatomical MR images to $\mathcal{R}_{\mathrm{mean}}$. Physically, $\mathcal{R}_{\mathrm{mean}}$ corresponds to the average cardiac morphology of the dataset.

Algorithm 1 The Groupwise Registration Framework

---

1. Initialize $n = 0$.

2. Set an arbitrary image in the data set as the initial reference image $\mathcal{R}^n_{\text{mean}}$.

3. Use multilevel non-parametric registration to register each image in the data set to $\mathcal{R}^n_{\text{mean}}$ and store the resulting transformation field f^n_i for $i = 1, \ldots, N$.

4. Compute the average transformation field f^n_{mean} at the nth step.

5. Approximate the inverse of f^n_{mean} using the formula in (3.8).

6. Transform each image in the data set by interpolating the intensity values of each subject $\mathcal{T}_i$ over the composition $f^n_i \circ [f^n_{\text{mean}}]^{-1}(x)$.

7. Compute the average of the transformed images to obtain the new current reference geometry $\mathcal{R}^{n+1}_{\text{mean}}(x)$.

8. Update $n \leftarrow n + 1$.

9. Repeat steps 3 to 8 until the method converges.

An outline of the groupwise registration framework is given in Algorithm 1.

In the next section, we will see how rotational information from the final set of registration transformations $\{f_i\}_{i=1}^{N}$ were used to transform the DT fields of each heart.

3.2.3   Tensor Reorientation and Average Diffusion Tensor Field

The registration step modifies the original frames of reference of the unweighted MR images. To enable the computation of an average DT field, the DT fields generated from the diffusion-weighted MR images also need to be reoriented.

Suppose that f_i is the transformation that registers the ith subject $\mathcal{T}_i$ to the average geometry $\mathcal{R}_{\text{mean}}$. With the Finite Strain method, the corresponding diffusion tensor D_i is transformed using the rotation component of the local deformation gradient $A = RU$ of f_i. The transformed tensor D_i' is given by

$$D_i' = R \cdot D_i \cdot R^T. \tag{3.9}$$

Diffusion tensors are positive-definite matrices. Therefore, they do not form a vector space and standard linear statistical techniques do not apply [42]. Log-Euclidean metrics have been demonstrated to circumvent the absence of vector space structure and incompatibility of the classical Euclidean framework on tensors while preserving their positive-definiteness [7, 6, 50].

The Log-Euclidean Fréchet mean $\overline{D}_{\text{log}}$ of the reoriented tensors D_i' at every voxel x is given by

$$\overline{D}_{\text{log}}(x) = \exp\left(\frac{1}{N} \sum_{i=1}^{N} \log\left(D_i'(x)\right) \right). \tag{3.10}$$

3.3   Experiments and Results

Prior to registration, the hearts were manually segmented in ITK Snap (`www.itksnap.org`, [181]) and the contours were checked by an expert (Dr. Mihaela Pop). At the beginning of every groupwise iteration, each subject was registered to the current reference

volume through multilevel elastic registration. The optimization problem in (3.4) was solved using Gauss-Newton method coupled with an Armijo line search.

Shown in Figure 3.4(a) are some results obtained after implementing the pairwise registration method discussed in the previous section. Dice similarity indices were also calculated to quantify the similarity between pairs of cardiac volumes. The computed similarity indices are shown in Figure 3.4(b).

Meanwhile, groupwise registration was implemented to generate a sequence of updates to the reference volume. In our experiments, an arbitrarily chosen heart in the dataset served as the initial reference. Figure 3.5(b) shows the error evolution of the groupwise algorithm given by the mean change in signal intensities between successive reference cardiac volumes. The algorithm was terminated when the average change in intensity values for the iteration was below 5% of the initial value, and the reference volumes converged to the average cardiac geometry $\mathcal{R}_{\mathrm{mean}}$ shown in Figure 3.5(c).

The rotation components of the final set of transformations aligning the hearts to $\mathcal{R}_{\mathrm{mean}}$ were then used to reorient the tensors and project them onto a common frame of reference. Illustrated in Figures 3.6(a) and (b) are the original and transformed tensors of one of the subjects, along with magnified sections in the septum and the LV free wall that demonstrate the rotation in tensor clusters when viewed laterally from left to right. Note that the following color-coding indicates the orientation of the tensors: Red=left-right (L-R), green=anterior-posterior (A-P), and blue=superior-inferior (S-I).

The average DT field was computed following the tensor transformations using Equation (3.10), and the associated average fiber architecture was visualized using MedInria [165]. Cross-sectional views of the average DT field and the associated fiber atlas are shown in Figures 3.6(c) and (d), respectively. We measured the median values of the fractional anisotropy (FA) and the mean diffusivity (MD) in a small region of interest (ROI) within the interventricular septum (Figure 3.7(a)), as well as the median fiber length for the entire fiber atlas – all of which were eventually used to gauge the accuracy
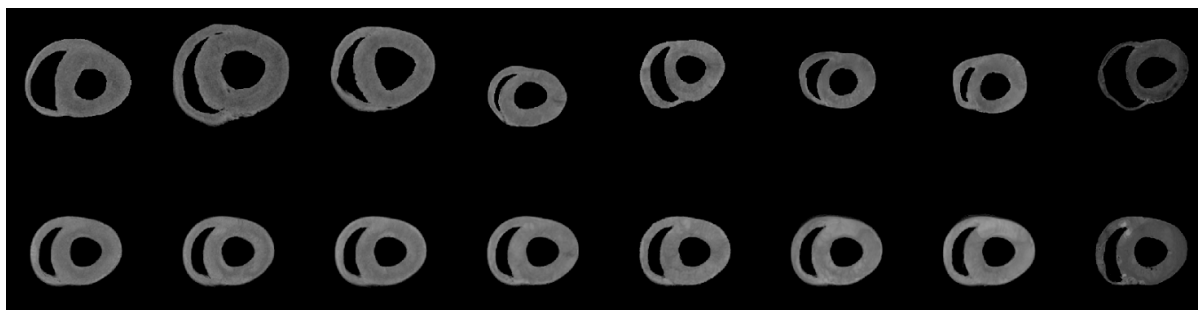
(a) Raw and registered versions of the hearts in the dataset
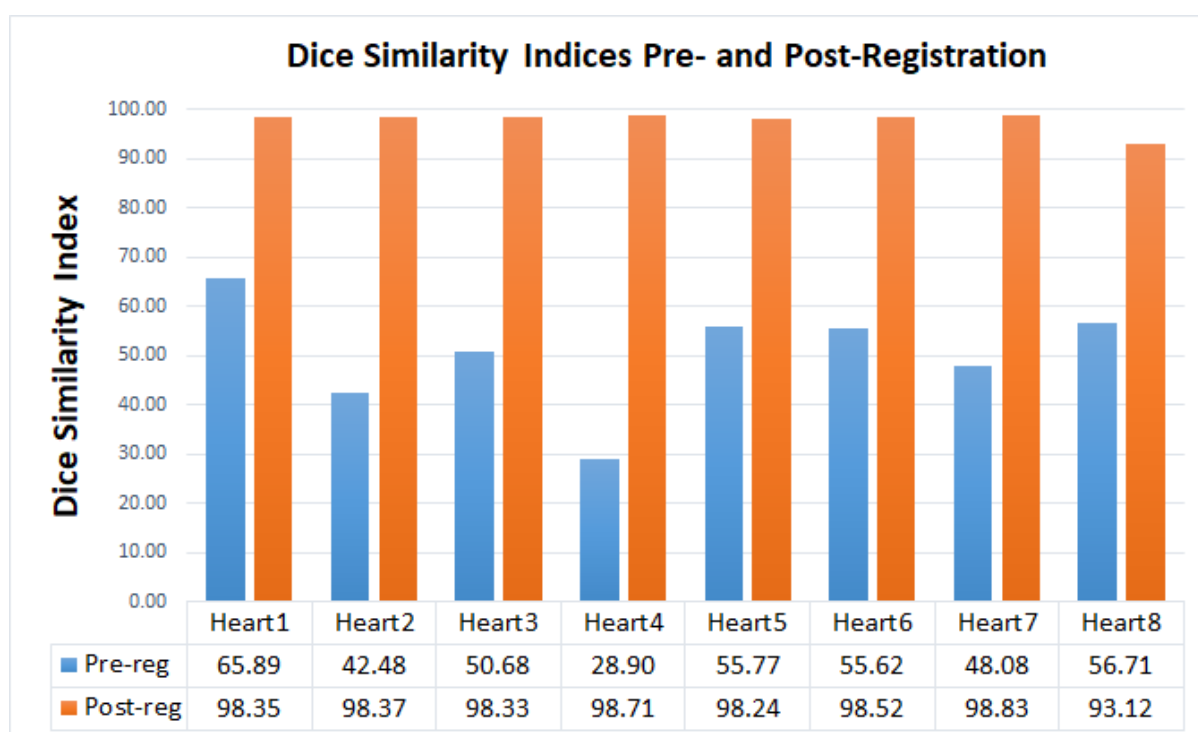
(b) Dice similarity indices

Figure 3.4: Pairwise 3D to 3D registration. (a) First Row: Center short axis slices of the unregistered hearts, Second Row: Registered/Transformed versions of the hearts, (b) Dice indices quantifying the similarity between the subjects and the final reference volume before and after registration.

(a)

(b)

(c)
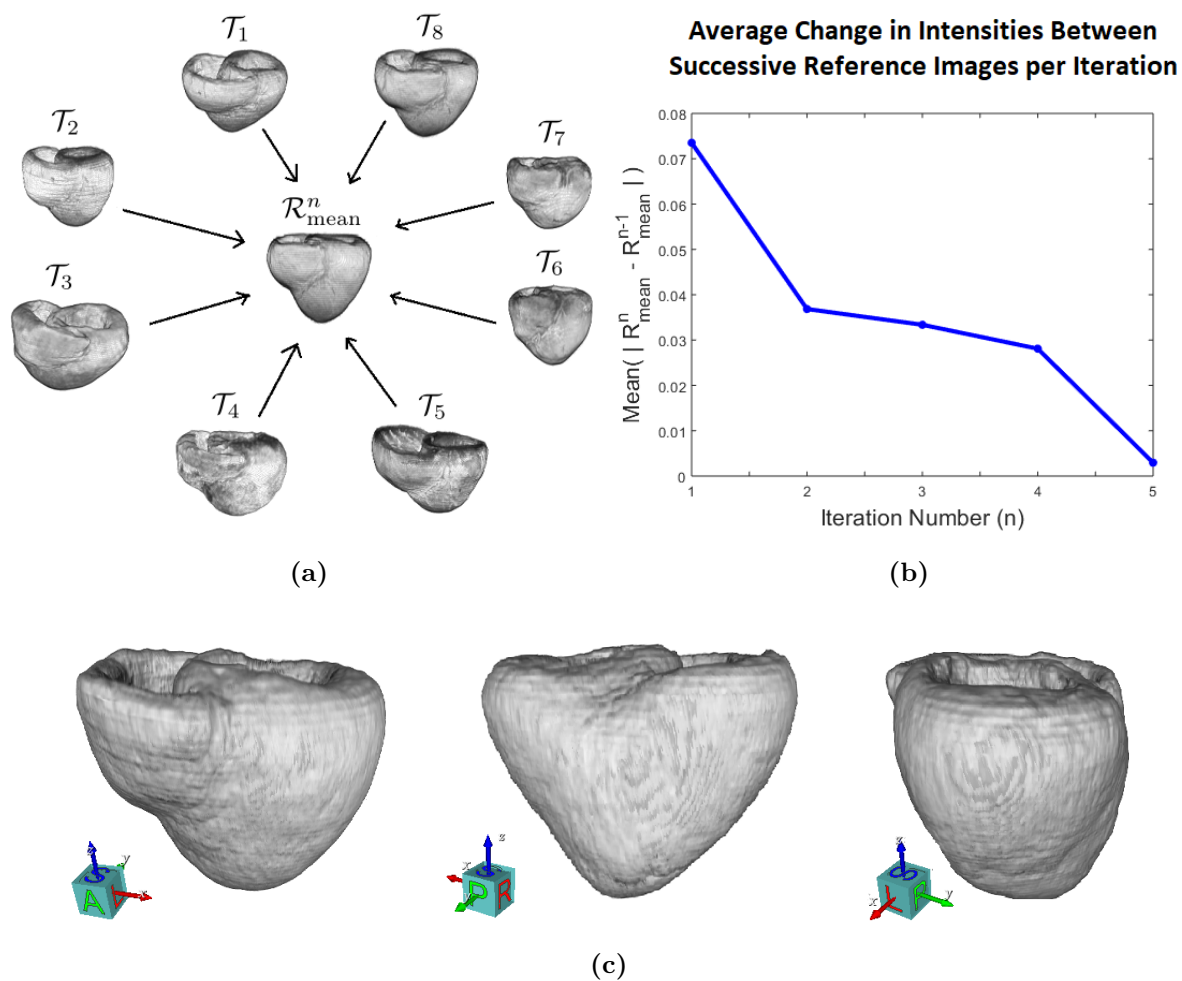
Figure 3.5: Groupwise registration and average geometry. (a) The dataset and the implementation diagram for one groupwise iteration, (b) error evolution in groupwise registration given by the average change in intensity between two consecutive reference cardiac volumes, and (c) anterior, posterior, and left lateral views of the average cardiac geometry obtained from 8 porcine hearts.

of the atlas. FA is a scalar ($0 \leq FA \leq 1$) that quantifies the degree or type of diffusion. It can be computed from the eigenvalues of a diffusion tensor D as follows:

$$FA = \sqrt{\frac{(\lambda_1 - \lambda_2)^2 + (\lambda_2 - \lambda_3)^2 + (\lambda_3 - \lambda_1)^2}{2(\lambda_1^2 + \lambda_2^2 + \lambda_3^2)}}, \tag{3.11}$$

where λ_1, λ_2, and λ_3 are the eigenvalues arranged in order of decreasing magnitude. Diffusion is isotropic if $\lambda_1 \approx \lambda_2 \approx \lambda_3$ and FA is close to zero. On the other hand, diffusion is anisotropic if there is a dominant eigenvalue (i.e., $\lambda_1 >> \lambda_2 > \lambda_3$), resulting to an FA-value that is closer to 1.

Mean diffusivity, also known as bulk mean diffusivity or apparent diffusion coefficient (ADC), is given by the average of the eigenvalues of a diffusion tensor. It is rotationally invariant, measures the overall rate of diffusion, and thus relates to the amount of water in the extracellular space [124, 173].

Finally, an exhaustive leave-one-out cross-validation [47] was performed. One round of cross-validation involved implementing the same pipeline after excluding one heart in the dataset. This was done 8 ways, excluding each heart exactly once. The median FA, MD, and fiber length from all rounds of cross-validation were averaged and compared against corresponding values from the fiber atlas constructed from 8 hearts to estimate how accurately the latter describes a healthy heart.

Presented in Figures 3.7(b)-(d) are the boxplots depicting the minimum, maximum, and median FA and MD values for the selected ROI in Figure 3.7(a) from each round of cross-validation. The median FA from the fiber atlas ($N = 8$) and the averaged leave-one-out validation results, respectively, were 0.4108 and 0.4172. The corresponding values for the median MD are $0.4907 \times 10^{-3} \text{mm}^2/\text{s}$ and $0.4611 \times 10^{-3} \text{mm}^2/\text{s}$. Meanwhile, the median fiber length from the two experiments were 85.6458mm and 86.4682mm. More details can be found in Figure 3.7. Additionally, FA statistics for the entire heart are published in [114].
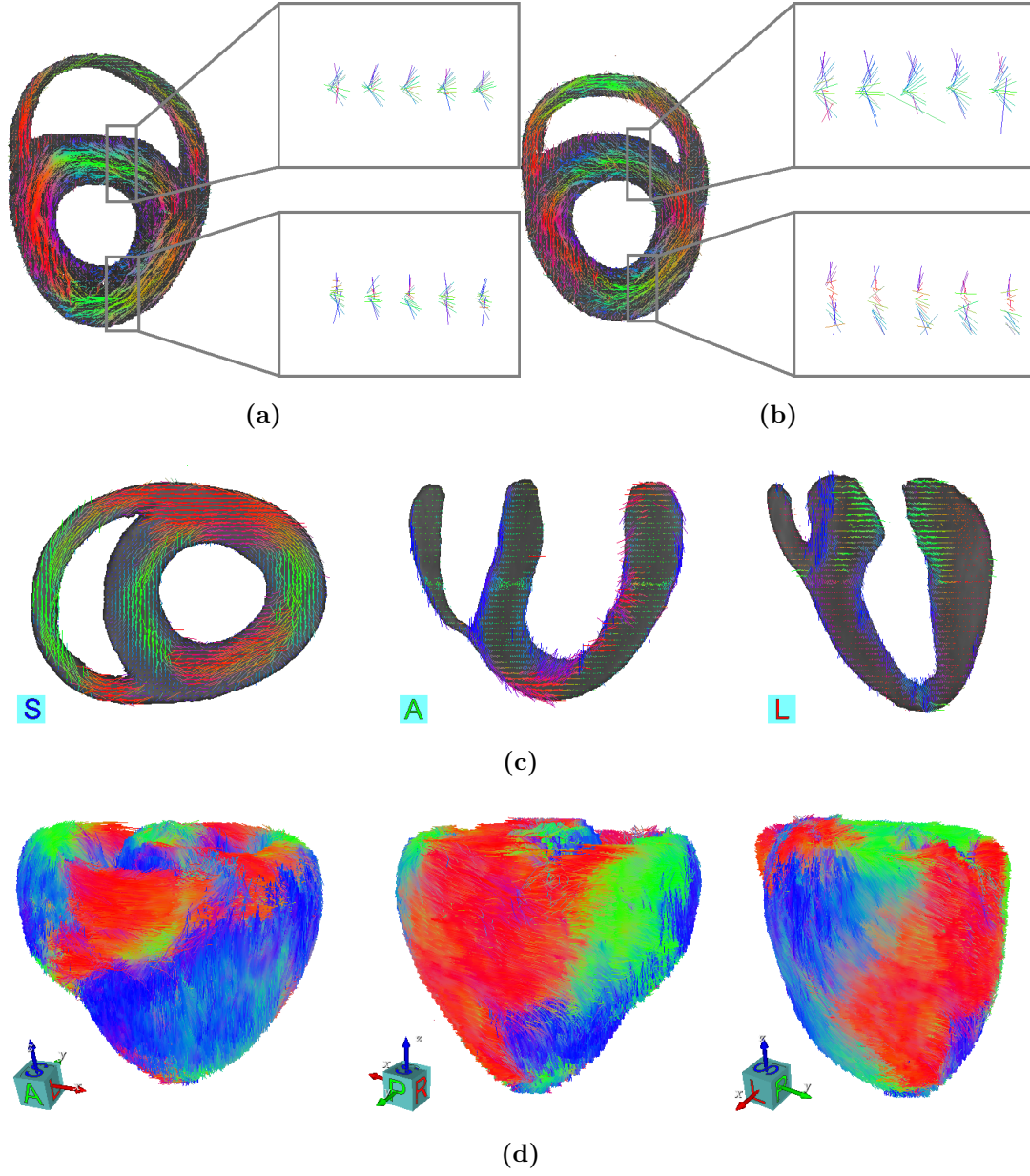
Figure 3.6: Preservation of tensor orientations, and tensor and fiber atlas. Mid-ventricular short axis slices of the (a) original and (b) transformed DT and fiber field of one of the subjects superimposed onto the corresponding unweighted MR image. Zoomed in sections show the tensors viewed transmurally from an area in the septum and the LV free wall. Observe that the geometric features and the counter-clockwise rotation of the DT fields were preserved. (c) Cross-sectional views of the average DT field superimposed onto the average cardiac morphology, and (d) anterior, posterior, and left lateral views of the associated fiber architecture obtained from 8 porcine hearts. The tensors and fibers are red, green, and blue when the primary eigenvector is oriented along the x-, y-, and z-direction, respectively.

(a)

(b)

(c)

(d)

(e)
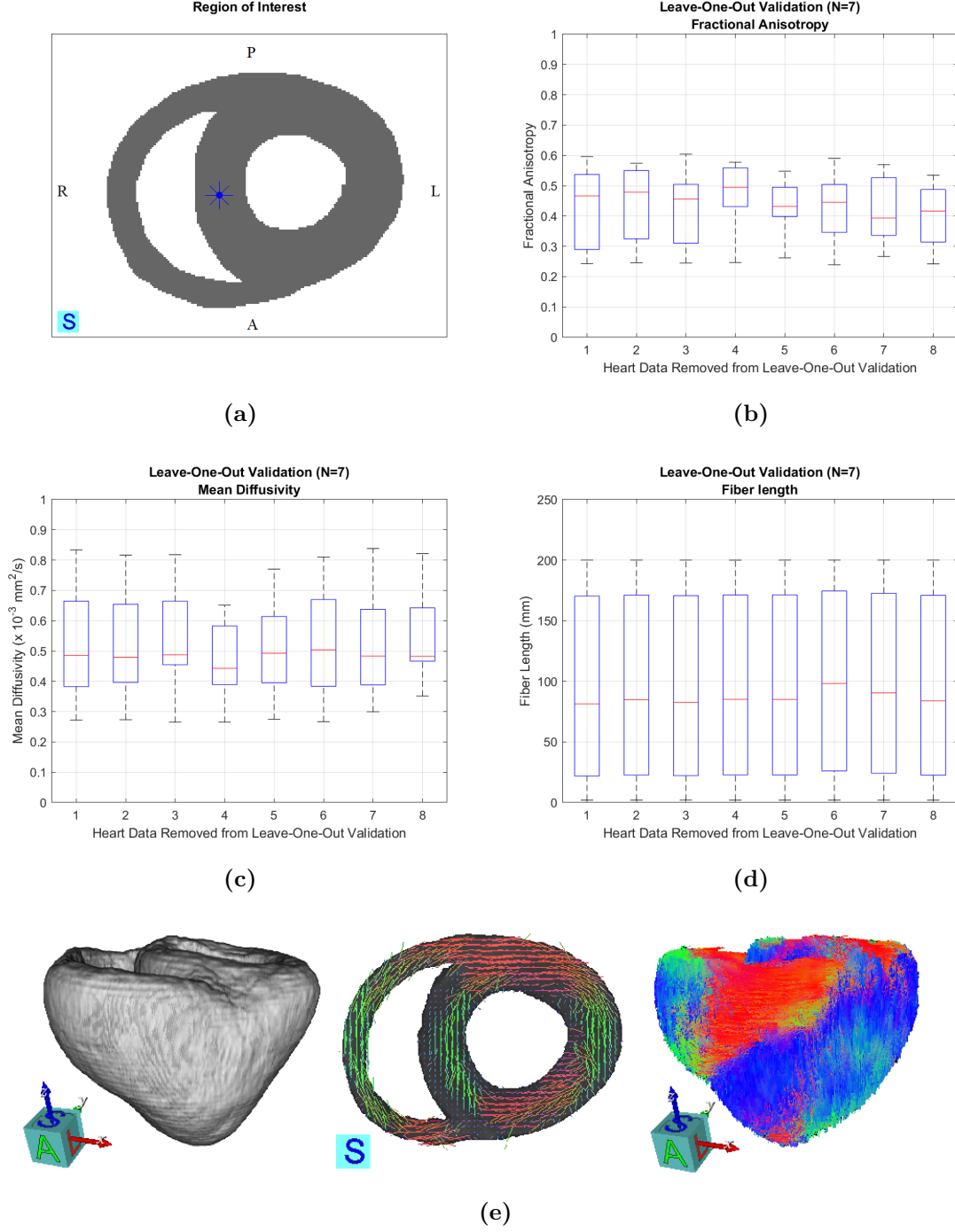
Figure 3.7: Leave-One-Out Cross-Validation. (a) Selected ROI in the interventricular septum, (b)-(d) boxplots indicating the median (in red), inter-quartile range and extreme values of the FA, MD, and fiber length from each round of cross-validation, (e) results of one round of leave-one-out cross-validation using 7 hearts: mean cardiac volume, center short axis slice of the mean DT field overlaid onto the mean cardiac volume, and the corresponding fiber atlas. The tensors and fibers are red, green, and blue when the primary eigenvector is oriented along the x-, y-, and z-direction, respectively.

3.4   Discussion

Multilevel elastic registration was able to effectively match the hearts to the reference geometries. As demonstrated by the pre- and post-registration Dice indices tabulated in Figure 3.4(b), all the hearts generally started with relatively low similarities to the reference geometries. The pairwise method we employed bumped the Dice indices up to an average of 97.81%, which corresponds to a 49.26%-241.58% increase in post-registration image similarity.

As a consequence of the effectiveness of the pairwise registration method used to initialize every groupwise iteration, the groupwise algorithm converged to a reasonable average geometry after only five iterations. The average change in intensity values between consecutive reference geometries dropped to less than 5% of the initial value – from approximately 0.0735 to 0.0029 – where the range of intensities in the anatomical MR images was $[0, 1]$.

Next, we observed the action of the Finite Strain method on the tensors. An important aspect of tensor reorientation is that it should preserve the local orientation of diffusion. As illustrated in Figures 3.6(a) and (b), the counterclockwise rotation of tensors from the LV to the endocardium on the septum and from the epicardium to the endocardium on the LV free wall was retained after reorienting the tensors using Finite Strain. This implies that the method is suited for registration of DT-MR images [129]. It follows that the computed final average DT field and its corresponding fiber architecture picked up the directional information on diffusion from all the subjects.

We remark that the averaged results from all rounds of the leave-one-out cross-validation of the fiber atlas only resulted to small errors of 1.54%, 6.02%, and 0.96% for the mean FA, MD, and fiber length. This means that the atlas that we obtained from a small database of pig hearts could accurately model the fiber architecture of a healthy pig heart.

3.5 Conclusions and Future Work

We have successfully created a cardiac fiber atlas for healthy porcine hearts. In addition, we proposed a simple pipeline for building a cardiac atlas by computing an average cardiac geometry from a small database without the need for selecting landmarks. Meanwhile, the associated average fiber architecture was built from reoriented DT fields that preserved the local fiber directions. Tensor properties extracted from the leave-one-out cross-validation of the fiber atlas indicate that constructing a cardiac fiber atlas even from a small database of pig hearts could accurately describe the fiber architecture of a healthy pig heart. To the best of our knowledge, this is the first cardiac fiber atlas constructed out of healthy porcine hearts.

Future work will focus on obtaining more tensor statistics to better understand the underlying fiber and laminar sheet structure, performing intra- and inter-species comparisons to check for correspondence of fiber and laminar sheet orientations, and using the fiber atlas for electro-mechanical simulations to predict cardiac function. Lastly, we also plan to implement the pipeline to analyze abnormal myofiber data to help research on cardiac diseases such as myocardial infarction.

Chapter 4

Intensity-Based Intra-Subject Registration of Dynamic Contrast-Enhanced Images: Application to Motion Correction in DCE Sequences

Dynamic contrast-enhanced magnetic resonance imaging (DCE-MRI) is a technique where a sequence of images are acquired before and after the administration of a paramagnetic contrast agent (CA), often gadolinium-based [91, 171, 48]. Over the last years, it has been a useful clinical technique in the characterization of tumor biology [13, 90]. The uptake of the contrast agent from this sequence of images can be quantified via a concentration versus time curve, which in turn allows us to characterize vascular permeability.

DCE-MRI continues to be a crucial component in identifying appropriate patient treatment response. However, motion present in the dataset has to first be compensated to accurately convert signal intensity changes to contrast agent concentrations [83]. Image registration has been used to successfully reduce naturally occurring motion from a sequence of DCE-MR images.

Some registration methods for DCE images involve the addition of an intensity correction term. In [36], the authors introduced a model that simultaneously aims to find the optimal transformation and the intensity correction term that compensates for intensity differences between the pair of images being registered. Meanwhile, in [2], the proposed model for pairwise registration of DCE images was based on the assumption that the moving image can be registered to the reference through a linear function. The additive and multiplicative components of the correction field were also locally penalized using a weighted Huber norm. In [83], a floating image reference scheme together with an intensity correction based on a Gaussian blurring kernel was used to register consecutive

images in a DCE sequence. In their algorithm, the starting reference was taken to be the image in the sequence that exhibits the largest average intensity. Principal component analysis (PCA) was then implemented to create a motionless dataset.

Another approach to correct motion in a DCE sequence entails the groupwise registration of the dataset to a common reference image. For instance, in [69] and [70], groupwise registration was formulated as the minimization of a PCA-based distance metric. Similarly, in [75], a hierarchical registration approach was implemented. In their paper, all post-contrast images were jointly aligned to a common reference image that was constantly updated by taking the mean of the registered images from the preceding iteration. The groupwise mean was then registered to a pre-contrast image to obtain the final registered dataset.

Some workarounds to the challenges introduced by intensity variations in contrast-enhanced images involved the use of surface markers and optical motion tracking devices to correct misalignment in image pairs, as in [79]. Others proposed the construction of a set of auxiliary images that is meant to simplify the image alignment process. For instance, in [153], the registration problem was divided into sub-problems using auxiliary images computed from the conditional probability distribution of image voxel pairs. These auxiliary images were registered to the original images using the SSD. In [72], a general tracer-kinetic model described by an input response function convolved with the plasma input function was used to obtain time-activity curves. These curves were then used to assist a succeeding groupwise registration framework based on an Expectation-Maximization framework [117].

In this Chapter, we introduce two registration methods for correcting motion in a sequence of DCE images. The first is a groupwise registration approach combined with an NGF-based pairwise step to correct motion. The groupwise framework used assumes equal weight of all pairwise transformations to come up with an update to the reference image. The second model involves the use of Tofts pharmacokinetic model [161] to

generate a sequence of synthetic images against which the template images are to be aligned. The idea is for the synthetic images to mimic the contrast of a reference image at different stages in the contrast absorption process. We validate the proposed scheme on a set of abdominal dynamic contrast-enhanced MR images. Visually, motion resulting from diaphragm motion is effectively reduced using either method. In addition, both methods yield lower post-registration target registration errors and less fluctuations in the signal intensity curves. Such attributes are indicative of the reduction of motion in the final registered dataset.

4.1 Dynamic Contrast-Enhanced Imaging

Dynamic contrast-enhanced imaging is a technique where a sequence of images are acquired before and after the administration of a paramagnetic contrast agent. DCE protocols can be readily incorporated into existing CT and MRI protocols [123].

The concentration curves resulting from the temporal enhancement pattern of a tissue enable the analysis of the tissue microvasculature, which in turn can be used in tumour diagnosis. It has been shown that the microcirculatory parameters that can be derived from the analysis of concentration curves can be used to characterize the malignancy of a tumour, aid in identifying appropriate courses of treatment, and characterize treatment response. Some of these paramaters include the transfer constant K^{trans}, the fractional volume v_{e}, the rate constant k_{ep}, and the plasma volume v_{p}.

Greater uptake of contrast agent by tumour tissue measured using MRI signal enhancement or quantitative model-based parameters such as K^{trans} has been shown to be a positive prognostic factor. Increased uptake of contrast agent before treatment may reflect a tumour that is better oxygenated and more easily infiltrated with chemotherapy agents via the vasculature, thus improving the chances of treatment success and reducing the risk of recurrence [32]. An example of pharmacokinetic modelling using DCE-MRI

data is shown in Figure 4.1.
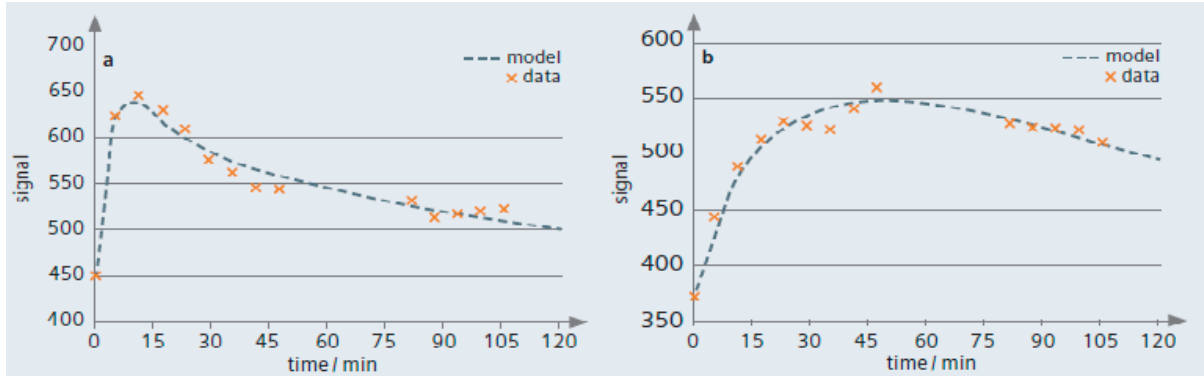
Figure 4.1: Measuring the blood-brain barrier permeability using dynamic MRI. Image taken from [161, 162].

4.1.1 Pharmacokinetic Models

Following are some models that are commonly used to describe the uptake of the Gd-DTPA contrast agent and to estimate microcirculatory parameters:

- Tofts model

  This model, proposed by Tofts and Kermode, is frequently used to characterize contrast dynamics in tissues and tumours [99]. The concentration of Gd-DTPA in the tissue is described by the biexponential function

  $$C(t) = DK^{\text{trans}} \sum_{i=1}^{2} a_i \left[\frac{\exp\left(-k_{\text{ep}}t\right) - \exp\left(-m_i t\right)}{m_i - k_{\text{ep}}} \right], \quad (4.1)$$

  where D is the injected dose of the contrast agent, K^{trans} the influx volume transfer constant, K_{ep} the efflux rate constant from the extravascular-extracellular space (EES) to plasma, the m_i's are the rate constants of CA clearance, and the a_i's are the corresponding amplitudes.

- Brix model

  The Brix pharmacokinetic model assumes that the enhancement of the signal is

proportional to the absorption of the contrast agent in the tissue. It is given by

$$C(t) = \frac{AH}{K_{ep} - K_{el}} \left[\exp\left(-K_{ep}\left(t - TA\right)\right) - \exp\left(-K_{el}\left(t - TA\right)\right) \right], \qquad (4.2)$$

where TA refers to the time of the arrival of the contrast media, K_{el} is the elimination constant of the CA from the central compartment, and AH is the amplitude scaling constant [30].

Both Tofts and Brix models are compartmental models for contrast uptake for a given region of interest with slightly different assumptions on the movement or exchange of contrast agent to and from the central compartment (plasma) and the peripheral compononent/s. In the former, equilibrium of the injected contrast agent between the plasma and EES (i.e., the whole body) and the isodirectional permeability of the plasma and EES compartments are assumed. Meanwhile, Brix model assumes that the peripheral compartment does not have any significant effects to the plasma. Detailed derivations of these two models can be found in [161, 30] and their schematics are provided in Figure 4.2.
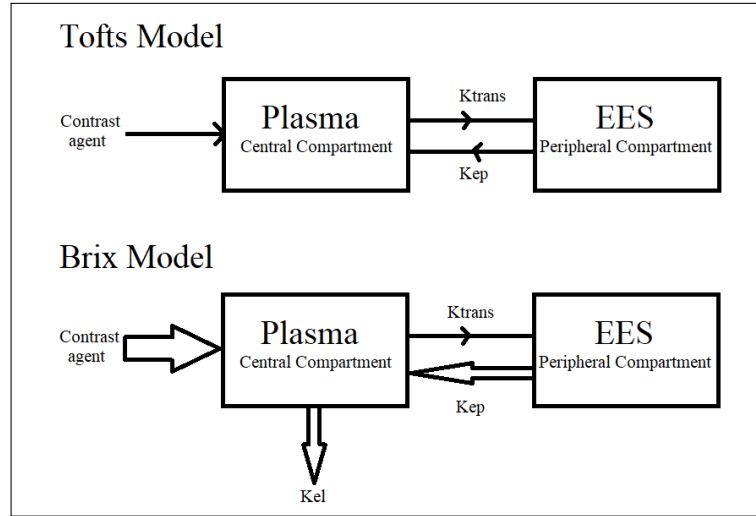
Figure 4.2: Schematics of Tofts and Brix two-compartment models. Image adapted from [30].

4.1.2 Estimating Pharmacokinetic Parameters

In this section, we discuss the Levenberg-Marquardt Algorithm for non-linear least squares minimization. This numerical method is vital in extracting pharmacokinetic parameters that are indicative of the state of the underlying vasculature.

Levenberg-Marquardt Algorithm

In practice, signal intensity curves (SI) from a sequence of DCE images are fitted to one of the pharmacokinetic models using a nonlinear fitting method like the Levenberg-Marquardt algorithm (LMA) [52]. The LMA is an iterative procedure for minimization that uses first-order information to approximate the optimal solution.

Suppose we are given a set of data points (x_i, y_i), $i = 1, \ldots, n$, and we want to find the parameter α^* of the curve $f(x, \alpha^*)$ that minimizes the sum of squared residuals

$$\mathscr{L}(\alpha) = \sum_{i=1}^{n} [y_i - f(x_i, \alpha)]^2. \tag{4.3}$$

Using the first-order Taylor expansion of f around α and letting $J_i = \partial f(x_i, \alpha)/\partial \alpha$, an approximation for the sum of squared residuals at the new estimate $\alpha + \delta$ can be computed as

$$\mathscr{L}(\alpha + \delta) = \sum_{i=1}^{n} [y_i - f(x_i, \alpha) - J_i \delta]^2. \tag{4.4}$$

Modifying the normal equation of (4.4) to include a damping factor $\lambda \geq 0$ for diagonal elements of the symmetric matrix $J^T J$ yields

$$\delta = \left[J^T J + \lambda \, \text{diag}(J^T J) \right]^{-1} \left[J^T [y - f(\alpha)] \right]. \tag{4.5}$$

4.2 Groupwise-NGF Method

An algorithm for performing unbiased groupwise registration to correct motion in a dataset of contrast-enhanced magnetic resonance images is presented. All the images

in the sequence are registered simultaneously and updates to the reference are computed using an averaging technique that takes into account all the transformations aligning each image to the current reference. The method is validated both qualitatively and quantitatively using an abdominal DCE-MRI dataset. When combined with the normalized gradient field dissimilarity measure, it produced promising results and showed significant improvements compared to those obtained through an existing motion correction approach.

4.2.1 Pairwise Registration

Constructing a motion-corrected dataset through groupwise registration entails the pairwise alignment of all the subjects to the same reference geometry.

In our implementations, we have tested the following distance measures for the pairwise registration model:

a. Normalized Gradient Field (NGF)

   The NGF is suited for aligning images where intensity changes appear at corresponding positions. These intensity changes are given by the image gradient $\nabla \mathcal{T}$. For a more detailed discussion on NGF, we refer the reader to Chapter 2 and also [107].

b. Sum of Squared Differences with Intensity Correction (SSDIC)

   In [83], intensity correction was used in combination with the SSD to partially account for intensity changes between image volumes. Instead of solving for a reasonable transformation aligning $\mathcal{T}$ and $\mathcal{R}$, we find one that matches the "intensity-corrected" template T^c to the reference, where

   $$\mathcal{T}^c = \mathcal{T} + c, \quad c = (\mathcal{R} - \mathcal{T}) * \mathrm{N}\left(0, \sigma\right), \tag{4.6}$$

   c is the pre-registration difference image filtered with Gaussian smoothing kernel $\mathrm{N}\left(0, \sigma\right)$ with a mean and standard deviation of 0 and σ, respectively. The template

image is transformed using the optimal deformation aligning the intensity-corrected template to the reference image.

4.2.2   Groupwise Registration

Groupwise registration has been used in a wide range of applications, including normalizing structural and functional MR data [53]. In [70], the performance of a groupwise registration method with a principal component analysis-based metric for correcting motion in DCE-MR images of the liver was evaluated.

Here, we adopt the method used in [62] and [129] to correct motion in a sequence of DCE-MR images. Each groupwise iteration is initialized by mapping every image in the dataset to the current reference image. The reference image is then updated using an averaging technique that takes into account all the transformations obtained from the pairwise registration step. The update to the reference is given by

$$\mathcal{R}_{\text{mean}}^{n+1}(\mathbf{x}) = \frac{1}{N} \sum_{i=1}^{N} \mathcal{T}_i \left(f_i^n \circ \left[f_{\text{mean}}^n \right]^{-1} (\mathbf{x}) \right), \tag{4.7}$$

similar to the update method discussed in Chapter 3.

4.2.3   Experiments and Results

A sequence of abdominal MR images was used for validation. The scans were acquired with a T1-weighted fast spoiled gradient-echo (FSPGR) sequence. Spatial resolution was 1.88mm by 1.88mm in the superior/inferior (S/I), left/right (L/R), and anterior/posterior (A/P) directions respectively. Temporal resolution was approximately 3.7 seconds per volume [83].

We applied the proposed groupwise algorithm to visually assess how well it eliminates real and complex patient motion. For quantitative validation, the groupwise scheme was applied to a dataset with simulated motion. The resulting sequence of registered images is then compared against the ground truth (the motionless dataset). For experiments that

made use of the SSDIC similarity measure, the standard deviation was chosen heuristically to be $\sigma = 2.7$.

Real Patient Motion

Every groupwise iteration was initialized by a pairwise alignment of the subjects to the current reference geometry. In Figure 4.4, we demonstrate how using different distance measures can affect the overall accuracy of the proposed method. Figures 4.4(f) and (i) show the optimal transformations that register Figure 4.4(b) to 4.4(a) obtained using the NGF and SSDIC. Figures 4.4(d) and (g) show the transformed versions of the template image. Observe that the NGF and SSDIC were able to align corresponding features correctly, with only slight misregistrations near the borders from using SSDIC. We also quantified the efficiency of the distance measure by computing the difference between the transformed template and the reference image. Ideally, if registration were performed properly, this difference should only exhibit the regions with contrast differences. This was the case with the NGF and the SSDIC, as demonstrated in Figures 4.4(e) and (h).

Next, we present results obtained from separate experiments using two significantly different initial reference images (one before and one after the contrast agent had been absorbed) in order to demonstrate that the proposed method for correcting motion in DCE-MR datasets is indeed unbiased regardless of the chosen initial reference. Figures 4.5(a) and (d) show the two initial reference images used. Next to the reference images are the final mean images computed using the NGF and SSDIC, respectively. Notice that the groupwise scheme converged to the same final average image when the same distance measure was used. For instance, the final mean images Figure 4.5(b) and 4.5(e) are the same despite "evolving" from different initial references.

In Figure 4.6, we show the rate of convergence of the groupwise scheme by plotting the average change in pixel values between successive iterates for the reference image against the iteration number. After around seven iterations, the average change in intensity

values dropped from approximately 0.080 to 0.005, where the intensity values of the images in the dataset lie in the interval [0,1].

Simulated Motion

Simulated motion was added to a motionless dataset similar to [83]. Non-rigid diaphragm motion during respiration combined with rigid rotations at point x during time t was modelled by

$$\Delta SI(x,t) = \Delta SI_{\mathrm{max}} \sin\left(\frac{\pi x}{x_{\mathrm{max}}}\right) \left|\sin\left(\frac{\pi t}{t_b}\right)\right|. \tag{4.8}$$

In the above equation, ΔSI_{max} is the maximum SI displacement, x_{max} is the maximum LR extent of the patient, and t_b is the duration of a full breath.

Signal Intensity Curves as Measures of Accuracy.

We present statistics on the signal intensity (SI) versus time curves over small regions of interest (ROIs). The ROIs considered are regions with relatively large motion shifts that are also affected by the administration of the contrast agent. They are shown in Figure 4.7. SI curves give us an idea of how well the registration corrects motion in the dataset. Without motion, these curves would be smooth. However, naturally occurring motion present in our dataset introduced changes unrelated to the uptake of the contrast agent.

In Figure 4.8, we display the SI curves after performing pairwise (PW) registration and groupwise (GW) registration with the NGF and SSDIC distance measures. All 4 methods were able to mitigate the effects of diaphragm motion and contrast change as demonstrated by smaller peaks in their SI curves compared to that from the simulated data. However, it is important to note the persistence of high fluctuations after using the SSDIC with either a pairwise or groupwise approach. This signifies misregistration in the specified region of interest. On the other hand, we obtained relatively smoother curves for the same ROIs after combining groupwise registration with NGF. See Figures 4.8(b),(d).

We measured the mean-squared error (MSE) of each curve to quantify how close our final registered images are to the ground truth. Out of all the methods we implemented, GW-NGF had the smallest MSE. In some cases, it even resulted to a ten-fold improvement in the MSE compared with the other methods.

To quantify the amount of motion in the registered sequence, we calculated the smoothness v_s of their accompanying SI curves. Given a time-series vector $v \in \mathbb{R}^n$ of SI values, its smoothness is given by the standard deviation (SD) of its difference vector $\text{diff}(v)$, i.e.,

$$v_s = \sigma(\text{diff}(v)), \tag{4.9}$$

where $\text{diff}(v) = [v(2) - v(1), v(3) - v(2), \ldots, v(n) - v(n-1)]^T$, and $\sigma(\cdot)$ denotes the standard deviation of the difference vector for v.

Again, the GW-NGF yielded the best results, implying that there were smaller fluctuations in the SI curves and less misregistrations in the ROIs considered. On the other hand, using the SSDIC with the groupwise scheme was either a hit or miss. Notice from the convergence of the method visualized in Figure 4.6 that the final average change in pixel values fluctuated close to the initial average change in intensity values. This could suggest that the final reference image might be similar to the initial reference and that some of the motion correction made in the previous iterations were cancelled out.

Target Registration Errors as Measures of Accuracy.

Target registration errors (TRE) are defined as the distances of pixels from their correct location in the motionless dataset pre- and post-registration. Let

- ϕ_i be the transformation that warps the ground truth (actual reference) image to the ith motion-simulated image I_i,

- f_{PW_i} the transformation that aligns the ith simulated image to the initial reference,

- f_{GW_i} the transformation that aligns the ith simulated image to the final reference, and

- ψ the transformation aligning the final groupwise mean to the ground truth.

Then the pairwise TREs before and after registration, respectively, are given by

$$|x - \phi_i(x)| \text{ and } |x - f_{\mathrm{PW}_i}(\phi_i(x))|. \tag{4.10}$$

On the other hand, the groupwise TREs are given by

$$|x - \phi(\psi_i(x))| \text{ and } |x - f_{\mathrm{GW}_i}(\phi(\psi_i((x))))|. \tag{4.11}$$

We provide the schematics for the derivation of the TREs corresponding to the pairwise and groupwise registration methods in Figure 4.3.

<div style="border:1px solid">

Pre-Reg. Frame   Registered Frame

Pairwise:

$$\mathcal{R}(x) \xrightarrow{\phi_i} \quad \mathcal{T}_i = \mathcal{R}\left[\phi_i(x)\right] \xrightarrow{f_{\mathrm{PW}i}} T_i^{\mathrm{Reg}} = \mathcal{R}\left[f_{\mathrm{PW}i}(\phi_i(x))\right] \overset{?}{\approx} \mathcal{R}(x)$$

Groupwise:

$$\mathcal{R}_{\mathrm{mean}}(x) \xrightarrow{\psi} \mathcal{R} = \mathcal{R}_{\mathrm{mean}}\left[\psi(x)\right] \xrightarrow{\phi_i} \mathcal{T}_i = \mathcal{R}_{\mathrm{mean}}\left[\phi_i(\psi(x))\right] \xrightarrow{f_{\mathrm{GW}i}} T_i^{\mathrm{Reg}} = \mathcal{R}\left[f_{\mathrm{GW}i}(\phi_i(\psi(x)))\right] \overset{?}{\approx} \mathcal{R}_{\mathrm{mean}}(x)$$

</div>

Figure 4.3: Schematics for the computation of the pairwise and groupwise target registration errors.

Shown in Figure 4.9 are the TREs for both PW-NGF and GW-NGF. Observe that the TRE post-GW registration had a smaller average compared to the usual pairwise approach. These are consistent with the results we obtained by analyzing the average signal intensity values over the same ROI in the previous section.

4.2.4   Conclusions and Next Steps

In this section, we proposed and implemented a groupwise registration approach for mitigating the effects of real and simulated diaphragm motion in a sequence of dynamic

(a) Ref. $\mathcal{R}$ **(b)** Temp. $\mathcal{T}$ **(c)** $|\mathcal{T} - \mathcal{R}|$

(d) $\mathcal{T}[f_{NGF}]$ **(e)** $|\mathcal{T}[f_{NGF}] - \mathcal{R}|$ **(f)** f_{NGF}

(g) $\mathcal{T}[f_{\text{SSDIC}}]$ **(h)** $|\mathcal{T}[f_{\text{SSDIC}}] - \mathcal{R}|$ **(i)** f_{SSDIC}
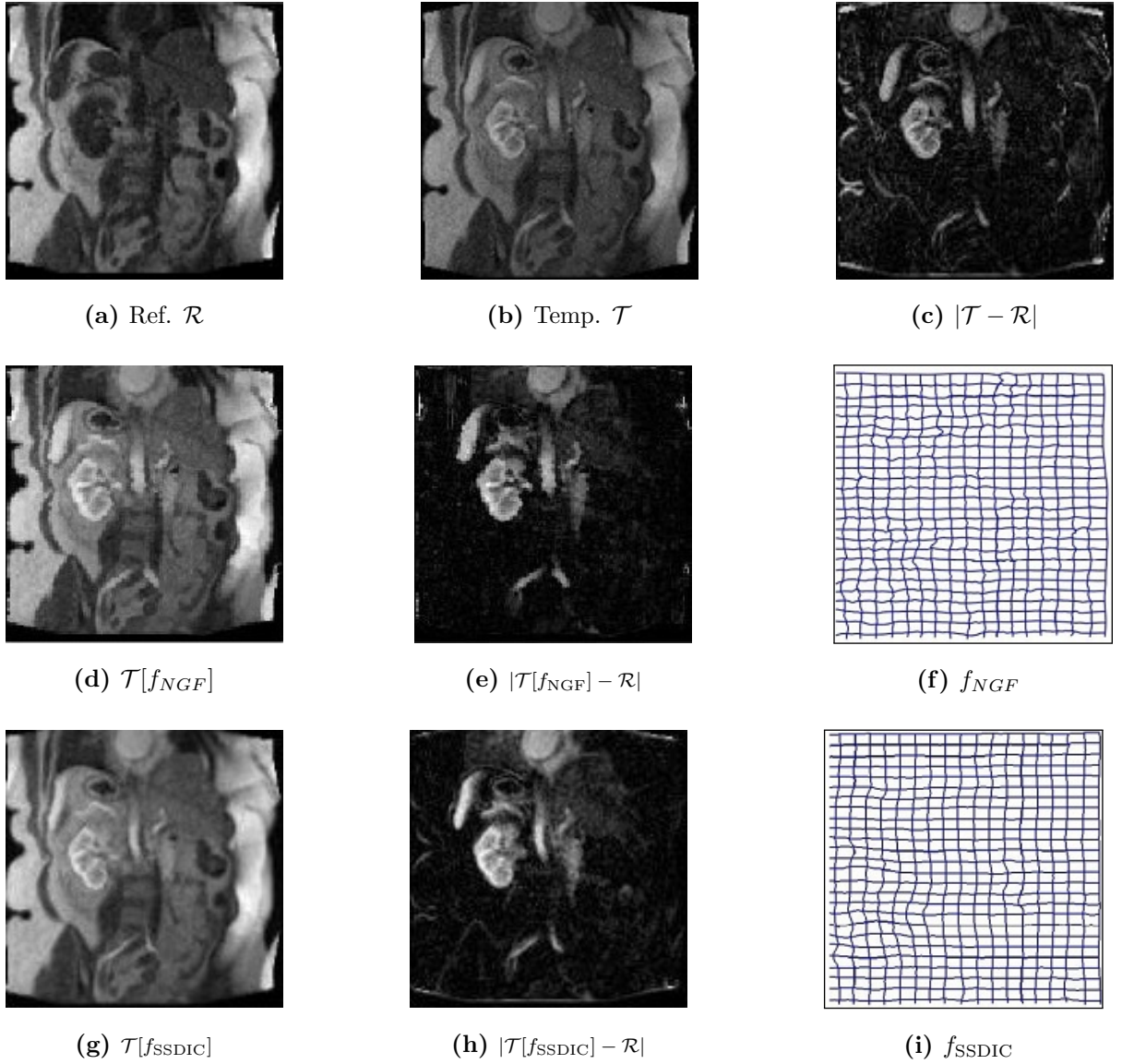
Figure 4.4: Results of pairwise registration of DCE-MR images. (a) reference, (b) template image, (c) difference image between the template and reference, (d) and (g) are the transformed templates, (e) and (h) are the difference images between the transformed template and the reference image, (f) and (i) are the optimal transformations aligning the template to the reference image using different distance measures.

(a) Initial Reference 1

(b) Final Mean - NGF

(c) Final Mean - SSDIC

(d) Initial Reference 2

(e) Final Mean - NGF
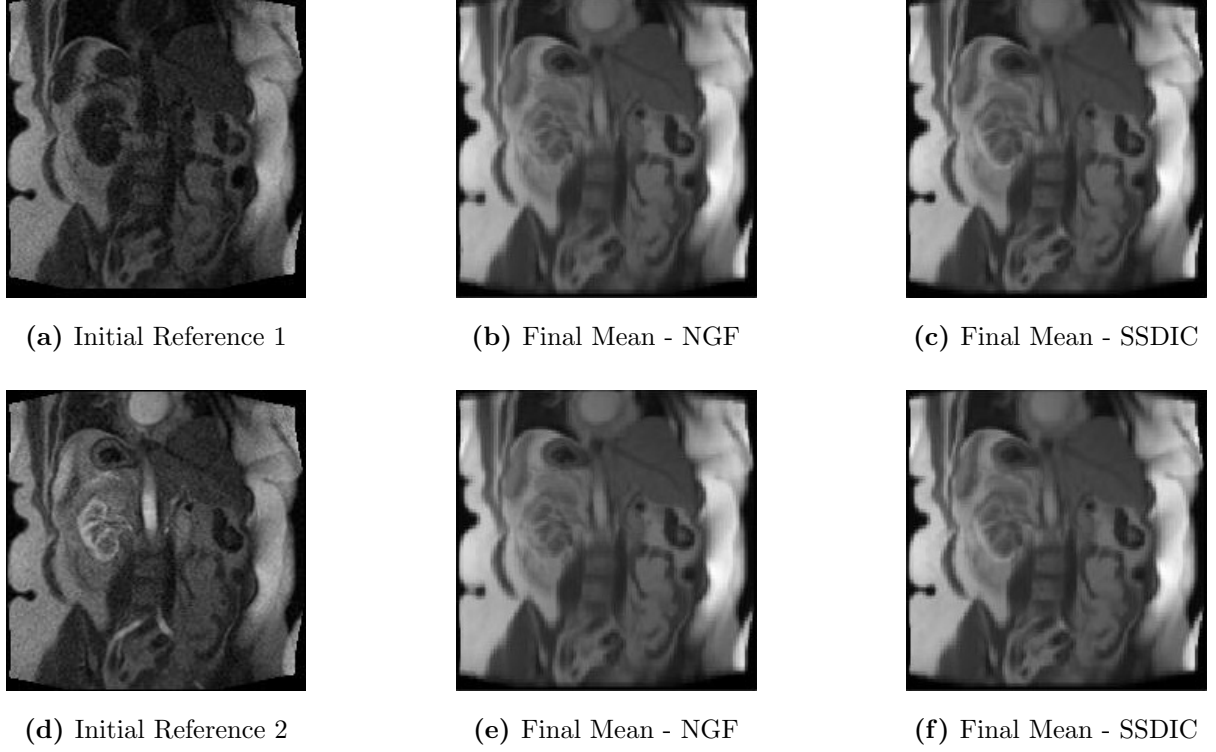
(f) Final Mean - SSDIC

Figure 4.5: Unbiased groupwise registration. The computation of the final mean image is independent of the initial reference.

	ROI 1				ROI 2			
α	PW-NGF	GW-NGF	PW-SSDIC	GW-SSDIC	PW-NGF	GW-NGF	PW-SSDIC	GW-SSDIC
100	1.68E-03	1.36E-04	2.01E-03	2.20E-03	4.91E-04	1.79E-04	1.61E-02	1.57E-02
200	1.20E-03	2.18E-04	6.40E-04	6.81E-04	5.34E-04	1.86E-04	4.81E-03	4.84E-03
600	2.12E-04	6.34E-05	7.10E-04	7.68E-04	3.30E-04	8.02E-05	1.10E-03	9.77E-04

Table 4.1: Mean Squared Error of the SI curves as a measure of the accuracy of the registration methods.

	ROI 1				ROI 2			
α	PW-NGF	GW-NGF	PW-SSDIC	GW-SSDIC	PW-NGF	GW-NGF	PW-SSDIC	GW-SSDIC
100	2.71E-02	2.48E-02	2.82E-02	2.88E-02	1.79E-02	1.43E-02	5.12E-02	5.27E-02
200	2.29E-02	2.27E-02	2.69E-02	2.95E-02	2.32E-02	2.15E-02	5.00E-02	5.03E-02
600	2.48E-02	2.43E-02	2.78E-02	2.88E-02	3.47E-02	3.46E-02	4.77E-02	4.75E-02

Table 4.2: Standard Deviation of the SI curves as means of quantifying the amount of remaining motion in the sequence of registered images.
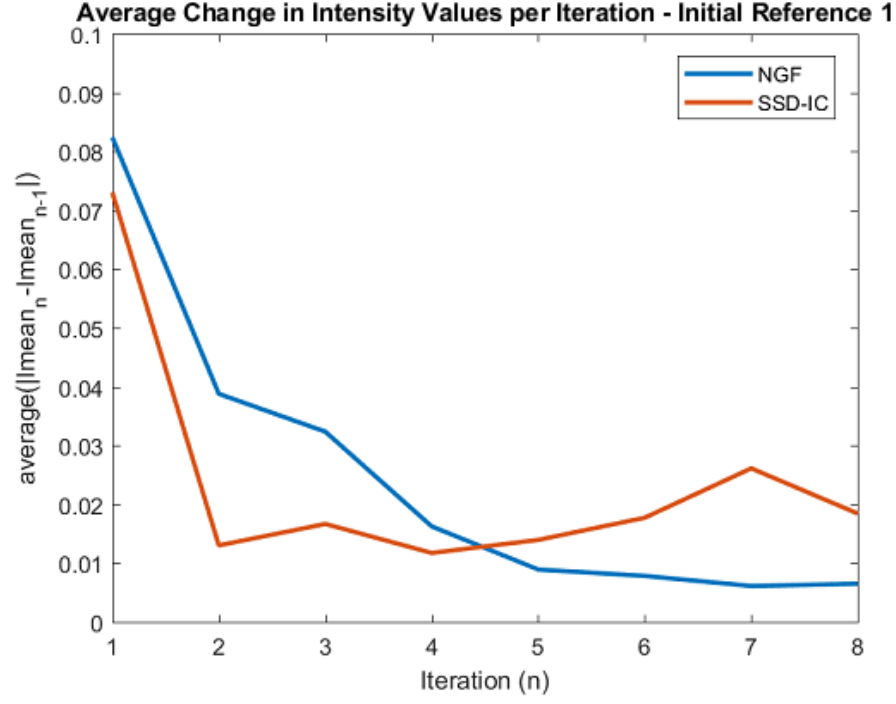
(a) Reference Image: Figure 4.5(a)
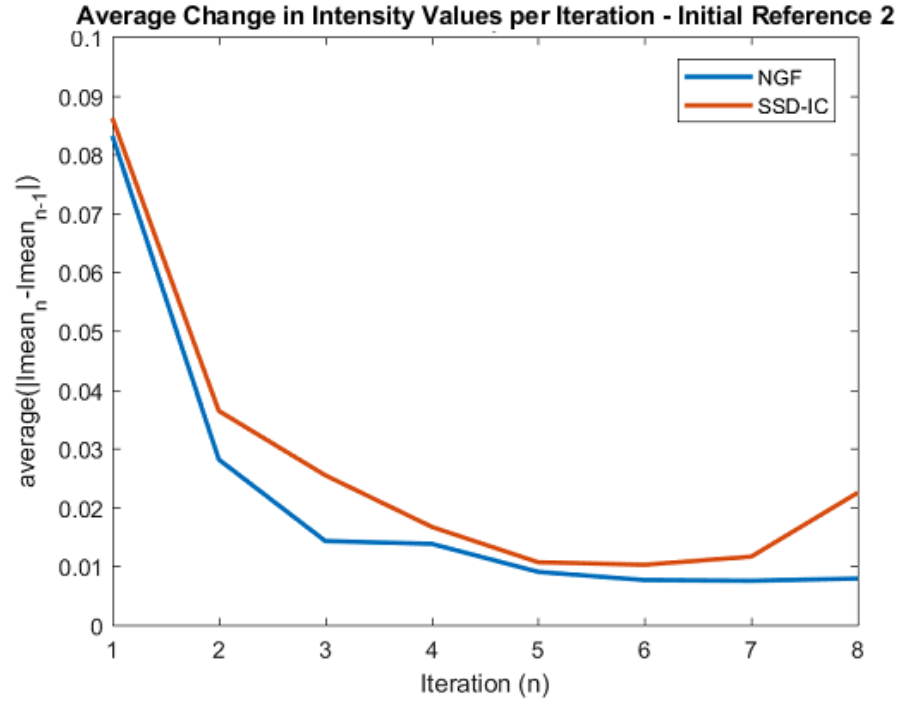
(b) Reference Image: Figure 4.5(e)

Figure 4.6: Convergence of the groupwise algorithm to a stable mean image. Range of intensity values in the DCE sequence is $[0, 1]$.
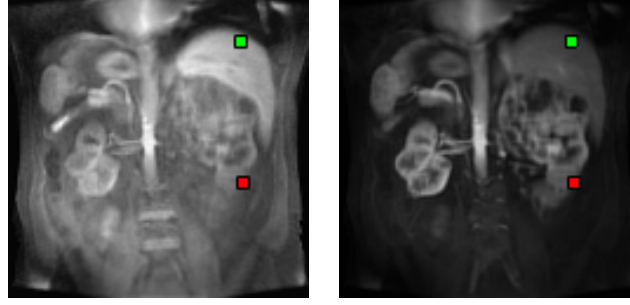
Figure 4.7: Regions of interest considered in the sequence of DCE-MR data with simulated motion. Red = ROI1; Green = ROI2

(a) PW-NGF vs GW-NGF, ROI1

(b) PW-SSDIC vs GW-SSDIC, ROI1

(c) PW-NGF vs GW-NGF,ROI2

(d) PW-SSDIC vs GW-SSDIC,ROI2
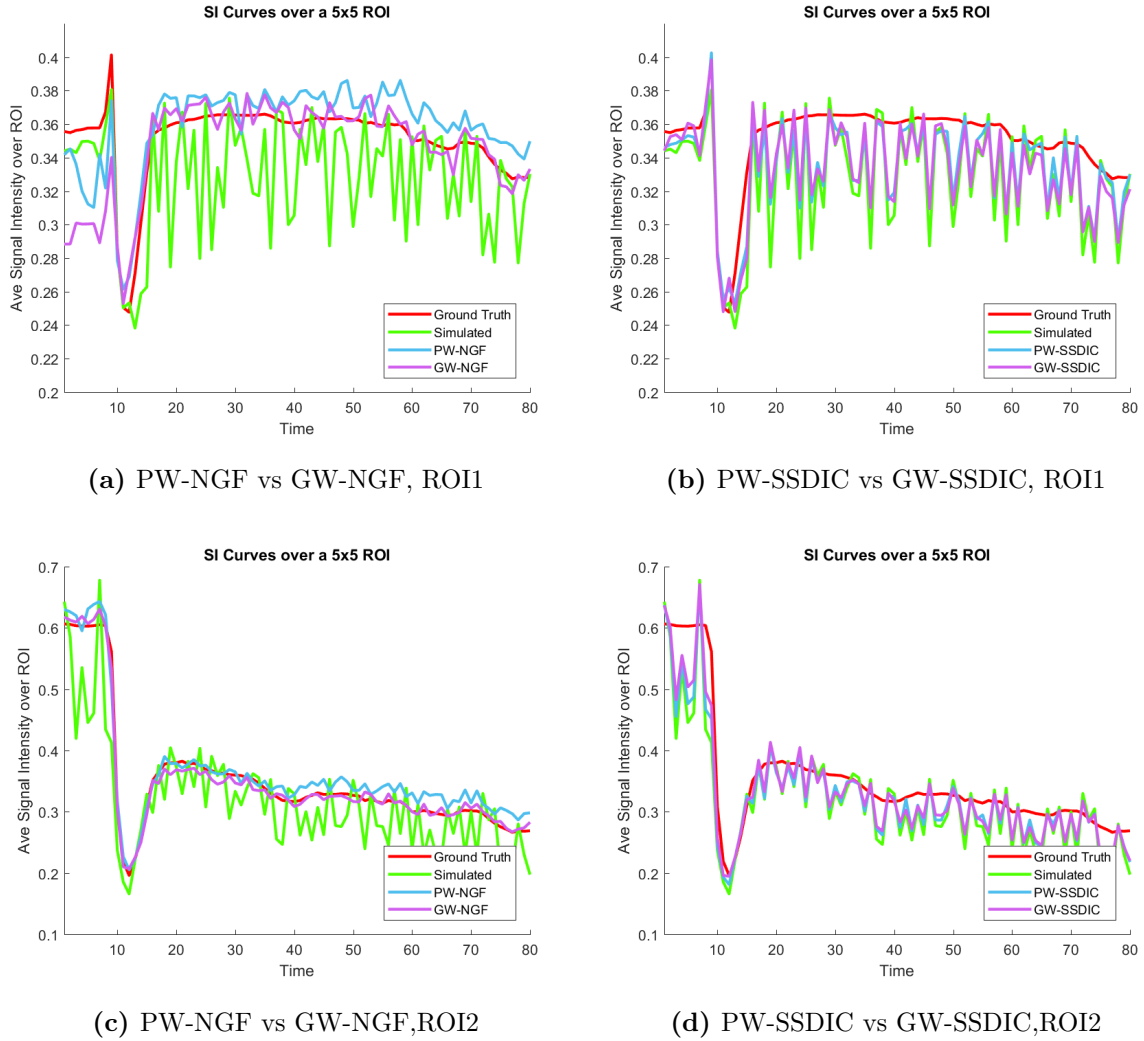
Figure 4.8: Signal intensity curves over a 5×5 region of interest. The signal intensity vs. time curves pre- and post-pairwise and groupwise registration for different ROIs.

(a) TREs - Pairwise   **(b)** TREs - Groupwise
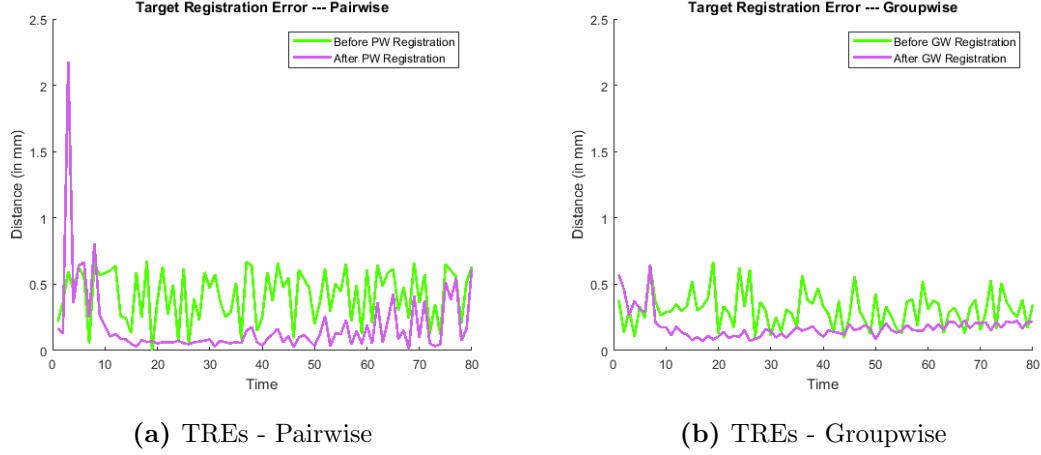
Figure 4.9: Target registration errors before and after registration. The location x of the center of ROI1 was tracked in the sequence of both the motion-corrupted (pre-registration) and motion-corrected images. The TREs are the distances of these centers from their correct location in the motionless dataset.

contrast-enhanced images. The duration of each pairwise and groupwise experiment based on the SSDIC and NGF distance measures are listed in Table B.2 in Appendix B.

We measured the performance of a multilevel elastic registration algorithm for registering contrast-enhanced images when paired with different registration models and found that both the NGF and SSDIC are able to account for contrast changes between the template and reference images.

Target registration error resulting from groupwise-registered DCE sequences was also defined and used as a measure of accuracy to better assess the performance of the groupwise registration method and to allow comparisons with the performance of pairwise registration algorithms.

We found that the groupwise approach combined with the NGF yielded the smoothest SI curves and the smallest TREs, implying that this method eliminates motion more accurately than methods that simply register against an arbitrarily chosen image from the dataset.

Finally, we aim to explore other techniques to reduce motion in a DCE sequence. In

the next section, we will propose a pharmacokinetic approach to motion correction that begins with the construction of a motionless sequence of reference images through the use of a pharmacokinetic approach model for contrast uptake.

4.3   Pharmacokinetic Method

In many existing DCE registration methods [36, 2, 83], the alignment of two images at different stages in the CA absorption process is facilitated by adding a correction term to either the template or the reference in order to account for intensity differences. In this section, we introduce the Pharmacokinetic (PK) method, where we employ a pharmacokinetic model of the uptake of the contrast agent in constructing a sequence of synthetic reference images that would allow the use of a simple and easy to implement similarity measure.

4.3.1   Registration Model

Intensity differences caused by the uptake of the contrast agent render widely used registration distance measures that are based on voxel intensity similarity are ineffective in terms of matching structural information in DCE images. As such, several methods have been proposed to register such images.

In this section, we will propose a pharmacokinetic registration method and also compare its performance against two other significantly different DCE registration methods. The three methods differ mainly in the choice of the reference images and the distance measure employed.

A. **Floating Reference (FR) Method**

Introduced in [83], the first method involves a floating reference image scheme that uses an intensity correction term to account for intensity differences between consecutive frames.

Let $\mathcal{T}_p$ be the image in the sequence with the highest average voxel intensity, where $p \in \{1, \ldots, N\}$. The FR method starts with the registration of $\mathcal{T}_{p-1}$ and $\mathcal{T}_{p+1}$ – the two frames in the sequence that are adjacent to $\mathcal{T}_p$ – to the initial reference $\mathcal{T}_p$. This results to a pair of registered images $\mathcal{T}[f_{p-1}]$ and $\mathcal{T}[f_{p+1}]$, which would then serve as the reference images against which the next pair of template images $\mathcal{T}_{p-2}$ and $\mathcal{T}_{p+2}$ are to be registered. The process is repeated until every template has been registered.

The Sum of Squared Differences [107] between an intensity-corrected template $\mathcal{T}^c$ and the reference, (i.e., the SSDIC implemented in the previous section) is used as the distance measure for the FR method.

B. Groupwise Registration (GW)

The groupwise registration method [112, 113] is an iterative approach where a common reference for the entire DCE sequence is used at each iteration. The reference is continuously updated using the registration transformations mapping the templates to the current reference, and the update process leads to both an average geometry and a final sequence of motion-corrected (registered) images.

In the previous section and in [108], a groupwise approach coupled with the Normalized Gradient Field (NGF) distance measure was proposed to correct motion in DCE images. NGF was shown to be effective in registering of images with intensity changes provided that such changes appear at corresponding positions.

C. Proposed Pharmacokinetic (PK) Method

In the pharmacokinetic method, a motionless sequence of reference images is constructed prior to registration by fitting every intensity curve over the entire image domain to a pharmacokinetic model that describes the absorption of the contrast agent. The synthetic reference images mimic the overall contrast enhancement of the template images taken at different points in the contrast absorption process.

We will demonstrate that the SSD works effectively in registering each template $\mathcal{T}_i$ with its respective synthetic reference image $\mathcal{R}_i$. That is,

$$\mathcal{D}^{\mathrm{PK}}[f] = \int_\Omega \left(\mathcal{R}_i(x) - \mathcal{T}_i\left[f(x)\right]\right)^2 dx. \tag{4.12}$$

The process of generating the motionless sequence will be discussed in further detail in the next section.

4.3.2   Constructing the Sequence of Synthetic Reference Images

Let $\mathcal{T}_1, \mathcal{T}_2, \ldots, \mathcal{T}_N$ be a sequence of DCE (template) images. The first goal is to generate a sequence of reference images

$$\{\mathcal{R}_i\}_{i=1}^N$$

such that the overall intensity of the generated image $\mathcal{R}_i$ is a close approximation of that of the ith template image $\mathcal{T}_i$. To do this, we begin by tracking the signal intensity (SI) of every pixel x in the reference image domain Ω at every time step t_i in the DCE MRI acquisition, with $i \in \{1, \ldots, N\}$. Since we know that pharmacokinetic models describe the uptake of the contrast agent in a region of interest, then we can also use these models to describe the behavior of the SI curves when there is no motion present in the data. See visualization in Figure 4.10.

Fitting the noisy SI curve of a pixel x to a pharmacokinetic model gives a smooth Tofts curve $y = f^x(t)$ such that every discrete point (t_i, y_i) in the curve would serve as a prediction of the intensity of that pixel t_i time units after the administration of the contrast agent. Performing the curve-fitting across all pixels in the image domain gives us a collection of smooth curves that make up a motionless set of reference images $\{\mathcal{R}_i\}_{i=1}^N$. These steps are illustrated in Figures 4.11 and 4.12.

A diagram of the pharmacokinetic registration method is shown in Figure 4.13.

(a) Problem: How to generate a motionless sequence of reference images?

(b) Solution: Use a pharmacokinetic model to predict the intensity of every pixel in the image domain at any time step in the acquisition.
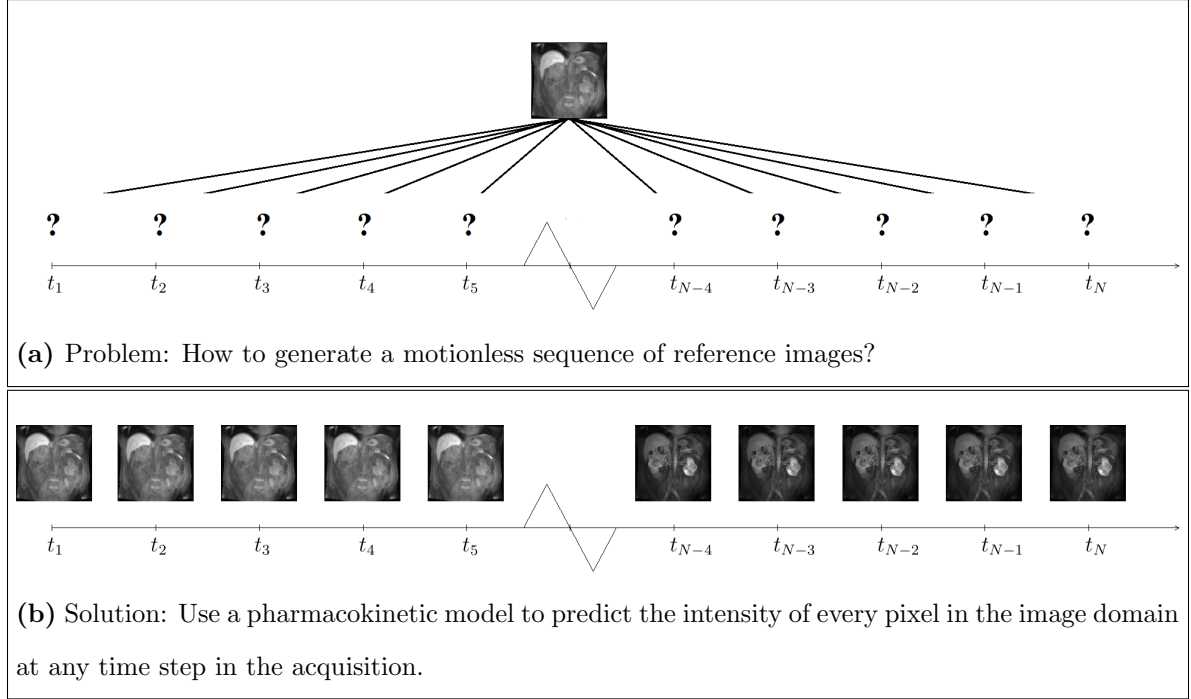
Figure 4.10: The first goal in pharmacokinetic registration method is to simplify the problem of registering pairs of images with instensity variations by constructing a sequence of synthetic reference images. Every image in this sequence would serve as the intensity-corrected version of the reference image at a specific point in the contrast absorption process, against which a corresponding template image from the original DCE sequence would be registered.
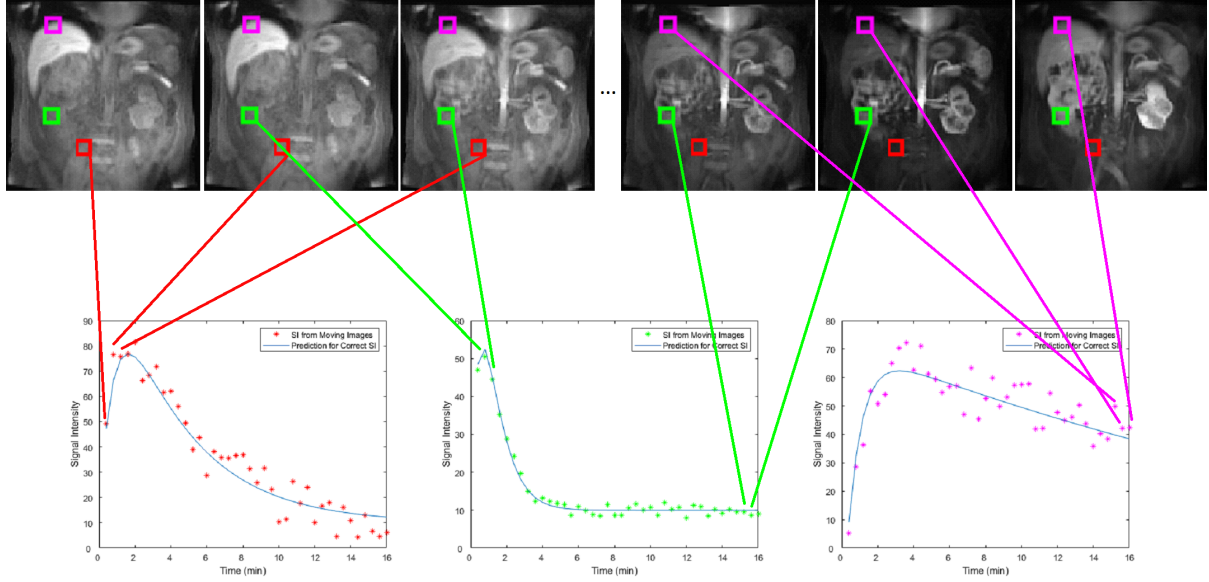
Figure 4.11: Steps 1 and 2. Fitting the pixel intensity values to a pharmacokinetic model to obtain the prediction curves (in blue). Every point (t_i, y_i) in a pixel's prediction curve represents the projected intensity of that pixel t_i time units after the injection of the contrast agent.
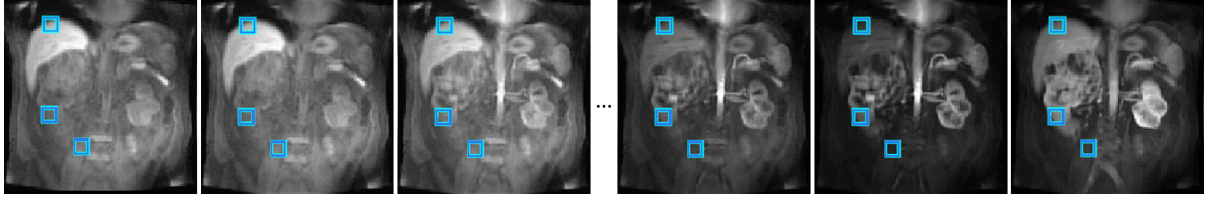
Figure 4.12: Step 3. Constructing the synthetic reference images from the fitted SI curves of all the pixels in the image domain. The intensity values at every pixel in the synthetic images are given by the values on the best-fit curves (in blue) in the previous figure. This process is repeated over all the pixels in the image domain to generate the synthetic reference image for every frame in the DCE sequence.
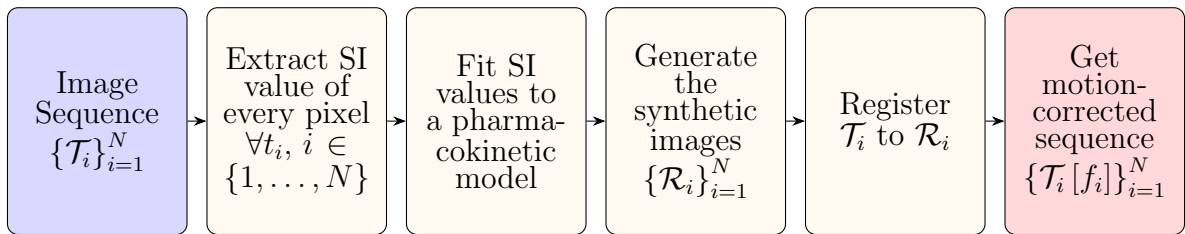
Figure 4.13: Pharmacokinetic image registration pipeline for motion correction.

4.3.3   Implementation

In this Section, we discuss the implementation details that were employed at every step in our experiments – from the weighted curve-fitting needed to generate the synthetic reference images, to the measures of accuracy used in validation.

The abdominal DCE data with simulated motion described in Section 2 was used for validation.

Intensity Curve Fitting.

To correct the motion in the sequence, a motionless sequence of reference images was first generated by fitting the intensity versus time curve of each pixel in the image domain to the Tofts model [161, 162].

It is important to recall two things that are central to our proposed method. Firstly, the main motivation behind eliminating motion in a sequence of DCE images is for accurate pharmacokinetic analysis to take place. Thus, the rate of the uptake of the contrast agent matters in the charaterization of the tissue microvasculature and the determination of the malignancy of a tumor. Secondly, curve fitting is done on the pixel level, and the signal intensity fluctuations and outlier values are actually results of the motion present in the starting data. Performing a straightforward and unweighted curve-fitting may cause the best-fit curve to fail to capture the actual rate of contrast uptake. To improve the fitting, signals at the beginning of the administration of the CA and at the peak of the absorption process were assigned larger weights. Some comparisons of the best-fit curves calculated with and without weighting for two different pixels are displayed in Figure 4.14. Observe that the curves obtained through weighted fitting more accurately characterize the CA wash-in rate. On the other hand, those obtained without weighting failed to illustrate the pre-enhancement and maximum values and also the time for the CA to peak.

The Levenberg-Marquardt algorithm (LMA) [52] was used to calculate the parameters

of the best-fit curves. In addition, the following image acquisition parameters were used for the Tofts model: $D = 0.25$ mM/kg, $a_1 = 3.99$ kg/liter, $a_2 = 4.78$ kg/liter, $m_1 = 0.144$ min^{-1}, and $m_2 = 0.011$ min^{-1}.

Registration and Benchmarks.

For the PK method, every template image $\mathcal{T}_i$ in the sequence was registered to its corresponding reference $\mathcal{R}_i$ by solving the registration problem in (2.1) with SSD similarity measure and elastic regularizater [107].

As mentioned in Section 3, visual and quantitative aspects of the final PK-registered sequence will be compared against those resulting from two other existing registration-based DCE motion-correction techniques. The FR and GW-NGF registration [108] pipelines were implemented as presented in [83] and Section 4.2, respectively, to provide baseline results.

Measures of Accuracy.

To visually assess the reduction of motion in the final registered sequences, difference images will be observed. Without motion, the difference image between consecutive registered images would be mostly black, except for the regions that were affected by the uptake of the contrast agent.

We will also gauge the accuracy of the results by computing the mean squared error (MSE) and standard deviation (SD) of signal intensity (SI) curves in regions of interest (ROIs), in addition to the average target registration error (TRE).

ROIs are small regions within the image domain that exhibit contrast enhancement and are also affected by naturally occurring motion. The ROIs that were considered in our work are shown in Figures 4.18(a)-(b).

In the absence of motion, SI curves would be smooth and depict only the average intensity change due to the contrast enhancement in an ROI over time. However, natu-

rally occurring motion present in our data causes fluctuations in the SI curves that are unrelated to contrast enhancement.

As in the previous section, we measured the smoothness v_s of a vector v of SI values by calculating the SD of its difference vector diff(v). On the other hand, calculating the MSE allows us to quantify how close an ROI average signal intensity from the final registered sequence is to its corresponding value from the motionless (ground truth) sequence.

The TRE evaluates the distance of pixel locations after registration from their correct locations in the motionless (ground truth) sequence. A detailed discussion of TREs can be found in [108].

Finally, we emphasize that the PK method and the two other methods that we will use as benchmarks (namely, FR and GW) all differ in their choice of reference images. In PK, the synthetic reference images were constructed with the use of a pharmacokinetic model. In FR, the initial reference was taken to be the brightest image in the sequence. Then, in GW, the common reference was given by the groupwise average. This means that in order to accurately measure the TRE and the MSE of the SI curves, the ground truth images needed to be translated by aligning them to the reference image for each method.

4.3.4 Results and Discussion

We now present the results of the registration methods discussed in Section 3. We begin by observing the difference images before and after registration. Difference images from consecutive frames in the initial DCE sequence with simulated motion are shown in Figure 4.15b. As expected, the images are characterized by both contrast enhancement and motion shifts due to the simulated diaphragm motion.

The FR and GW schemes were implemented to provide benchmarks for our proposed method. Some consecutive frames from the final registered sequences are displayed in Figures 4.15c and 4.15e, along with their respective difference images. A reduction of

artefacts in the benchmark difference images (Figures 4.15d and 4.15f) demonstrate better alignment and less motion between successive frames. We remark that difference images from the GW method indicate that the GW method is more effective at eliminating motion than the FR method.

To facilitate the application of the proposed pharmacokinetic method, a motionless sequence of reference images were first generated (Figure 4.15g) and every template was registered to its corresponding reference. Note that the difference images from the registered sequence were closer to null, with the exception of regions that were enhanced by the contrast agent. This means that, visually, the PK method eliminates motion more effectively than both the FR and GW methods.

Shown in the first column of Figure 4.16 are TREs pre- and post-FR, GW, and PK registration for $\alpha = 500$. Overall, PK yielded the smallest average TREs per frame. In addition, the fluctuations in the TRE curves are smaller compared to the FR and GW TRE curves. This indicates that there is less motion between successive PK-registered images.

Each boxplot in Figure 4.17 displays the full range of variations of the average TRE per frame in the final registered sequence of images for specific values of the regularization parameter α. For instance, the first box and whiskers plot in Figure 4.17(a) tell us that the median of the average TRE across all $N = 80$ registered images is 0.27 mm when the FR method is used together with an elastic regularization parameter of $\alpha = 100$. On the other hand, the GW approach yielded a median value of 0.45 mm for the same regularization parameter. The red markings correspond to outlier average TRE values in the registered sequences.

The boxplots reveal that the median, as well as the inter-quartile range and maximum value of the TREs resulting from the pharmacokinetic method are consistently lower compared to those of the groupwise registration method. This means that after pharmacokinetic registration, the transformed grid points are closer to their correct

(ground truth) location.

For the local measures of accuracy, we observed the same 2 ROIs in the previous section that manifest different uptake rates of the contrast agent. For each ROI, we compared the mean squared errors standard deviations of the SI curves resulting from the three method and across different values of the regularization parameter.

With respect to the initial template sequence, only the PK method consistently yielded lower post-registration MSEs. The FR and GW methods tend to suffer in these local measures of accuracy. See Figure 4.16(b), for instance. While the FR registration led to a smaller post-registration SDs, the intensity-correction employed by the FR method introduced some blurring both in the intensity-corrected templates and in the registered images and resulted in larger post-registration MSEs. Blurring artifacts introduced by the FR method imply that the registered sequence does not accurately reflect the intensity enhancements caused by the CA to the initial motion-corrupted sequence and, hence, it may not be ideal for applications that require an accurate analysis of the wash-in and wash-out of the contrast agent.

In the case of the GW method (Figure 4.16(d)), small SI curve fluctuations persisted in the first few frames after implementing GW registration in some of the ROIs that were considered. This also equates to higher MSEs and is characteristic of local misregistrations, which then translates to the presence of motion in the registered sequence.

Finally, we also analyzed the standard deviation in the SI curves to measure the amount of remaining motion in the registered images. Consistent with the other measures of accuracy, the SDs resulting from the pharmacokinetic method were generally lower than their counterparts from the groupwise method. This implies that the proposed method produces smoother SI curves with smaller fluctuations, which then translates to more accurate local alignment.

Summaries of the SI curve statistics across different values of the regularization parameter α and for different ROIs are displayed in Figure 4.18. Implementation runtimes

for each method are listed in Table B.2 in Appendix B.
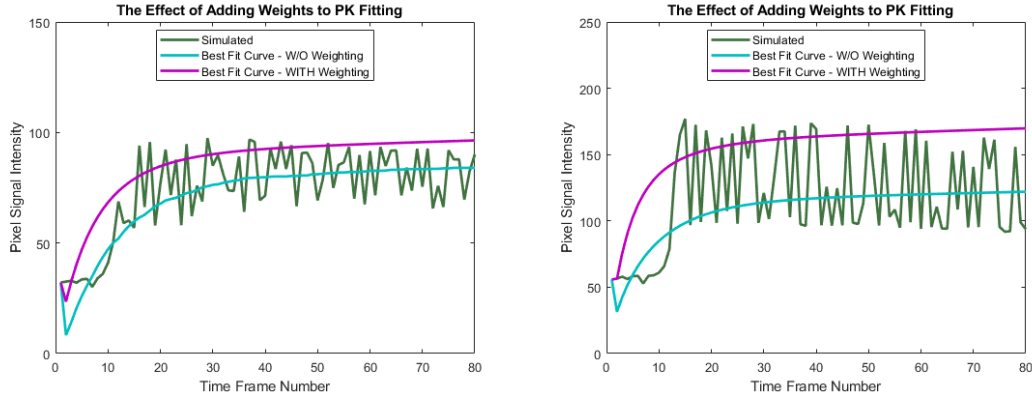
Figure 4.14: Best-fit curves computed with and without weighting for two pixels. For weighted PK fitting, larger weights were assigned to the starting and the largest values in every signal intensity curve. Observe that the curves obtained through weighted fitting more accurately characterize the CA wash-in rate. On the other hand, those obtained without weighting failed to illustrate the pre-enhancement and maximum values.

4.3.5   Conclusions and Future Work

We introduced a registration approach based on the construction of a set of motion-less synthetic reference images through a pharmacokinetic model to correct motion in a sequence of dynamic contrast-enhanced images. This is a departure from registration methods that typically require the inclusion of an intensity correction term to properly align DCE images [2, 82, 83] or the implementation of more computationally expensive groupwise methods [69, 70, 75, 108].

Visually, the least amount of motion artifacts remained in the difference images obtained from the PK-registered images. Such difference images are indicative of the elimination of motion.

Different measures of accuracy were employed to assess the registration results as well as the amount of remaining motion in the final registered set of images. We found that this new method fared best in terms of both global (TRE) and local (SD and MSE of the
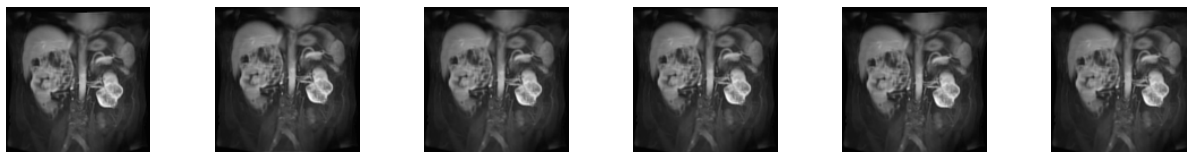
(a) Consecutive template images (DCE sequence with motion)
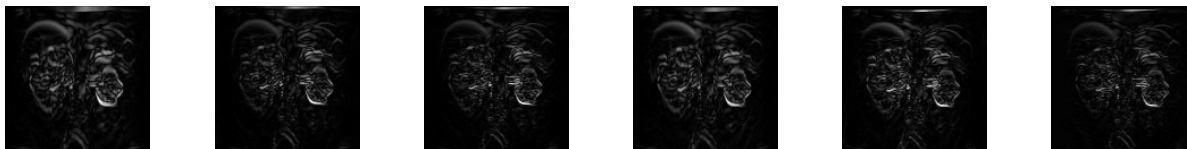
(b) Absolute difference between consecutive template images
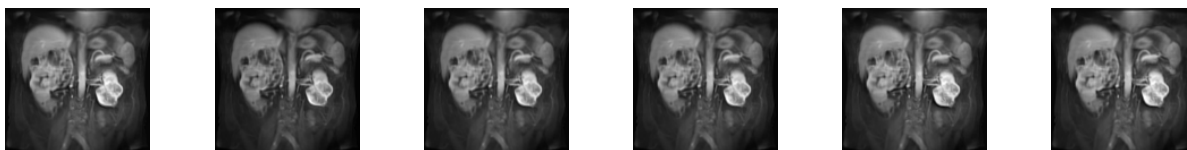
(c) Consecutive FR-registered images
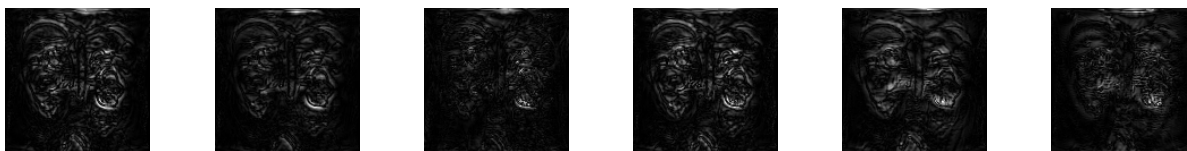
(d) Absolute difference between consecutive FR-registered images
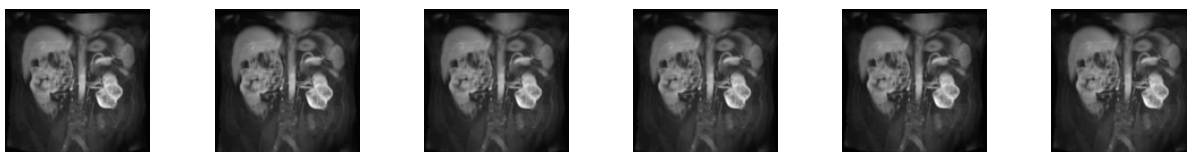
(e) Consecutive GW-registered images
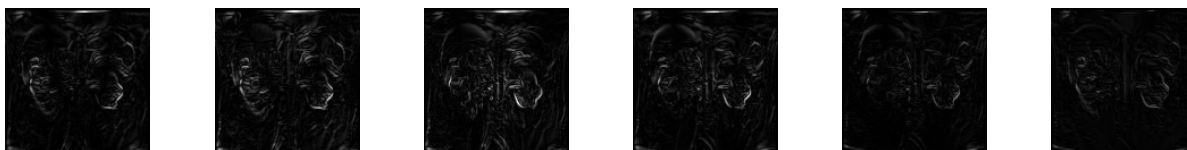
(f) Absolute difference between consecutive GW-registered images

Figure 4.15: Registration results. (a)-(b) Consecutive template images and absolute differences between consecutive template images, (c)-(d) results of floating reference registration, (e)-(f) results of groupwise registration.
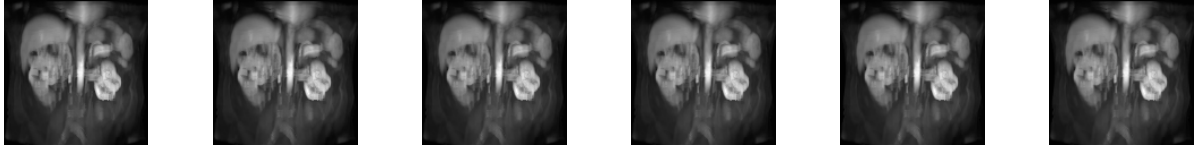
(g) Synthetic reference images
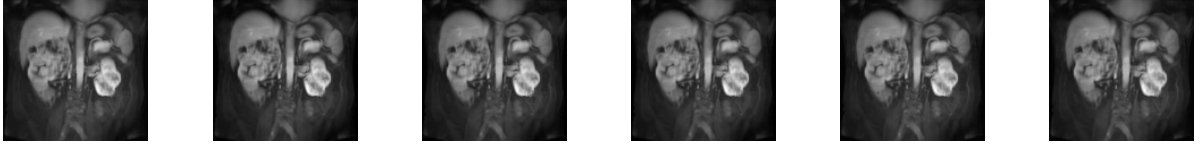
(h) Consecutive PK-registered images
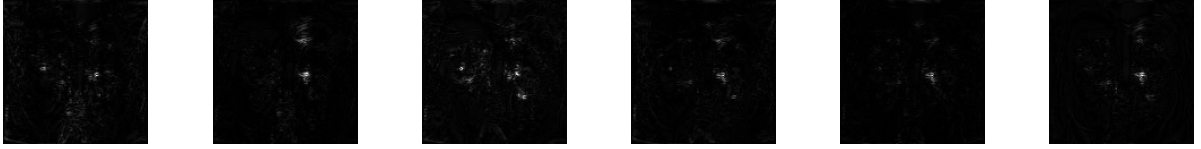
(i) Absolute difference between consecutive PK-registered images

Figure 4.15: (Cont'd.) Registration results. (g) Consecutive synthetic reference images, (h)-(i) results of pharmacokinetic registration.

SI curves) measures of accuracy. The PK TREs were consistently smaller compared to FR and GW-NGF TREs. In terms of the local measures of accuracy, the pharmacokinetic MSEs were also generally lower than the MSEs of the baseline results. In addition, the SI curve SDs was reduced by as much as 83% with the PK method.

Finally, we have successfully used both structural and temporal information to come up with an algorithm for motion correction in a sequence of DCE images. Generating the motionless sequence of reference images that mimic the contrast enhancement of the frame in the sequence through Tofts model and the LMA also helped simplify the registration problem by enabling the correct matching of image features with the use of an easy-to-implement registration distance measure that is based on voxel intensity similarity.

As a logical next step, we plan to further improve the performance of the proposed registration method by enhancing the quality of the generated sequence of synthetic reference images. We plan to achieve this either by imposing adjacency conditions in the

(a) FR - Average TRE

(b) FR - Average SI

(c) GW - Average TRE

(d) GW - Average SI

(e) PK - Average TRE

(f) PK - Average SI
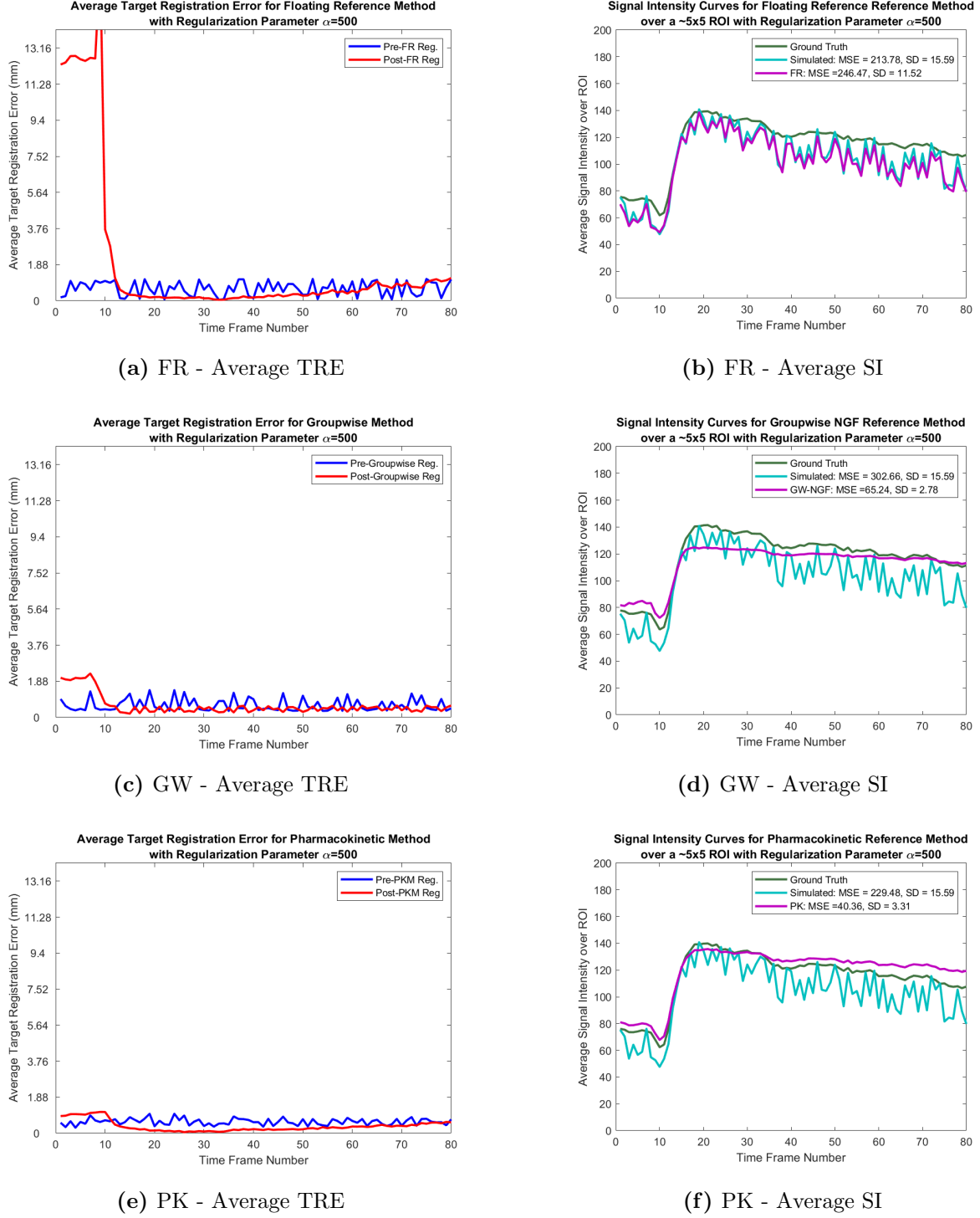
Figure 4.16: Frame-by-frame average TRE and SI curves for $\alpha = 500$. The location of the gridpoints in the template images were tracked in the sequence of both the motion-corrupted (pre-registration) and motion-corrected images. The TREs are the distances of these points from their correct location in the ground truth/motionless dataset.
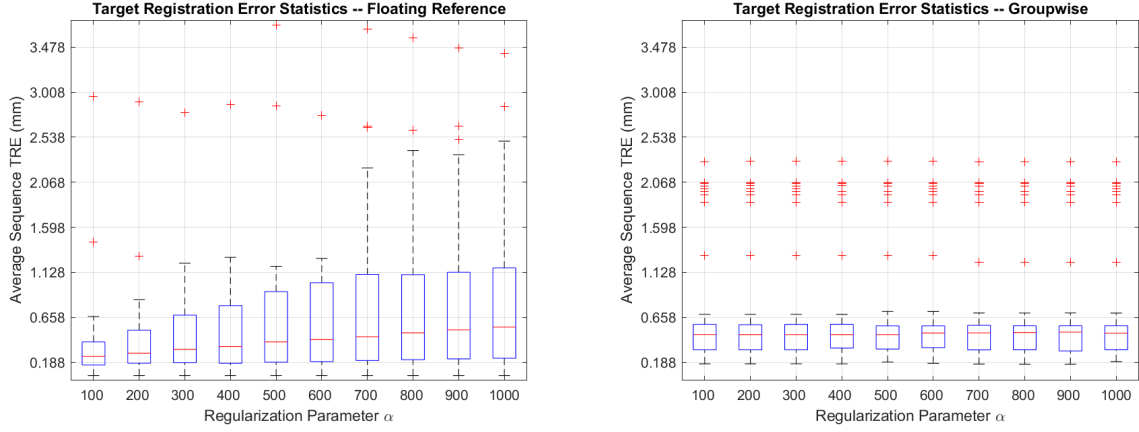
(a) Average TRE Statistics for Floating Reference Approach

(b) Average TRE Statistics for Groupwise Approach
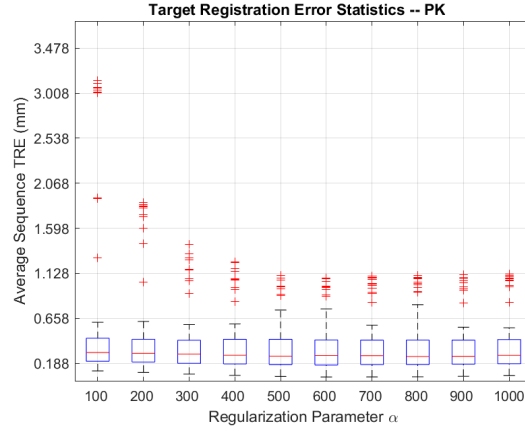
(c) Average TRE Statistics for Pharmacokinetic Approach

Figure 4.17: Boxplot of average target registration error across all frames in the sequence and over different regularization parameters. The boxplots indicate that the median, as well as the inter-quartile range and maximum value of the TREs resulting from the pharmacokinetic method are consistently lower compared to those of the groupwise registration method. This means that after pharmacokinetic registration, the transformed grid points are closer to their correct (ground truth) location.
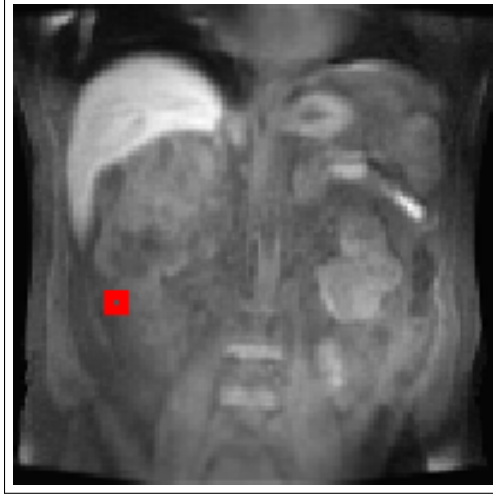
(a) ROI1

(b) ROI2
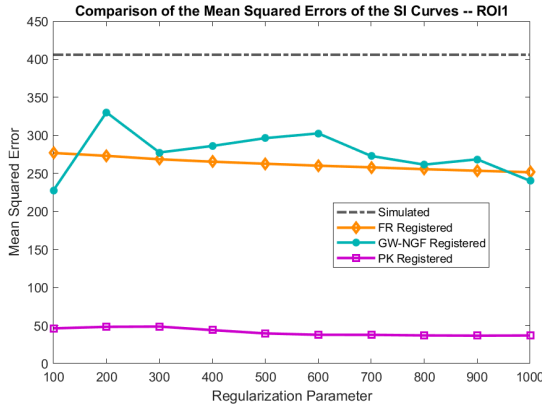
(c) ROI1 SI curve MSEs
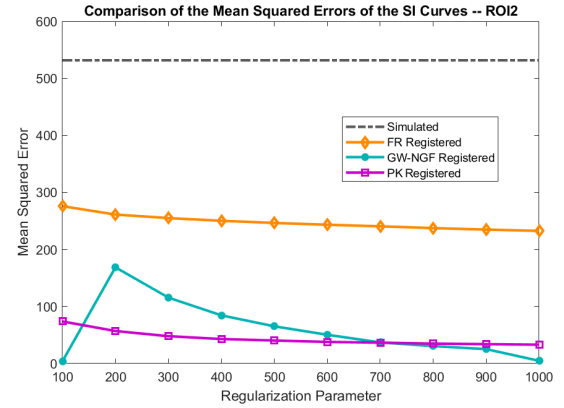
(d) ROI2 SI curve MSEs
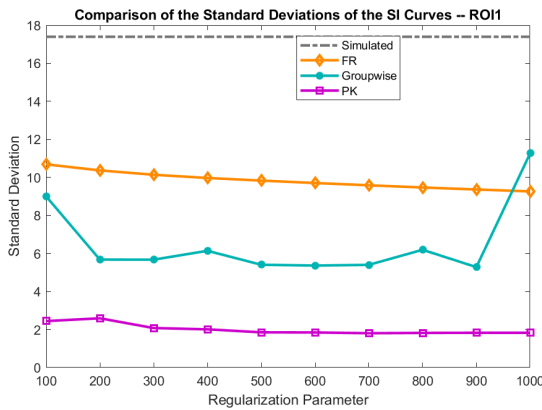
(e) ROI1 SI Curve SDs
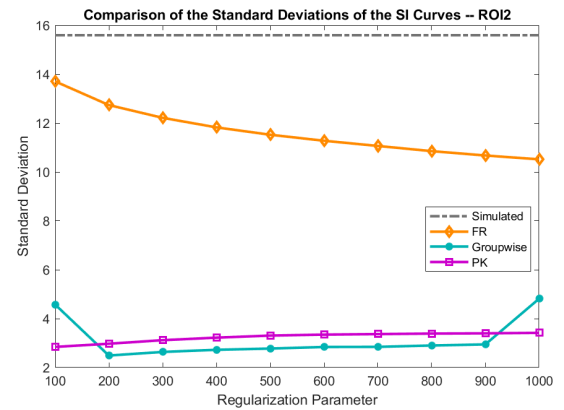
(f) ROI2 SI Curve SDs

Figure 4.18: Comparison of SI curve properties over different values of the regularization parameter α for ROI1 and ROI2. Smaller MSEs imply that the post-registration ROIs are visually similar to the ground truth in terms of the average intensity. On the other hand, a lower SD translates to smoother SI curves and reduced motion in the final registered sequence.

pharmacokinetic model-fitting step or by converting the original motion correction problem into a simultaneous deblurring and registration problem. We also plan to compare the influence of generating reference images through other well-known parmacokinetic models (e.g., the Brix, Kety, or Patlak models [19, 15, 20, 160, 158, 125, 39]) on the quality of registration results.

Chapter 5

Hybrid Landmark- and Intensity-Based Registration

5.1 Introduction

Image registration can generally be classified under two main categories: landmark- and intensity-based. Landmark-based registration can be viewed simply as an interpolation problem, with the optimal transformation being the function passing through each control point while satisfying other constraints, e.g., minimizing the oscillation of the interpolant. A downside of landmark-based registration is that it completely ignores the intensity of the images being registered. As a result, the image overlap away from the landmarks tends to suffer.

On the other hand, intensity-based registration matches corresponding structures between images by minimizing a distance measure that quantifies voxel similarity without the need for guiding landmarks [40]. As such, it usually cannot cope with large geometric deformations [80].

In this chapter, we present a model for intra-modality registration that builds on one of the most commonly used landmark registration methods – Thin Plate Splines – by simultaneously using landmark and intensity information.

Several approaches combining landmark- and intensity-based registration have already been proposed. Eriksson and Astrom introduced in [38] an intensity-based approach that focused on minimizing the Sum of Squared Differences while restricting the solution space to thin plate spline mappings. In [81], the Normalized Gradient Field similarity measure was employed together with the elastic regularizer. Similar restrictions were imposed on the solution space.

Our model eliminates the need for a pre-registration step and also allows the relaxation

of landmark-matching constraints. The aim here is to boost the image similarity and matching of correct landmark pairs even in the presence of landmark localization and/or correspondence errors. We validate the method on short axis and 3D MR images of porcine hearts.

5.2 Proposed Mathematical Model

Let $\mathcal{R}$ and $\mathcal{T}$ be the reference and template images defined on an image domain Ω and suppose that $\{r_j\}_{j=1}^K$ and $\{t_j\}_{j=1}^K$ are K landmarks defined on $\mathcal{R}$ and $\mathcal{T}$, respectively.

We wish to minimize the following functional:

$$\min_f \mathcal{D}^{\text{LM}}[f] + \alpha \mathcal{D}^{\text{INT}}[f] + \beta \mathcal{S}^{\text{TPS}}[f] \tag{5.1}$$

such that f is a thin plate spline.

It has been shown that TPS transformations can be expressed as a linear combination of radial basis functions and an affine correction term. That is, for a d-dimensional registration problem,

$$f^i(x) = \sum_{j=1}^K c_j^i \rho\left(\|x - t_j\|\right) + \sum_{k=0}^d w_k^i \tag{5.2}$$

and satisfies the following for $c_j^i, w_l^i \in \mathbb{R}$, $i \in \{1, \ldots, d\}$, and $l \in \{0, \ldots, d\}$:

$$\begin{cases} c_1^i & + & c_2^i & + & \ldots & + & c_K^i & = & 0 \\ c_1^i t_1^1 & + & c_2^i t_2^1 & + & \ldots & + & c_K^i t_K^1 & = & 0 \\ \vdots & & & \ddots & & & \vdots & \\ c_1^i t_1^d & + & c_2^i t_2^d & + & \ldots & + & c_K^i t_K^d & = & 0 \end{cases} . \tag{5.3}$$

For more context on the necessary conditions in the above system of equations (5.3), we refer the reader to [17, 33, 150, 175] and also Chapter 2.

The term $\mathcal{D}^{\text{INT}}$ denotes the discrete analogue of the SSD between a transformed version $\mathcal{T}[f]$ of the template and the reference $\mathcal{R}$. For instance, in 2D registration, it is

given by

$$\mathcal{D}^{\mathrm{INT}}[f] := \sum_{x \in \Omega} \frac{h}{2} \Big(\mathcal{T}[f(x)] - \mathcal{R}(x) \Big)^2, \tag{5.4}$$

where x refers to a physical point in the image domain Ω, and h refers to the width of the grid constructed from the template and reference image domain.

The term $\mathcal{S}^{\mathrm{TPS}}$ acts as a regularizer that relaxes the landmark matching constraint, thereby controlling the smoothness of the resulting deformation [107].

5.3   Validation

High resolution *ex-vivo* short axis images of porcine hearts first instroduced in Chapter 3 were used for validation. Data acquisition parameters are provided in [134].

5.3.1   Idealized Case

To quantify the performance of our model, we first created an idealized case where neither cardiac nor respiratory motion affects the registration result. Points along the free wall of the right ventricle, the interventricular septum, and the left ventricular myocardium were chosen similar to [121] (see Figure 5.1(a)-(c)). The template image and its landmarks were generated by applying a spline transformation to the reference.

The performance of the model for different values of α and β was investigated under the following three scenarios:

(a) $\mathcal{R}$ (b) $\mathcal{T}$ (c) $|\mathcal{R} - \mathcal{T}|$
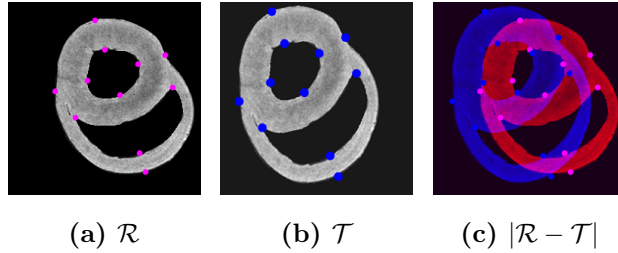
Figure 5.1: Reference and Template Images. (L-R) $\mathcal{R}$, $\mathcal{T}$, and the reference image (red) overlaid onto the template (blue).

Case A. Correct landmark correspondence without any localization error,

Case B. Correct landmark correspondence with a small localization error in one of the template landmarks, and

Case C. Correct landmark correspondence in 10 out of the 11 landmark pairs and a small localization error in one of the template landmarks.

Experiments on data that exhibit the last two scenarios were performed mainly to find out whether the proposed method could compensate for possible deformities and/or reduction in image overlap when an identified landmark is slightly off from its correct position (as in Case B), when a landmark is mistakenly identified as another landmark, or when a combination of both scenarios are present in the data (as in Case C).

5.3.2 Reference-Template Pairs from Different Hearts

We also applied the proposed method on entire 3D volumes (each with 43 landmarks) to assess how well it fuses information from different subjects. All landmarks were automatically selected based on their location with respect to the RV insertion points. Hence, the landmarks located on the epicardial and endocardial surfaces are just approximations (i.e., possibly have localization errors). The additional test images are shown in Figure 5.4.

In all of the experiments, the discrete derivative of each component of the functional in Equation (5.1) was computed with respect to the parameters of the thin plate spline mapping, and the minimization problem was solved through the Newton Method. The complete derivation of the discrete derivatives are provided in Appendix C.

5.3.3 Measures of Accuracy

The match between landmarks pairs was measured by tracking the location of the correct template landmarks t_j^c with respect to their corresponding reference landmarks after reg-

istration and then calculating the maximum component $\left\|\vec{E}\right\|_\infty$ of the vector of distances

$$\left\|\vec{E}\right\|_\infty = \max\left\{\left\|t_j^c - r_j\right\| : j = 1, 2, \ldots, n\right\}. \tag{5.5}$$

In a way, the above quantity gauges how badly the registration is impacted by the landmark errors and how well the inclusion of the intensity and smoothing terms help to align the images in spite of said errors.

Finally, Jaccard similarity indices were used to measure the image overlap before and after registration.

5.4 Results and Discussion

5.4.1 Idealized Case

Shown in Figure 5.1 are the reference and template images used in the experiments, along with the correct location of the landmarks. The pre-registration Jaccard similarity index of the two images is 54%, while the initial maximum entry of the distance vector from the reference to the template landmarks is 24.14mm.

Since TPS registration ($\alpha = \beta = 0$) is widely used in medical image registration, results obtained from blindly applying the technique were used as a baseline for every set of experiments described in the previous section. Shown in Figures 5.2(b) and (c) are the baseline results for when 1 and 2 landmarks errors, respectively, were present in the template data. Observe that deformities were introduced to the registered image due to the wrong placement of landmarks.

As expected, TPS performed well when the correct pairing and locations of the landmarks were used to guide the registration (see Figure 5.2(a)). Image overlap increased by almost forty percent, to 91.24%, and the maximum landmark distance went down to 8.20×10^{-13} mm. Our model yielded similar results for this scenario. We can see from the first column in Figure 5.3 that increasing the magnitude α of the intensity term

(a) Case A   **(b)** Case B   **(c)** Case C   **(d)** $\beta = 0$ **(e)** $\beta = 1$ **(f)** $\beta = 10$

(g) $\alpha = 0$ **(h)** $\alpha = 10^{-5}$ **(i)** $\alpha = 10^{-4}$ **(j)** $\alpha = 10^{-3}$ **(k)** $\alpha = 10^{-2}$ **(l)** $\alpha = 10^{-1}$
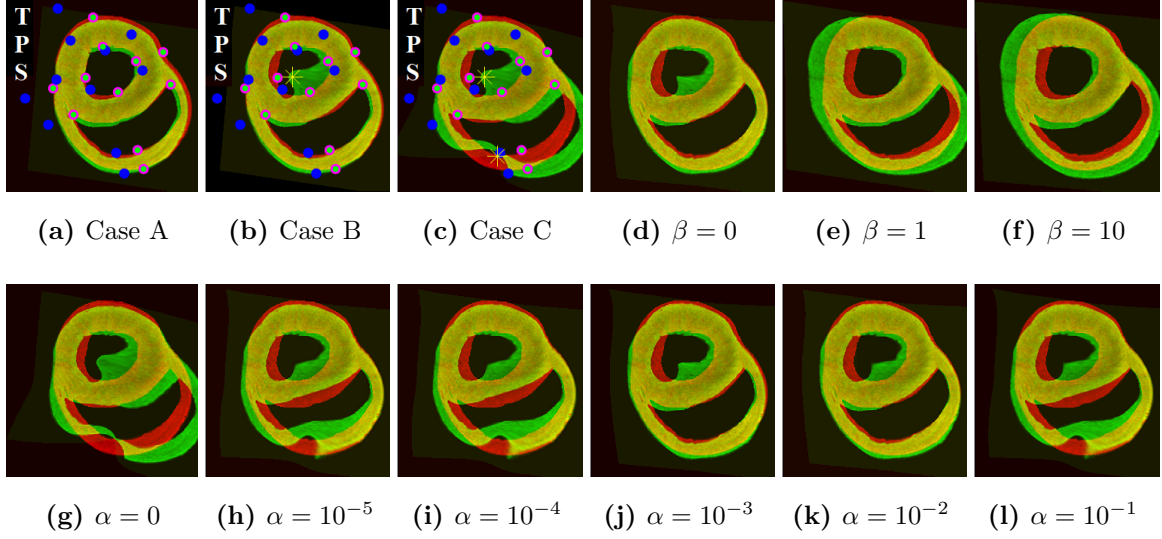
Figure 5.2: Registration Results. (a)-(c) Baseline/TPS results ($\alpha = \beta = 0$), (d)-(f) demonstrates the effect of increasing the magnitude β of the smoothing term (given a fixed $\alpha = 0.01$) on deformities caused by a localization error, (g)-(l) shows the benefit of adding the intensity term to the model. Note that these are fused images of the registered template and the reference. Red=regions exclusively in $\mathcal{R}$, green=exclusively in the registered template $\mathcal{T}[f]$, yellow=regions where the two overlapped.
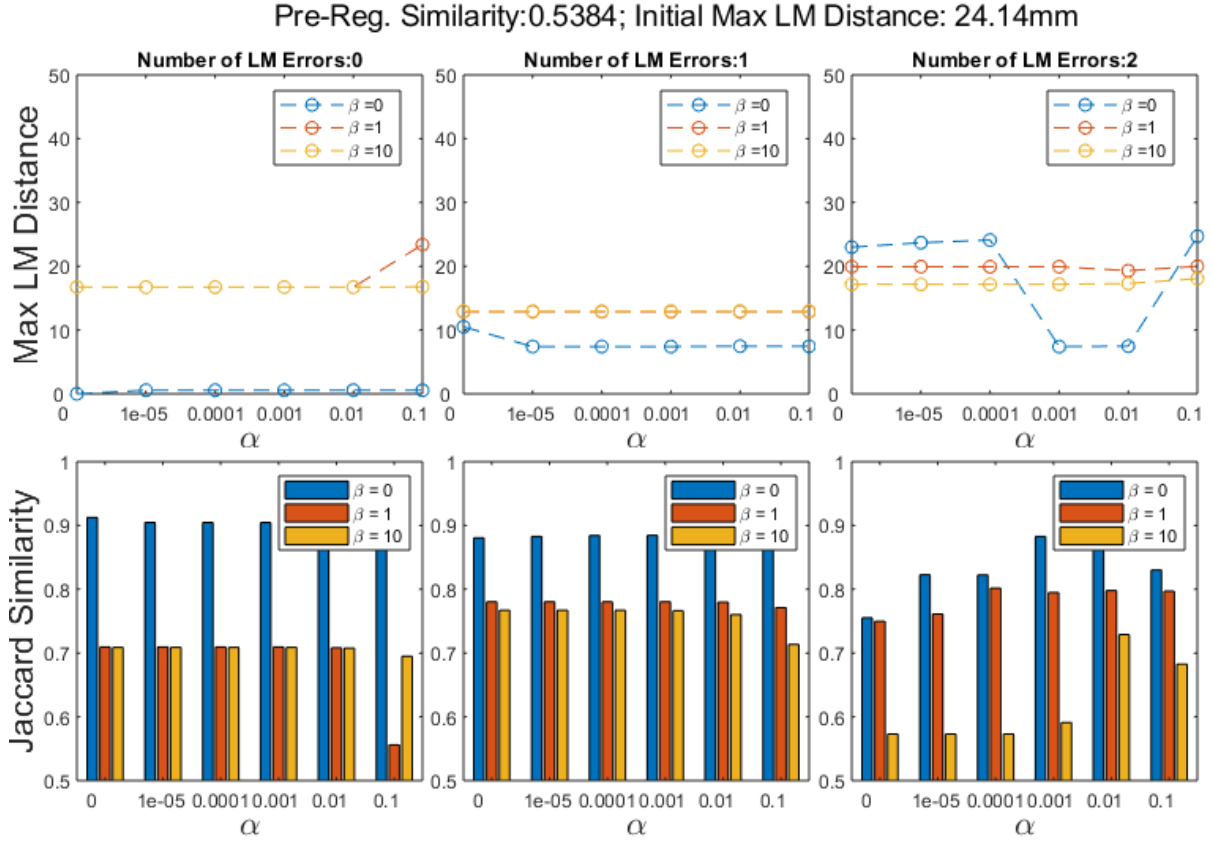
Figure 5.3: Summary of Results. Results of using reference and template landmarks that exhibit (Column 1) no localization error, (Column 2) a small localization error (29.32mm) in one of the template landmarks, (Column 3) correct correspondence in 10 out of the 11 landmark pairs and a small localization error in one of the template ladnmarks. First row gives the max. of the vector of distances (in mm) between reference and correct template landmark pairs. Second row shows the Jaccard coefficients for different values of the model parameters.

resulted in comparable overlaps between the registered template and the reference image. Naturally, relaxing the matching constraint by increasing the value of β gave poor results when there was already an accurate correspondence between landmarks to begin with.

Shown in Figures 5.2(b) and (c) and the last two columns in Figure 5.3 are the results when TPS registration was applied blindly to landmarks with errors. It can be seen that unnatural deformities were introduced to the registered image by the wrong placement of landmarks. Aside from the obvious jump in maximum landmark distance, the post-registration image overlap dropped by 3% and 16% for Case A and Case B, respectively.

For Case B, we see from Figure 5.3 that the final Jaccard similarities when $\beta = 0$ are at par with the baseline result. Improvements resulting from our method are more evident if we look at the maximum landmark distance after adding the intensity term (i.e., by setting $\alpha > 0$). It decreased from 10.50mm to 7.40mm when $\alpha = 0$. More importantly, if we look at Figures 5.2(d)-(f) and compared it against the benchmark in Figure 5.2(b), we can see that the deformity introduced by the landmark error became less pronounced with the inclusion of the intensity term in the model. The deformity even disappeared when the smoothing term was added (i.e., when $\beta > 0$), although with some image similarity tradeoffs.

For Case C, where we have 2 errors – 1 small localization error and 1 incorrect template-reference landmark correspondence – observe from the third column in Figure 5.3 that our model outperformed the baseline for every value of α used and for $\beta = 0.1$. The best overlap and least maximum landmark distance occurred when $\alpha = 0.01$ and $\beta = 0$. This tells us that our model can compensate for landmark correspondence and localization errors. If we look at the results in Figures 5.2(g)-(l) and compare them against the TPS registration result in Figure 5.2(c), we can conclude that adding the intensity term indeed helped to reduce the deformities caused by these errors.

5.4.2   Reference-Template Pairs from Different Hearts

As we mentioned in the previous section, the identified landmarks were merely estimates of points of interest on the endocardium and epicardium with respect to the insertion points. Identifying landmarks in this manner is highly prone to errors both due to large deformations in the heart and variability in cardiac scale and alignment (see Figure 5.4). These factors make the process of selecting the model parameters more challenging.

Aligning the pair of cardiac volumes displayed in Figure 5.4(a)-(b) using the hybrid approach led to a much improved post-registration Jaccard similarity of 99.75%, as shown in Figure 5.4(c). The parameter values that yielded the highest post-registration similarity were $\alpha = 0.01$ and $\beta = 0$.

5.5   Conclusions and Next Steps

Thin plate spline registration provides an effective and computationally efficient way of registering images, provided that correct landmark locations and correspondences between the template and reference are defined. However, identifying landmarks is prone to errors. In the presence of such errors, TPS registration fails to properly register medical images and could introduce unnatural deformities to the transformed template.

In this section, we proposed a novel registration model combining intensity and landmark information to match pairs of 2D and 3D images. The model can be adjusted to relax the TPS landmark-matching constraint and cater to landmark uncertainties. Most importantly, the inclusion of the intensity term helped improve the overlap between the transformed template and reference images.

Our experiments demonstrated that this new method consistently yields good post-registration image overlaps. In addition, while most proposed hybrid registration methods explore their advantages in terms of the imropovement of registration accuracy when perfect landmark correspondences are defined, we went one step further by analyzing the

applicability of our proposed hybrid method in cases where there are significant LM errors in the data. We found that our method outperforms the widely used TPS registration in the presence of landmark localization or correspondence errors.

In the following chapters, we will introduce a fast registration method and a hybrid landmark- and contour- matching model, both of which require automatically detected anatomical points of interest and contour information.

(a) Reference $\mathcal{R}$

(b) Template $\mathcal{T}$

(c) Transformed Template $\mathcal{T}[f^*]$
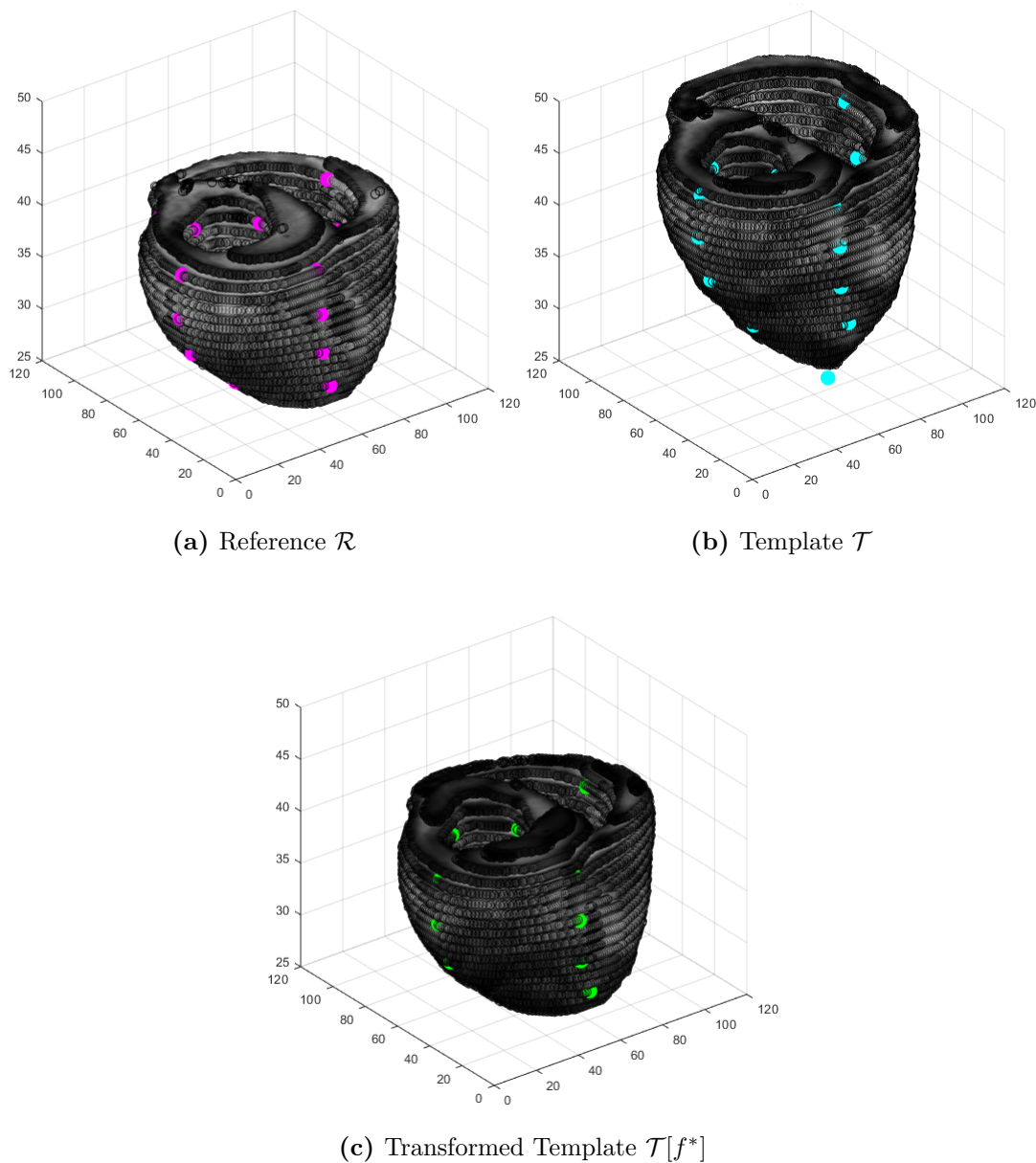
Figure 5.4: Some results from experiments using 3D cardiac MR data with 2 localization errors. (a) Reference, (b) template, and (c) transformed template from experiment with 2 landmark errors. Model parameters used: $\alpha = 0.01$, $\beta = 0$; Pre-reg. similarity: 49.15%; Post-reg. similarity: 99.75%.

Chapter 6

Landmark Detection in Medical Images

Landmark-based registration of medical images can be challenging and prone to errors since the selection of landmarks highly depends on the ability of the physician to mentally integrate information from different images [97]. In addition, some medical images like the heart only has few spatially accurate and repeatable anatomical landmarks [129] to guide the transformations. For instance, in [145], only the two papillary muscles and the inferior junction of the right ventricle were used to rigidly transform cardiac PET and US images. To circumvent the aforementioned issues, point-based registration is typically used either only as a preliminary step to correct scaling and orientation, or in conjunction with an intensity-based approach to improve image overlap, as in [129].

Here, we propose an approach to automatically detect cardiac anatomical landmarks for fast registration. These landmarks will allow the partitioning of the image edges and the identification of an ordered set of contour-approximating landmarks. We will first discuss the landmark detection pipeline and eventually demonstrate its applicability to different medical images.

6.1   Methods

Image features that are normally used in image alignment include corner points, ridges, and edges. Popular methods for feature-point extraction include the Harris edge and corner detector [60], Kanade–Lucas–Tomasi feature tracker [163], Laplacian of Gaussian zero-crossing detector [155], and Canny [24] and Sobel [51, 151] edge detection methods, to name a few.

Our focus in this section is to generate an ordered set of contour-approximating landmarks. To do so, we begin by identifying points of interest (POI) in each contour.

Here, we define the POIs be the points along the contour where the maximum curvature occurs. Several curvature-based feature point detection and shape analysis methods have been proposed [18, 8, 27, 115, 149, 182]. Here, we use a straightforward approach to identifying areas of high curvature that involves the computation of the narrowing or interior angles at every contour-tracing point.

Recall that the curvature κ in $\mathbb{R}^2$ measures how sharply a curve C bends [5] and that maximizing κ is equivalent to minimizing its reciprocal $\rho = 1/\kappa$, more commonly known as the radius of curvature. Finding κ is straightforward provided that the equation describing C is known. For our application, only the pixels tracing contours are known. Thus, computing the curvature entails the additional step of performing a polynomial fit at every point on each contour. On the other hand, calculating ρ involves finding the center of the osculating circle at every $x \in C$ and then calculating the distance of the center from x.

To simplify the problem of finding the POIs, note that the sharpest bends occur where the contour is narrowest (Figures 6.1a-6.1c). Therefore, we can instead focus on measuring the narrowing at every boundary point.

Given an ordered list of connected pixels $C = \{x_k\}_{k=0}^{N-1}$, we define the interior angle of C at pixel x_k as a function of the dot product of two unit vectors

$$\phi(x_k) = \arccos \left[\frac{\overrightarrow{x_k x_{(k+\Delta k)\bmod N}}}{\left\| \overrightarrow{x_k x_{(k+\Delta k)\bmod N}} \right\|} \cdot \frac{\overrightarrow{x_k x_{(k-\Delta k)\bmod N}}}{\left\| \overrightarrow{x_k x_{(k-\Delta k)\bmod N}} \right\|} \right], \tag{6.1}$$

where the window size Δk ($0 < \Delta k < N - 1$ and $\Delta k \in \mathbb{N}$) dictates the points along the curve that make up the interior angle $\phi(x_k)$. More specifically, the interior angle $\phi(x_k)$ at pixel x_k is made up of two rays: one extending from x_k to $x_{k-\Delta k}$, and the other from x_k to $x_{k+\Delta k}$, the pixels that, respectively, precede and succeed x_k in the ordered list of connected pixels by Δk places. See Figures 6.1b-6.1c.

A smaller interior angle corresponds to a smaller radius of curvature or, equivalently, to a larger curvature. Thus, we hypothesize that minimizing the interior angle along a

myocardial contour is a good alternative to locating the POIs. See Figure 6.1.

(a) Curvature and int. ∠s

(b) RV interior angles

(c) LV interior angles

(d) 2- and 3-segment slices

(e) 3-segment LMs

(f) 2-segment LMs
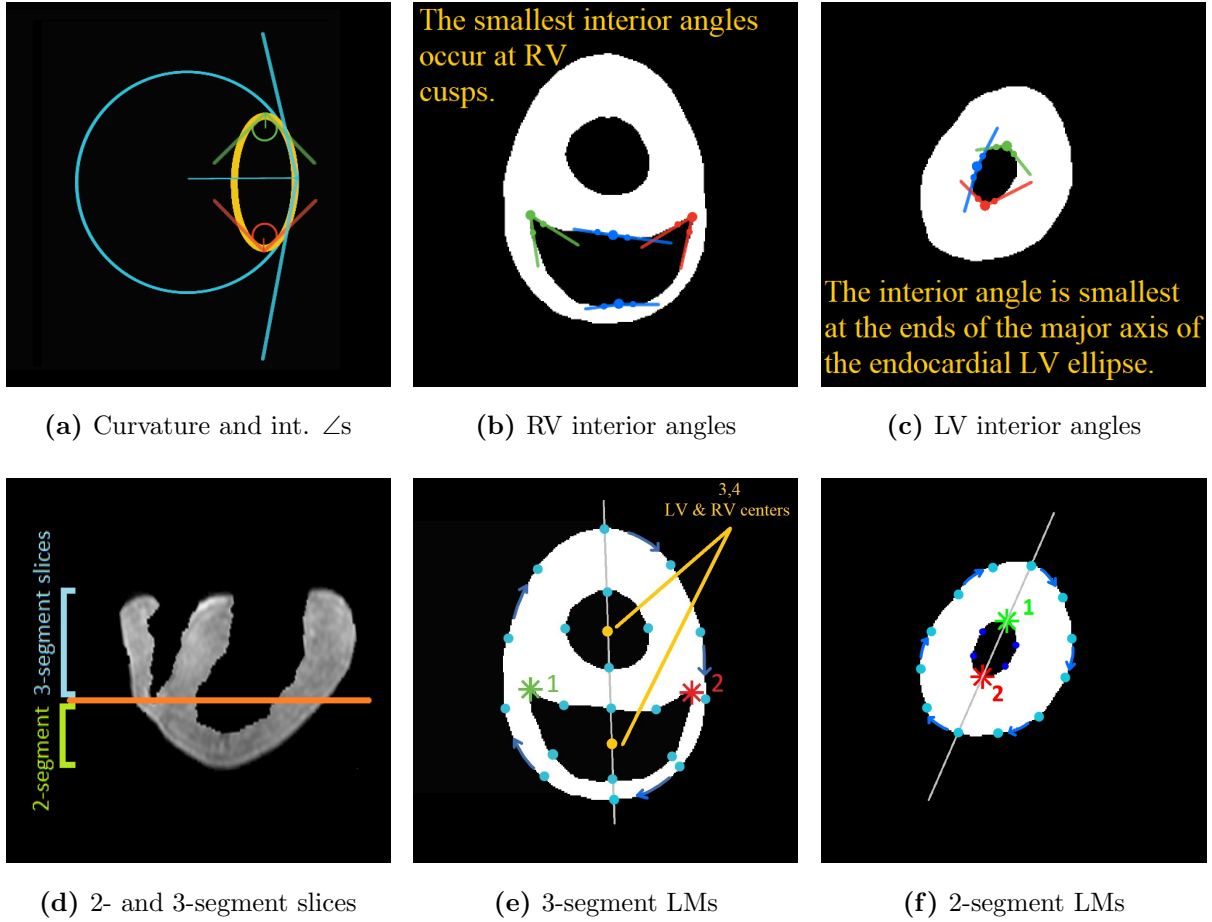
Figure 6.1: Curvature and interior angles. (a) Comparison of curvature, radius of curvature, and interior angles. Osculating circles drawn at different points on an ellipse demonstrate that a high curvature κ corresponds to a small radius of curvature ρ and a small interior angle ϕ, (b)-(c) interior angles in 3- and 2-segment slices, (d) 3- and 2-segment slices in lateral view, (e)-(f) POIs and a sampling of each segment/contour.

6.2 Segmentation and Classification

2D images were binarized to facilitate image segmentation. The Moore-Neighbor tracing algorithm [54] was implemented to detect the holes in the image, the exterior boundaries, and the maximal region of connected pixels tracing each segment.

6.3   Landmark Detection in Cardiac MR Images

We now present each step involved in the detection of contour-approximating landmarks in short-axis cardiac slices. The pipeline (summarized in Figure 6.2) starts with the segmentation and classification of the epicardial and endocardial regions. These steps utilize prior shape knowledge about the structures of the myocardial segments. In the final step, an ordered sampling of each contour is obtained through the location of points of interest (POIs) in the ventricles. The process of locating the POIs will be discussed in detail in Section 6.3.2.

We will also extend our proposed landmark detection scheme to generate surface-approximating landmarks for 3D cardiac MR volumes.
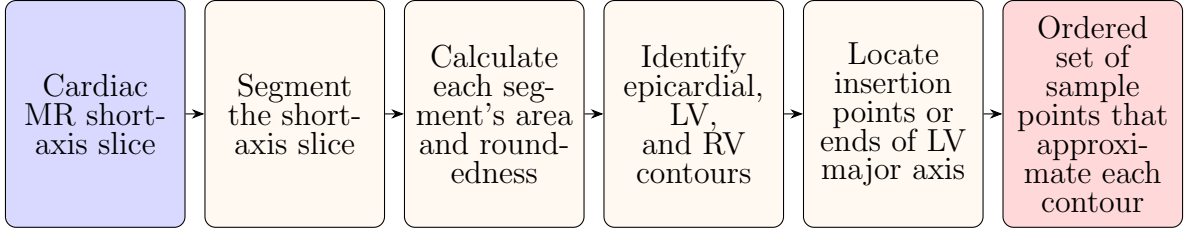
Figure 6.2: Landmark detection in short-axis cardiac images.

6.3.1   Contour Classification

Following the myocardial segmentation through the Moore-Neighbor tracing algorithm [54], the myocardial contours were classified into one of three categories (epicardial, endocardial LV or RV contours). The following assumptions on myocardial segments were employed to label the segmented regions:

   a. Healthy epicardial and LV endocardial regions possess elliptical contours.

   b. RV contours are lune-shaped.

In conjunction with these shape priors, we also calculated the area and roundedness of each segment. The largest region is automatically classified as the epicardium. In basal

and mid-cavity slices (see Figure 6.3), the LV endocardium is differentiated from the RV through the roundedness measure R. It is given by

$$R = \frac{4\pi A}{P^2},$$
(6.2)

where A and P denote the area and perimeter of a region, respectively. Note that R-values range from 0 to 1 (circle). The segment with the smallest R-value is labeled as the RV because RVs are typically crescent-shaped, while LV cross sections resemble ellipses. On the other hand, in binarized apical slices where only the LV endocardial and the epicardial contours are visible, the smaller region is classified as the LV endocardium.
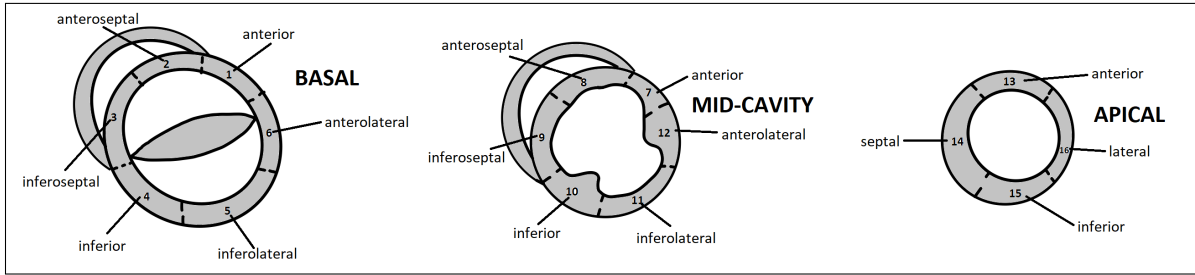
Figure 6.3: Classifications of short-axis slices. Image adapted from [25].

6.3.2 Landmark Detection in 2D Short-Axis Images

To generate an ordered set of contour-approximating landmarks, we begin by identifying two points of interest in each slice. These 2 points will partition each myocardial segment into halves, which in turn, will allow us to define a starting and end point for each partition, divide each partition into shorter arcs of equal length, and identify an ordered set of pixels that ultimately approximate each contour. Again, we define the POIs to be the points along the ventricular contours where the maximum curvature occurs.

As a consequence of the definition of the curvature κ, POIs in short-axis cardiac images vary depending on the presence (or absence) of a cross section of the RV in the slice as follows.

A. Basal and mid-cavity slices

On the upper slices of the heart where cross sections of the RV are visible, the POIs are given by the RV insertion points. Visually, these points correspond to the cusps of the crescent-shaped RV contour and consequently divide it into two arcs. After finding the insertion points using the method described above, we then bisect the LV and the epicardial contours by locating the centers of the LV and RV, and then passing a straight line through their centers. The points along the LV (epicardial) contour that intersect this line are labeled as the first pixels in the ordered sampling for their respective halves of the LV (epicardial) contour. These steps are shown in Figure 6.1e.

B. Apical slices

On apical slices where only the LV and epicardial contours are present, the bisection of the myocardial contours begins with the identification of the ends of the major axis of the elliptic LV contour. We remark that the curvature-based POI detection method described above is still applicable in this case because the maximum curvature in every ellipse occurs at the ends of its major axis. In this case, a line passing through the two LV POIs is used to bisect the epicardial and endocardial contours, again enabling the identification of a starting and an end point for each contour. See Figure 6.1f.

Finally the contour-approximating landmarks in each bisected arc are obtained by sampling the ordered set of connected pixels. The number of sample points is user-specified.

6.3.3   Landmark Detection in 3D Cardiac Volumes

Provided that the hearts were scanned as specified in Section 2, the 3D analogue of the landmark detection method presented in the previous section merely involves the extra step of identifying the short-axis slices from which contour-approximating landmarks are to be generated.

Suppose that

a. T denotes the slice thickness,

b. the two-segment (apical, see Figure 6.1d) slices occupy levels $z \in [a, b]$,

c. the three-segment (basal and mid-cavity) slices are on levels $z \in [b + T, c]$,

d. m and n refer to the user-specified number of sub-intervals in the levels spanned by the two-segment and the three-segment slices.

Then the sampling increments in the vertical direction for the two-segment and three-segment slices, respectively, are given by

$$\Delta m = \frac{b - a}{m} \quad \text{AND} \quad \Delta n = \frac{c - (b + T)}{n}, \tag{6.3}$$

and the slices where the contour-approximating landmarks are to be identified are $z \in \{a, \ a + \Delta m, \ \ldots, \ b\} \quad \text{AND} \quad z \in \{(b + T), \ (b + T) + \Delta n, \ \ldots, \ c\}.$

Once the sampling slices are determined, the same landmark detection pipeline discussed in the previous section is implemented on each sampling slice. Collectively, the landmarks from these slices approximate the surface of the cardiac volume. Examples demonstrating the placement of automatically detected landmarks in cardiac volumes are shown in Figure 6.4.

6.3.4   Experiments

Both 2D and 3D cardiac MR images were used to validate the proposed pipeline. The use of images of explanted hearts in our experiments was advantageous because it helped
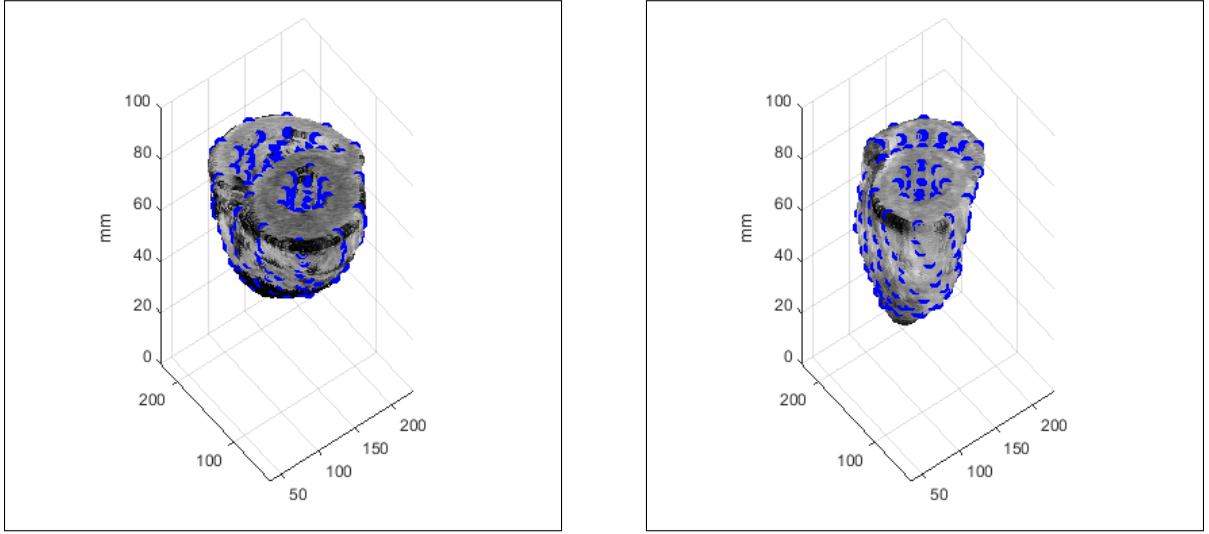
Figure 6.4: Examples of automatically detected surface-approximating landmarks in cardiac volumes.

avoid motion artefacts. It also simplified the heart segmentation step since no other structures were present.

For both 2D and 3D experiments, landmarks were located using the method discussed in Section 3. Note that in order for the proposed fast registration pipeline to work, a one-to-one correspondence between the sets of reference and template landmarks has to be defined. To do this, the user-specified number of sampling slices (m and n) and the number of contour-approximating points along the short-axis myocardial contours (epicardium, LV, RV) have to be the same for the reference and template hearts.

Thin Plate Spline (TPS) registration was then used to align the hearts, with the automatically detected landmarks acting as the control points. To compute the accuracy of the registration results, Dice coefficients were compared before and after registration. Elastic registration (ER) was also implemented using the FAIR toolkit [107] in Matlab to provide a benchmark for our registration results. Recall that the same intensity-based SSD-elastic registration method was used in the groupwise registration framework we implemented in constructing the cardiac atlas in Chapter 3. Choosing it as our benchmark allowed us to measure the tradeoff in computational runtime gained through

the implementation of the proposed landmark-based fast registration pipeline.

6.3.5   Results and Discussion

The accuracy of the proposed interest detection method was assessed by calculating the ratio of the total number of slices with correctly identified interest points to the total number of two-cluster (apical) and three-cluster (basal or mid-cavity) slices per heart. Depending on the slice classification, we determined whether the ends of the LV major axes or the RV insertion points were indeed correctly detected by the method. The results are tallied in Table 6.1, and exemplary visual results for cardiac POI detection are displayed in Figure 6.5. All POIs across every short-axis slice in 6 out of $N = 8$ hearts in the dataset were correctly identified. Overall, the POI detection accuracy across all 8 hearts is 98.93%. This indicates that the method provides a simple yet promising alternative to locating points along the edges of an image that correspond to regions of high curvature. Performing the 2D myocardial segmentation and classification steps of the pipeline took an average of 0.10 seconds per heart (see Table B.1 in Appendix B).

Shown in Figures 6.6a-6.6c are exemplary results obtained after TPS registration was applied on pairs of short-axis slices. The top row shows the pre- and post-registration image overlap of the template with the reference image. Note that the use of automatically detected landmarks resulted in better post-registration image similarity, demonstrated by the difference image $|\mathcal{R} - \mathcal{T}[f]|$ being close to null.

The proposed fast registration approach also proved to be effective in registering 3D volumes of porcine hearts. All fifty-six possible reference-template pairings in our dataset of eight hearts were considered. Some of the results are displayed in Figures 6.6d-6.6e, and the complete tabulation of DSCs is in Table 6.3. Our method yielded consistently accurate results despite the high variability in cardiac size and surface curvatures present in our dataset. Statistically, 46 of the 56 (82.14%) image pairings that were registered using our proposed pipeline had resulted in DSCs that were comparable (i.e., within a 5%

margin of error) to the baseline elastic registration results [112, 113, 114]. Notably, an additional 8 out of the 56 reference-template pairings (or 14.28%) of our results improved on their corresponding baseline DSC by at least 10%.

We also calculated the average change in runtime (measured in seconds) over all reference-template pairings between the two registration methods. We found that the TPS, when paired with the automatically detected landmarks on the original cardiac volumes, was approximately 65% faster compared to implementing multi-level elastic registration [107] on downsampled versions of the reference and template volumes. This amounts to an 11-minute runtime speedup. For a detailed tabulation of the runtime tradeoff obtained from switching from intensity-based elastic registration to the proposed fast registration pipeline, refer to Table 6.4.

	Interest Point Detection in Short-Axis Slices							
	Heart1	Heart2	Heart3	Heart4	Heart5	Heart6	Heart7	Heart8
Total no. of apical slices	5	7	7	9	6	6	6	8
Apical slices with correctly ID'd POIs	5	6	7	9	6	6	6	8
Total no. of basal/mid-cavity slices	24	22	26	41	37	25	24	28
Basal/mid-cavity slices with correctly ID'd POIs	22	22	26	41	37	25	24	28
% Slices with correctly ID'd POIs	93.10%	96.55%	100%	100%	100%	100%	100%	100%
Overall accuracy	98.93%							

Table 6.1: Interest point detection accuracy. The accuracy of the proposed interest point detection method was calculated as the ratio of the total number of slices with correctly identified points of interest to the total number of apical, mid-cavity, and basal slices.

6.4   Landmark Detection in Other Medical Images

We also tested the proposed POI detection method to identify guiding landmarks in other medical data, namely 2D hand Xray images, a mouse brain scan, and some sinus/brain CT and MR images. As shown in Figure 6.7, the approach was able to accurately locate points where sharp turns in the contour of the medical images occur. More specifically,
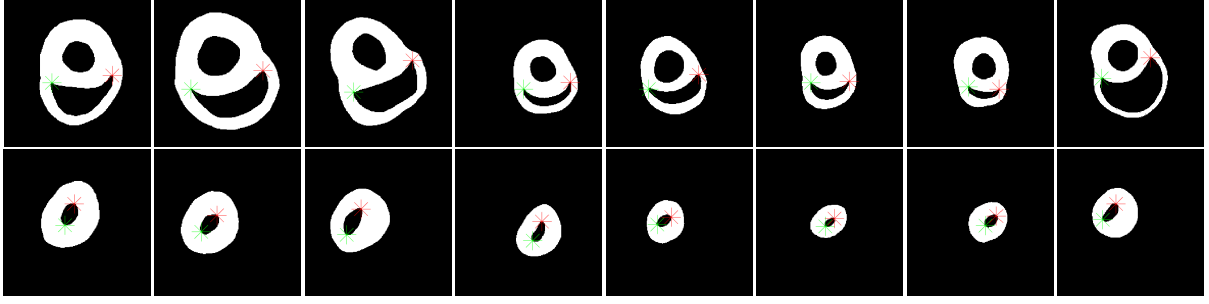
Figure 6.5: Interest point detection in short-axis cardiac images. Points of interest (* and *) in basal/mid-cavity slices are given by the RV insertion points, while POIs in apical slices are defined to be the ends of the major axis of the elliptic LV contour.

		Pre-Registration Dice Similarity Coefficient							
		Template Heart							
		Heart1	Heart2	Heart3	Heart4	Heart5	Heart6	Heart7	Heart8
	Heart1	1.00	0.57	0.58	0.27	0.44	0.46	0.42	0.55
	Heart2	0.57	1.00	0.69	0.21	0.34	0.30	0.28	0.41
Reference Heart	Heart3	0.58	0.69	1.00	0.26	0.43	0.31	0.28	0.59
	Heart4	0.27	0.21	0.26	1.00	0.26	0.24	0.34	0.20
	Heart5	0.44	0.34	0.43	0.26	1.00	0.43	0.36	0.49
	Heart6	0.46	0.30	0.31	0.24	0.43	1.00	0.73	0.34
	Heart7	0.42	0.28	0.28	0.34	0.36	0.73	1.00	0.28
	Heart8	0.55	0.41	0.59	0.20	0.49	0.34	0.28	1.00

Table 6.2: Reference-template image similarity before registration, measured in terms of the Dice similarity coefficient.

all the fingertips and the cusps in between adjacent fingers were correctly identified in the hand data. Prominent points of high curvature within the mouse and human brains were also accurately identified by the method.

(a) 2D - Sample Result 1

(b) 2D - Sample Result 2

(c) 2D - Sample Result 3

(d) 3D - Sample Result 1

(e) 3D - Sample Result 2
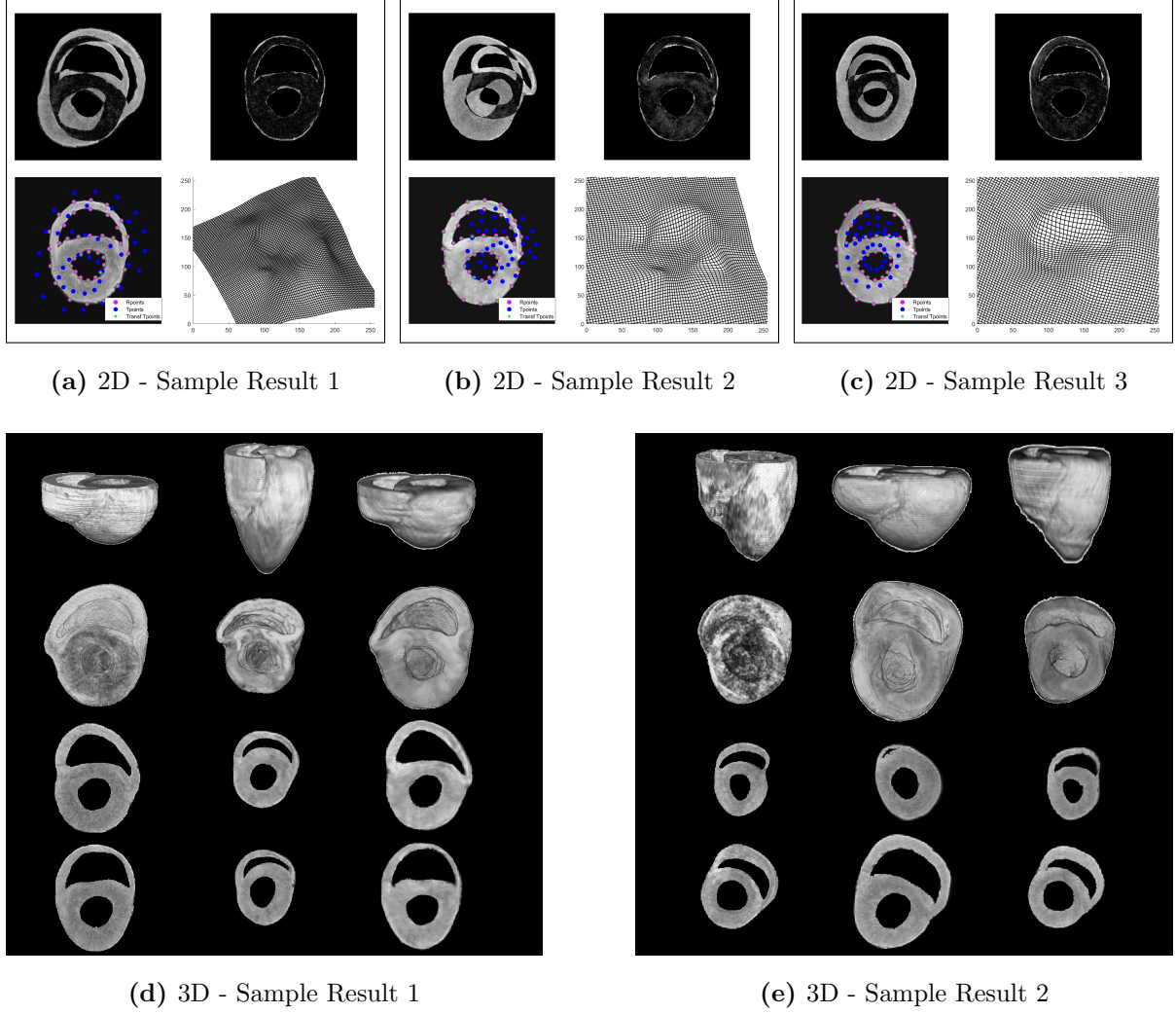
Figure 6.6: 2D and 3D TPS registration using automatically detected landmarks. (a)-(c) Top row: Difference images before and after registration, Bottom row: Registered template image and optimal transformation; (d)-(e) First col: Different views of the reference volume, Second col: Template, Third col: Registered template.

6.5 Conclusions and Future Work

In this work, we presented the mathematical framework behind each step in a fast cardiac image registration pipeline. The proposed definition of interest points based on shape priors and the classification of short-axis slices enabled the the strategic location of landmarks on the reference and template images, which ultimately guided the registration

		Post-Registration Dice Similarity Coefficient														
		Template Heart														
		Heart1		Heart2		Heart3		Heart4		Heart5		Heart6		Heart7		Heart8	
		ER	TPS	ER	TPS	ER	TPS	ER	TPS	ER	TPS	ER	TPS	ER	TPS	ER	TPS
Reference Heart	Heart1	1.00	1.00	0.95	0.94	0.95	0.93	0.96	0.94	0.96	0.93	0.96	0.94	0.94	0.93	0.92	0.94
	Heart2	0.97	0.93	1.00	1.00	0.97	0.94	0.44	0.93	0.95	0.93	0.97	0.93	0.88	0.92	0.95	0.93
	Heart3	0.97	0.93	0.97	0.93	1.00	1.00	0.59	0.94	0.96	0.94	0.97	0.93	0.96	0.92	0.95	0.93
	Heart4	0.97	0.93	0.97	0.93	0.97	0.93	1.00	1.00	0.97	0.94	0.97	0.94	0.97	0.94	0.94	0.92
	Heart5	0.98	0.92	0.97	0.91	0.97	0.92	0.92	0.94	1.00	1.00	0.98	0.93	0.96	0.92	0.94	0.94
	Heart6	0.96	0.92	0.95	0.92	0.95	0.94	0.96	0.95	0.96	0.95	1.00	1.00	0.96	0.93	0.93	0.94
	Heart7	0.95	0.93	0.95	0.93	0.95	0.94	0.95	0.95	0.96	0.95	0.98	0.95	1.00	1.00	0.92	0.93
	Heart8	0.82	0.89	0.89	0.89	0.83	0.89	0.16	0.90	0.81	0.92	0.78	0.90	0.53	0.88	1.00	1.00

Table 6.3: Dice similarity coefficient after elastic (ER) and TPS registration.

		% Change in Runtime							
		Template Heart							
		Heart1	Heart2	Heart3	Heart4	Heart5	Heart6	Heart7	Heart8
Reference Heart	Heart1	0	-77.07	-77.96	-65.28	-70.29	-79.86	-72.55	-77.66
	Heart2	-67.85	0	-67.8	-55.56	-64.50	-69.37	-80.27	-80.13
	Heart3	-69.37	-71.45	0	-54.19	-67.58	-76.36	-67.09	-84.37
	Heart4	-59.86	-9.51	-47.55	0	-66.78	-72.12	-32.77	-80.68
	Heart5	-63.76	-67.86	-65.82	-55.06	0	-71.89	-69.54	-85.64
	Heart6	-60.57	-51.12	-56.61	-57.17	-61.24	0	-77.14	-78.33
	Heart7	-66.48	-67.73	-62.23	-59.93	-63.03	-74.68	0	-82.29
	Heart8	-74.55	-78.46	-73.43	-50.79	-81.37	-56.92	-58.55	0

Table 6.4: Runtime tradeoff resulting from the proposed interest point and registration pipeline.

process.

   Our holistic approach was able to successfully carry out the accurate segmentation and classification of myocardial regions, the detection of surface-approximating landmarks,

(a) Hand Xray   (b) Hand Xray   (c) Mouse brain

(d) Sinus CT   (e) Head CT   (f) Brain MRI   (g) Brain MRI
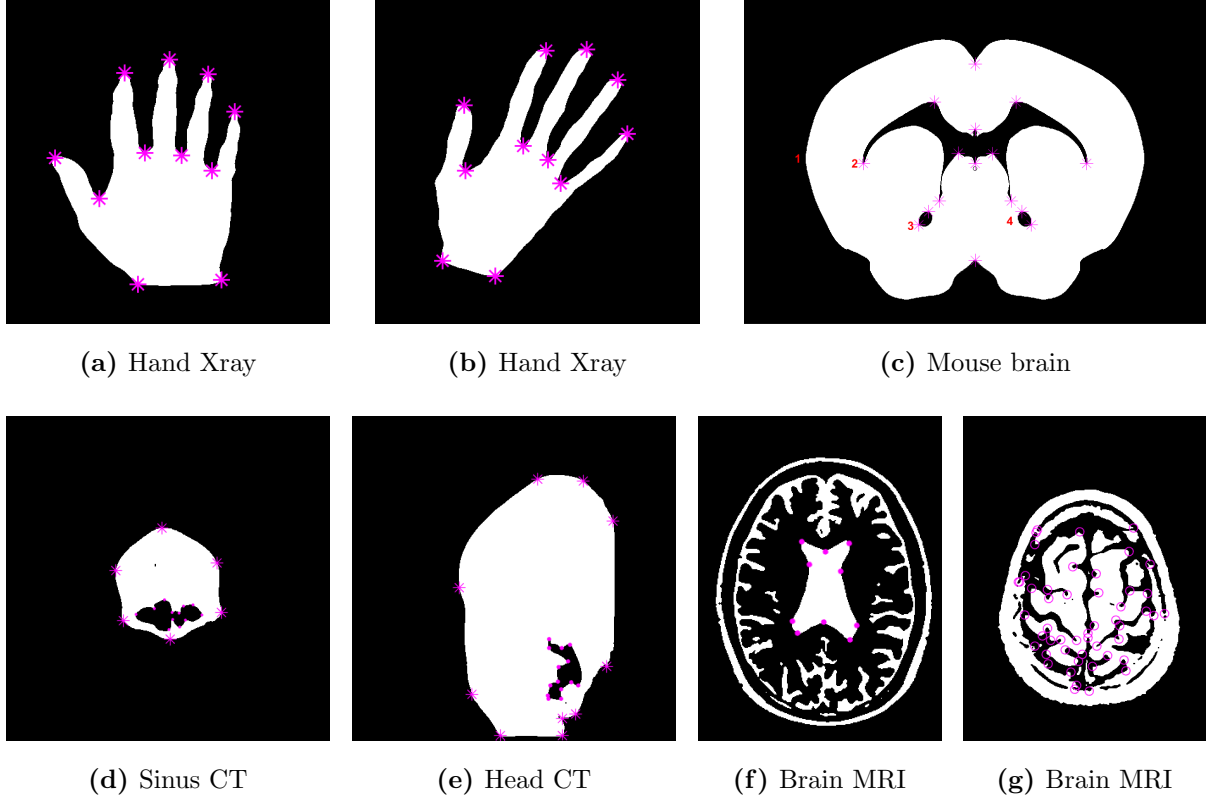
Figure 6.7: Detection of POIs in other medical images. The images above are binarized versions of (a)-(b) hand Xrays from [4, 107], (c) a pre-processed mouse brain from the Allen Adult Mouse Brain Atlas (raw image can be found here), (d)-(e) coronal and sagittal views of sinus/head CT scans and (f)-(g) axial T1-weighted and fluid-attenuated inversion recovery (FLAIR) of brain MR images.

and the implementation of a point-based registration method to align pairs of cardiac images with minimal user input.

Experiments using the automatically detected landmarks together with Thin Plate Spline registration demonstrated that our proposed method consistently yields accurate registration results that are comparable to those from an intensity-based elastic registration scheme. In addition, the computational runtime was reduced. We conclude that our pipeline provides a fast but still an effective alternative to intensity-based registration methods.

We have also demonstrated the applicability of the interest and contour-approximating

point detection scheme to other medical images that exhibit one or more structures with prominent curvature.

Future work includes the improvement of the segmentation and classification steps to allow the proposed pipeline to accommodate the co-registration of *ex-vivo* and *in-vivo* cardiovascular MR images. In line with this, we also aim to make landmark detection in 3D cardiac images more robust by including an LV chamber ellipsoid-fitting as a pre-processing step. This would allow the extension of the interest point detection method to accommodate cardiac volumes that were imaged with a significant tilt relative to the z-axis.

Chapter 7

Landmark- and Contour-Based Registration

Thin plate spline (TPS) data interpolation and approximation are a spline-based technique that has been applied successfully in various fields such as medical imaging, oceanography, geosciences, and shape analysis in general [167, 88, 33, 31, 107].

As a landmark-based registration technique, the use of TPS transformations to describe a non-rigid deformation results to a system of equations that have a closed-form solution [107]. In addition, it produces physically relevant smooth transformations.

While the implementation of a TPS approach is convenient and straightforward, the method comes with some drawbacks. Similar to other landmark-based registration methods, image similarity tends to suffer away from landmarks [40]. Visually, this could result to abnormalities (e.g., unnatural bending, incorrect scaling of image features) in the registered image (see Figure 7.1c).

Naturally, one could consider increasing the number of landmark correspondences in order to improve image overlap between the reference and registered template. Thin plate splines, however, are radial basis functions that have global support. This means that sample points act both as knots and interpolating points, which could then result to a number of computational issues. First, increasing the number of landmarks would involve the inversion of a TPS kernel matrix – an operation of order $\mathcal{O}(K^3)$, where K is the number of landmark pairs. Increasing the number of landmarks also leads to an increase in the condition number of the TPS kernel matrix that could likewise translate to deformities in the registered image as in Figures 7.1d-7.1f.

Figure 7.1d is the result of solving a TPS system with 58 interpolation conditions. Meanwhile, the TPS-registered images in Figures 7.1e and 7.1f suffer from stretching artefacts. More specifically, the metacarpophalangeal joints at the base of the middle

finger in both images appear stretched significantly more than the original template image. The joint at the base of the ring finger in Figure 7.1e also appears curved even when the external finger contour is straight.

Ill-conditioning also occurs in the presence of data points that are too close together [139]. In such a case, exact interpolation is sensible only if the intensity values at the two close data sites are themselves close [150].

Here, we aim to address these issues associated with TPS registration. We will introduce a hybrid registration model that pairs with the landmark detection method we proposed in Chapter 6. The model only requires a small number of feature points as centers of the TPS radial basis functions. It also incorporates approximate contour information to increase registration accuracy and avoid the visual deformities commonly induced by a purely TPS-based approach in the transformed template.

Lastly, since landmark selection in medical images is typically done manually and is thus susceptible to errors, it is important for a registration model to cater to such localization errors. We will demonstrate that the model outperforms the TPS approach in such cases.

7.1   Proposed Landmark and Contour-Matching Model

Let $\mathcal{R}$ and $\mathcal{T}$ be the reference and template images with exact (major) landmarks $\{r_j\}_{j=1}^K$ and $\{t_j\}_{j=1}^K$, respectively. Also, let $\left\{\overset{*}{r}_j\right\}_{j=1}^L$ and $\left\{\overset{*}{t}_j\right\}_{j=1}^L$ be an ordered set of sampling points that trace the contours of an object of interest present in $\mathcal{R}$ and $\mathcal{T}$. We aim to solve the optimization problem

$$f^* = \arg\min_f \mathcal{D}^{\mathrm{LM}}[f] + \alpha \mathcal{C}[f] \tag{7.1}$$

in which f is a thin plate spline transformation 2.19.

For a 2-dimensional registration problem, the optimal solution of (7.1) has the form

(a) Reference

(b) Template

(c) Transformed Template with bending

(d) Folding issue

(e) Stretched (middle) and bent (fourth) metacarpophalangeal joint

(f) Internal Deformities

(g) Sample TPS Transf. 1

(h) Sample TPS Transf. 2

(i) Sample TPS Transf. 3
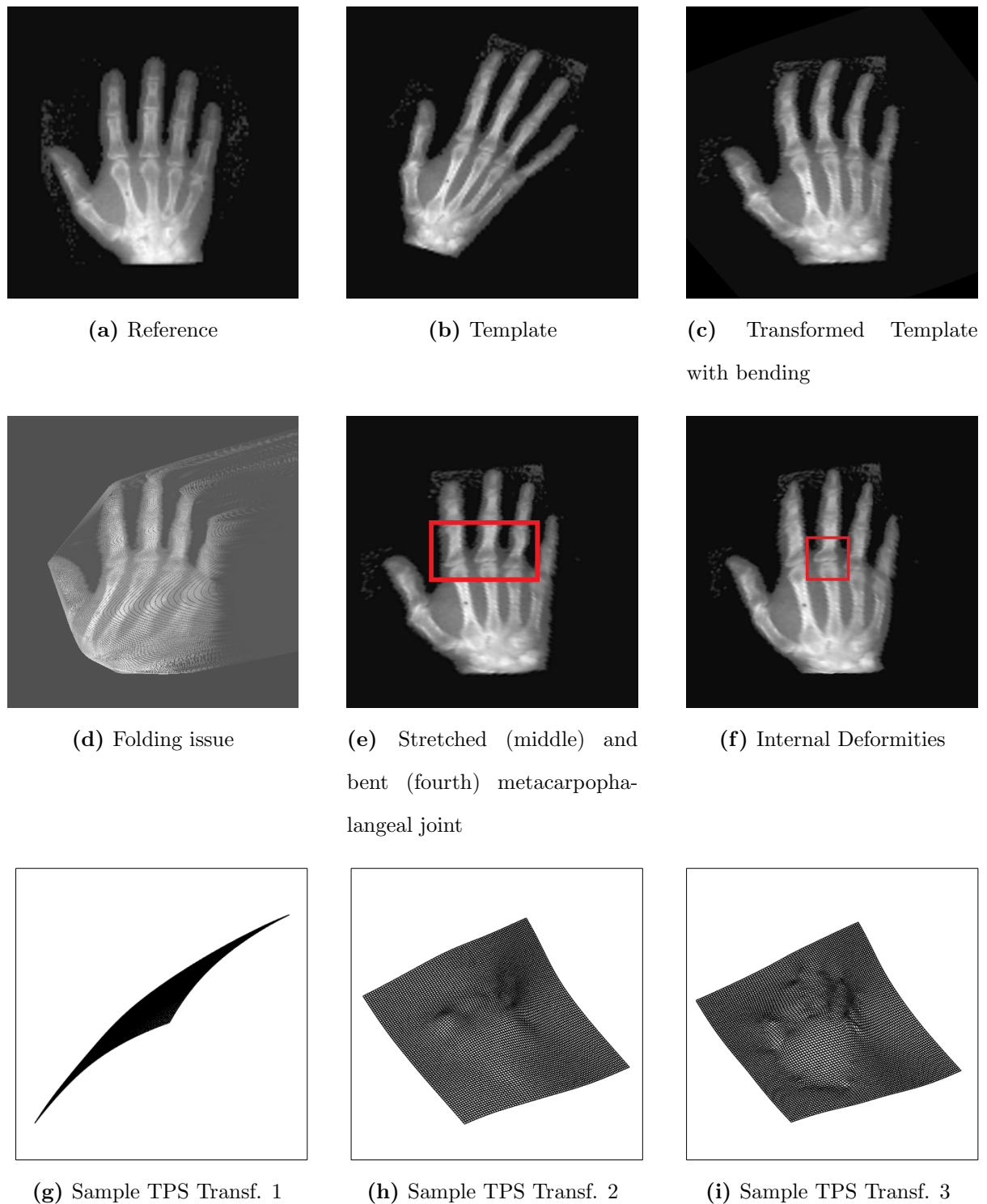
Figure 7.1: Drawbacks of thin plate spline registration in medical imaging. (a) Reference, (b) template, (c) unnatural bending in registered image, (d) folding issue in ill-conditioned TPS systems, (e)-(f) deformities induced by the TPS transformations with too many knots, (g)-(i) TPS transformations associated with the registered images in (d)-(f).

$f^* = [f^1, f^2]^T$, where

$$f^i(x) = \sum_{j=1}^{K} c_j^i \|x - t_j\|^2 \log \|x - t_j\| + w_0^i + w_1^i x^1 + w_2^i x^2 \tag{7.2}$$

and the transformation parameters c_j^i, $w_l^i \in \mathbb{R}$ satisfy the constraints in Equation (2.21) for $i \in \{1, 2\}$, $j \in \{1, \ldots, K\}$, $l \in \{0, 1, 2\}$, and $x = [x^1, x^2]^T$.

In (7.1),

- $\mathcal{D}^{\mathrm{LM}}$ denotes the sum of squared landmark distances

$$\mathcal{D}^{\mathrm{LM}}[f] = \sum_{j=1}^{K} \|f(t_j) - r_j\|^2, \tag{7.3}$$

- $\mathcal{C}$ denotes the contour matching term

$$\mathcal{C}[f] = \sum_{j=1}^{L} \frac{1}{2} \left[1 - \left(v \left[f \left(\overset{*}{t}_j \right) \right] \cdot v \left[\overset{*}{r}_j \right] \right)^2 \right], \tag{7.4}$$

  and

- $v \left[f \left(\overset{*}{t}_j \right) \right] \cdot v \left[\overset{*}{r}_j \right]$ denotes the cosine of the angle between corresponding unit vectors $v \left[f \left(\overset{*}{t}_j \right) \right]$ and $v \left[\overset{*}{r}_j \right]$ formed by consecutive contour-approximating points in the transformed template and reference images, respectively.

The components of the contour matching term are given by

- the unit secant vectors formed by connecting pairs of consecutive contour-approximating reference landmarks $\overset{*}{r}_j$ and $\overset{*}{r}_{(j+1)\bmod L}$

$$v \left[\overset{*}{r}_j \right] = \frac{\overrightarrow{\overset{*}{r}_j \overset{*}{r}_{j+1}}}{\left\| \overrightarrow{\overset{*}{r}_j \overset{*}{r}_{j+1}} \right\|} = \frac{\left\langle \overset{*1}{r}_{j+1} - \overset{*1}{r}_j, \overset{*2}{r}_{j+1} - \overset{*2}{r}_j \right\rangle}{\left\| \left\langle \overset{*1}{r}_{j+1} - \overset{*1}{r}_j, \overset{*2}{r}_{j+1} - \overset{*2}{r}_j \right\rangle \right\|} \tag{7.5}$$

  and

- the unit secant vectors formed by connecting pairs of consecutive contour-approximating landmarks $f\left(\overset{*}{t}_j\right)$ and $f\left(\overset{*}{t}_{(j+1)\bmod L}\right)$ defined on the transformed template

$$
\begin{aligned}
v\left[f\left(\overset{*}{t}_j\right)\right] &= \frac{\overrightarrow{f\left(\overset{*}{t}_j\right)f\left(\overset{*}{t}_{j+1}\right)}}{\left\|\overrightarrow{f\left(\overset{*}{t}_j\right)f\left(\overset{*}{t}_{j+1}\right)}\right\|} \\[2mm]
&= \frac{\left\langle f^1\left(\overset{*}{t}_{j+1}\right)-f^1\left(\overset{*}{t}_j\right), f^2\left(\overset{*}{t}_{j+1}\right)-f^2\left(\overset{*}{t}_j\right)\right\rangle}{\left\|\left\langle f^1\left(\overset{*}{t}_{j+1}\right)-f^1\left(\overset{*}{t}_j\right), f^2\left(\overset{*}{t}_{j+1}\right)-f^2\left(\overset{*}{t}_j\right)\right\rangle\right\|}
\end{aligned}
\tag{7.6}
$$

for $j = 0, \ldots, L-1$.

Minimizing the contour-matching term $\mathcal{C}$ is equivalent to maximizing the dot product of corresponding vectors that approximate the edges in the pair of images being registered or maximizing the similarity in the orientation of these unit vectors without any constraints on scaling. Therefore, the registration problem in (7.1) relaxes the TPS interpolation condition

$$
\mathcal{D}^{\mathrm{LM}}[f] = 0
\tag{7.7}
$$

and balances the overlap of the exact landmarks and the similarity between the orientation of the image contours.

An example of the setup required in the proposed Landmark and Contour-Matching (LCM) model is shown in Figure 7.2.

7.2 Experiments

7.2.1 2D LCM Registration

Hand Xrays from [4, 107] were used to validate the proposed Landmark and Contour Matching model.

Major reference-template landmark and contour-approximating point pairings were defined prior to registration. In our experiments, the major landmarks (i.e., the fingertips

(a) Reference $\mathcal{R}$ **(b)** Exact $\mathcal{R}$ LMs $\{r_j\}_{j=1}^{K}$ **(c)** Approx. $\mathcal{R}$ LMs $\left\{\overset{*}{r}_j\right\}_{j=1}^{L}$

(d) Template $\mathcal{T}$ **(e)** Exact $\mathcal{T}$ LMs $\{t_j\}_{j=1}^{K}$ **(f)** Approx. $\mathcal{T}$ LMs $\left\{\overset{*}{t}_j\right\}_{j=1}^{L}$
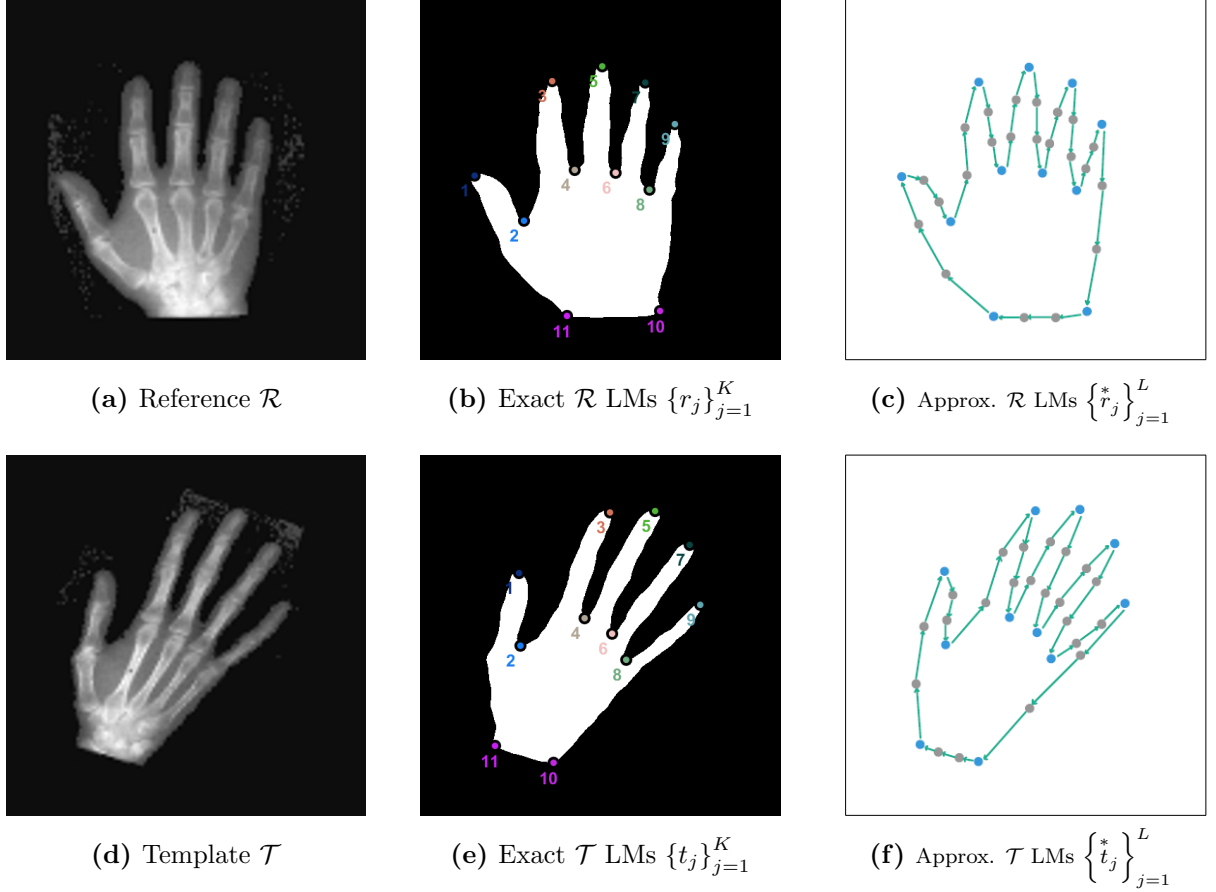
Figure 7.2: Landmark and Contour-Matching (LCM) Model requisites. (a) Reference image, (b) exact/major reference landmarks, (c) exact reference landmarks, contour-approximating points and vectors, (d) template image, (e) exact template landmarks, (f) exact template landmarks, contour-approximating points and vectors. Here, the number of exact landmarks is $K = 11$ and the number of contour-approximating points is $L = 33$.

and the cusps in between adjacent fingers) were identified via the interest point detection method presented in Chapter 6. Meanwhile, the contour-approximating points

$$\left\{\overset{*}{r}_j\right\}_{j=1}^{L} \text{ and } \left\{\overset{*}{t}_j\right\}_{j=1}^{L}$$

represent an ordered sampling of the connected set of pixels that trace the edges of the hands. We note here that the major landmarks could be selected manually or through a different interest point detection method. Thus, the set of major landmarks need not be a proper subset of the collection of contour-approximating landmarks.

We then solved the constrained optimization problem in (7.1) using Newton's method to obtain the optimal TPS parameters. At every iteration, the distances between the transformed major template landmarks and their target locations were calculated. In addition, the vectors connecting adjacent contour-approximating landmarks were normalized, and the cosine of the interior angles formed by corresponding unit vector pairs in the reference and transformed template were calculated to measure the overall similarity between the orientation of the contours present in the two images.

The exact Hessian of both the landmark and contour-matching terms in (7.1) were used in the implementation of the Newton method. The derivations for the Jacobian and Hessian of each component of the LCM model are provided in Appendices C-D.

In the first set of experiments, we simply performed the steps described above and compared the results of the proposed model against registered images obtained by blindly performing TPS registration (i.e., by solving (7.1) where $\alpha = 0$) with

1a. only 11 POIs as exact landmarks (Figure 7.3a)

1b. the 11 POIs in Experiment 1a and a specified number of additional contour-approximating landmarks, all of which were treated as major landmarks (Figure 7.3b).

The goal of this set of experiments is to determine whether the proposed LCM model indeed addresses the drawbacks of TPS registration. First, we want to observe whether

using the same major landmarks as in Experiment 1a and adding extra contour information from the approximate landmarks as hard constraints lessens the occurrence of unnatural bending and consequently improves the image overlap away from the exact landmarks.

Next, we wish to gauge whether LCM-registered results using few exact landmarks as hard constraints and supplying additional approximate contour information (only to be used in the second term $C[f]$) improves on the results of Experiment 1b, where contour-approximating landmarks are treated as hard interpolation conditions.

The second and third sets of experiments (Experiments 2a and 2b shown in Figures 7.4a-7.4b, and Experiments 3a and 3b shown in Figures 7.5a-7.5b) are the same as the first, except that landmark localization errors were introduced to the major template landmarks – 1 LM with error for Experiment 2, and 2 LMs with errors for Experiment 3. The purpose of these experiments is to determine the accuracy of the registration methods in the presence of landmark localization error. The TRE and Dice coefficients of the registered images resulting from the application of TPS are compared against those of the LCM-registered images.

7.2.2 3D Analogue of LCM Registration for Cardiac Volumes

The proposed model was also modified to accommodate the registration of the same set of 3D cardiac images used in Chapters 3, 5, and 6.

Surface-approximating landmarks were detected prior to LCM registration as discussed in Chapter 6. Connecting adjacent landmarks then results to the formation of approximate myocardial contours that resemble the latitude and longitude of the Earth's lower hemisphere (Figure 7.7a). This also implies that each approximate landmark can be associated with two vectors: one parallel to the short axis of the heart (v_{Hor}), and the other extending from the approximate landmark to its corresponding point in the next sampling slice (v_{Vert}). Thus, given L surface-approximating landmarks, the 3D analogue

of the contour matching term $\mathcal{C}$ of the proposed LCM model (7.1) specifically for our cardiac dataset is

$$
\begin{aligned}
\mathcal{C}[f] \;=\; & \sum_{j=1}^{L} \frac{1}{2} \left[1 - \left(v_{\text{Hor}} \left[f\left(\overset{*}{t}_j\right) \right] \cdot v_{\text{Hor}} \left[\overset{*}{r}_j\right] \right)^2 \right] \\
& + \frac{1}{2} \left[1 - \left(v_{\text{Vert}} \left[f\left(\overset{*}{t}_j\right) \right] \cdot v_{\text{Vert}} \left[\overset{*}{r}_j\right] \right)^2 \right].
\end{aligned}
\tag{7.8}
$$

Aside from calculating the improvement of image overlap in terms of Dice coefficients, we will also measure the average target registration errors from three repeatable cardiac landmarks, namely the left ventricular apex A_{LV}, and the two right ventriculo-septal junctions P_1 and P_2 (see Figures 7.7b-7.7c). Similar to the 2D experiments, we will comment on the quality of the LCM-registered images and compare them against TPS-registered images.

7.3   Results

7.3.1   2D LCM Registration

The results of the first set of experiments are displayed in Figure 7.3a. Observe that imposing only a few hard constraints in the TPS approach yielded registered images where the fingers are slightly bent. $K = 11$ exact landmarks were used in Experiment 1a.

Next, for Experiment 1b (Figure 7.3b), 55 contour-approximating landmarks were used as exact landmarks (i.e., as hard constraints) in the TPS interpolation problem in order to determine whether an increase in the number of exact landmark correspondences also results to an improvement in the registration accuracy. While the Dice similarity coefficient did increase, the registered image still exhibits some irregularities. Notice that the metacarpophalangeal joints of the middle and ring fingers were distorted by the registration transformation.

In contrast, the LCM-registered template yielded both an improved Dice similarity coefficient compared to Experiment 1a, in addition to a more visually accurate transformed template (Figure 7.3c). More specifically, there were no apparent deformities such as bent fingers and distorted bones in the LCM results unlike those yielded by Experiments 1a and 1b.

When analyzing the results of Experiments 2 and 3 (with one and two landmark localization errors, respectively), it is important to note that TPS registration at its core is just an interpolation technique. Therefore, blindly applying the technique naturally results to misregistrations (Figures 7.4a-7.4b and 7.5a-7.5b) – regardless of the number of interpolating points.

A more comprehensive tabulation of the results of Experiment 2 is also provided in Figure 7.6. Each row in said figures corresponds to a set of experiments where a localization error was introduced to one of the 11 of the major landmarks. Displayed in the second-fourth columns are TPS registration results with different numbers of interpolating conditions, while the last column shows LCM-registered images for each experiment.

The TREs associated with different configurations for Experiment 2 (e.g., registration method used, location of major landmark error, number of contour-approximating points used, etc.) can be found in Table 7.1. The corresponding implementation runtimes are provided in Appendix B. Observe that while increasing the number of exact landmark matching conditions for TPS sometimes leads to smaller TREs, doing so does not necessarily guarantee a visually accurate transformed template as demonstrated in Column 4 of Figure 7.6.

The results of the proposed LCM method in Figures 7.4-7.5 once again outperformed those of the TPS approach and resulted to better post-registration Dice image similarities, lower target registration errors (TRE), and registered images without abnormalities even in the presence of a landmark error (Figures 7.4c and 7.5c).

(a) Experiment 1a: TPS using major LMs only ($K = 11$); Post-TPS registration Dice=0.82
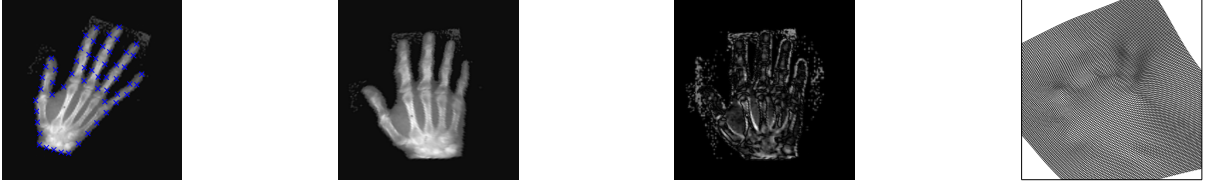
(b) Experiment 1b: TPS using major and contour-approximating LMs as exact LMs ($K = 55$); Post-TPS Registration Dice=0.85
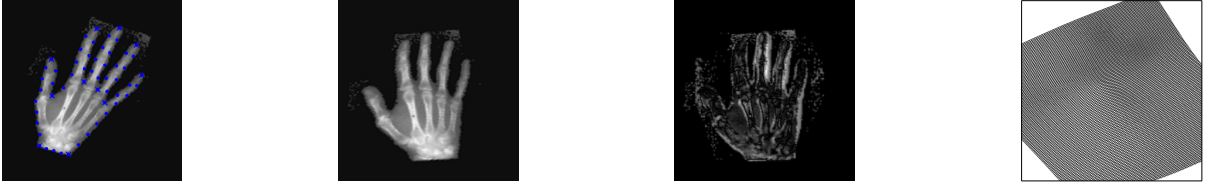
(c) Proposed Method: LCM model using $K = 11$ Major ($*$) and $L = 55$ Contour-approximating ($\cdot$) LMs, $\alpha = 1 \times 10^4$; Post-LCM Registration Dice=0.83

Figure 7.3: Experiment 1. Comparison of TPS and LCM Registration Accuracy when no errors are present in the landmark data. (a) Results of Experiments 1a, (b) results of Experiment 1b. (c) LCM registration results. Pre-Registration Dice=0.64. (First col) Reference image with exact and contour-approximating landmarks, (Second col) registered image, (Third col) post-registration subtraction image $|R - T[f]|$, (Fourth col) optimal transformation. Bending, ridges along the finger contours, and bone deformities are present in the TPS-registered images in (a) and (b). Notably, the LCM-registered image in (c) does not suffer from such deformities.

(a) Experiment 2a: TPS using major LMs only ($K = 11$). Post-TPS registration Dice=0.81; TRE=9.27mm
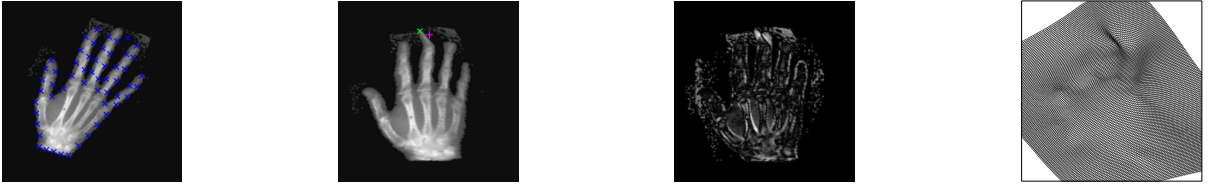
(b) Experiment 2b: TPS using major and contour-approximating LMs as exact LMs ($K = 55$). Post-TPS registration Dice=0.84; TRE=7.13mm

(c) Proposed Method: LCM model using $K = 11$ Major ($*$) and $L = 54$ Contour-approximating ($\cdot$) LMs. Post-LCM registration Dice=0.81; TRE=5.19mm

Figure 7.4: Experiment 2: Comparison of TPS and LCM registration accuracy for the case where a localization error was introduced to t_5 (the middle fingertip). (a) Results of Experiment 2a, (b) results of Experiment 2b, (c) exemplary LCM registration results. Pre-Registration Dice=0.64. (1st col) Reference image with exact and contour-approximating landmarks, (2nd col) registered image, (3rd col) post-registration subtraction image $|R - T[f]|$, (4th col) optimal transformation.
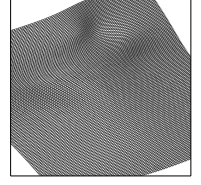
(a) Experiment 3a: TPS using major LMs only ($K = 11$). Post-TPS registration Dice=0.77; TRE=10.71mm
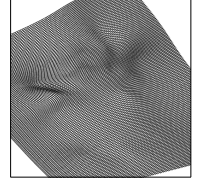
(b) Experiment 3b: TPS using major and contour-approximating LMs as exact LMs ($K = 55$). Post-TPS registration Dice=0.84; TRE=5.66mm
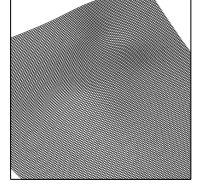
(c) Proposed Method: LCM model using $K = 11$ Major ($*$) and $L = 53$ Contour-approximating ($\cdot$) LMs. Post-LCM registration Dice=0.80; TRE=5.09mm

Figure 7.5: Experiment 3: Comparison of TPS and LCM Registration Accuracy for the case where errors were added to t_1 and t_5. (a) Exemplary results of Experiment 3a, (b) exemplary results of Experiment 3b, (c) LCM registration results. Pre-Registration Dice=0.64. (1st col) Reference image with exact and contour-approximating landmarks, (2nd col) registered image, (3rd col) post-registration subtraction image $|R - T[f]|$, (4th col) optimal transformation.

(a) Experiment with Incorrect t_1

(b) Experiment with Incorrect t_2

(c) Experiment with Incorrect t_3
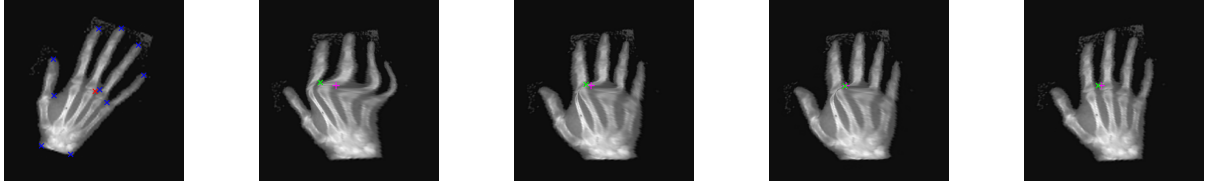
(d) Experiment with Incorrect t_4

(e) Experiment with Incorrect t_6

Figure 7.6: Additional TPS vs LCM registration comparisons for Experiment 2, where a localization error was introduced to t_i, $i = 1, 2, 3, 4, 6$. (1st col) Template image with exact and contour-approximating landmarks, (2nd col) TPS-registered image with $K = 11$ exact landmarks, (3rd col) TPS-registered image with $K = 55$ exact landmarks, (4th col) TPS-registered image with $K = 278$ exact landmarks, (5th col) LCM-registered image with $\alpha = 1 \times 10^4$, $K = 11$, and $L = 54$. Direct application of hard TPS interpolation conditions resulted to misregistrations and distorted fingers as in Columns 2-4. LCM provides good image overlaps and mitigates the effect of the LM error.
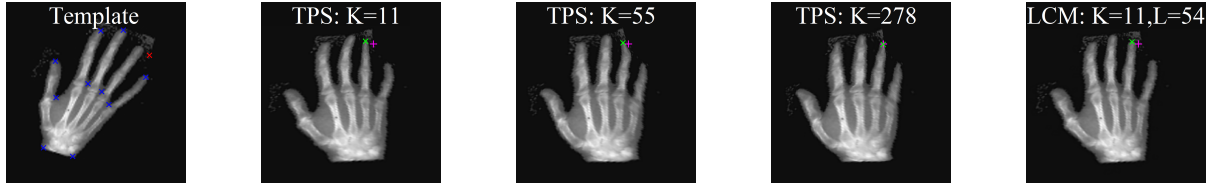
(f) Experiment with Incorrect t_7

(g) Experiment with Incorrect t_8

(h) Experiment with Incorrect t_9

(i) Experiment with Incorrect t_{10}
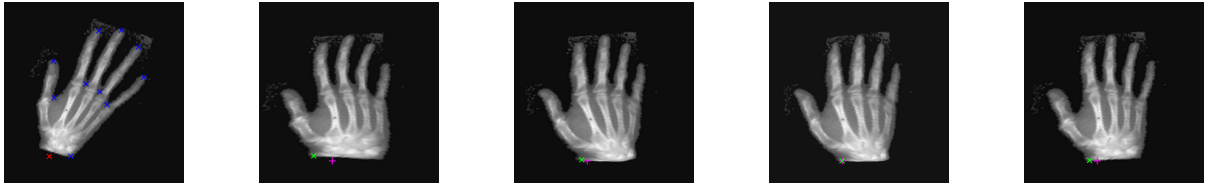
(j) Experiment with Incorrect t_{11}

Figure 7.6: (Cont'd) Additional TPS vs LCM registration comparisons for Experiment 2, where a localization error was introduced to t_i, $i = 7, \ldots, 11$. (1st col) Template image with exact and contour-approximating landmarks, (2nd col) TPS-registered image with $K = 11$ exact landmarks, (3rd col) TPS-registered image with $K = 55$ exact landmarks, (4th col) TPS-registered image with $K = 278$ exact landmarks, (5th col) LCM-registered image with $\alpha = 1 \times 10^4$, $K = 11$, and $L = 54$. Direct application of hard TPS interpolation conditions resulted to misregistrations and distorted fingers as in Columns 2-4. LCM provides good image overlaps and mitigates the effect of the LM error.

		Experiment 2 Target Registration Errors										
		Major Landmark with Error										
		t_1	t_2	t_3	t_4	t_5	t_6	t_7	t_8	t_9	t_{10}	t_{11}
L=0	TPS Expt2a: $K = 11, L = 0$	13.39	11.21	8.51	11.56	9.27	7.15	5.85	6.07	5.87	10.03	13.64
L=36	TPS Expt2b: $K = 37, L = 0$	8.33	5.11	9.77	6.58	9.51	3.94	4.94	3.12	3.31	4.65	5.52
	LCM ($K = 11, L = 37$)	4.14	6.81	1.74	4.17	6.46	1.55	5.46	3.40	2.81	8.70	8.12
L=54	TPS Expt2b: $K = 55, L = 0$	4.18	3.97	5.12	5.59	7.13	2.80	3.84	4.70	2.01	3.72	3.98
	LCM ($K = 11, L = 54$)	4.51	4.66	1.55	3.29	5.19	4.20	4.67	4.10	5.52	8.90	5.51
L=92	TPS Expt2b: $K = 93, L = 0$	0.80	1.56	2.68	3.76	2.72	3.81	1.72	4.29	0.97	2.23	2.12
	LCM ($K = 11, L = 92$)	2.95	3.67	0.25	2.04	3.66	1.65	4.33	2.61	3.91	8.99	3.07
L=184	TPS Expt2b: $K = 185, L = 0$	0.50	0.39	0.75	1.26	0.58	1.63	1.02	1.30	0.50	1.04	0.39
	LCM ($K = 11, L = 184$)	0.86	2.12	4.69	5.96	4.76	1.59	5.25	3.54	4.2	8.55	2.16
L=277	TPS Expt2b: $K = 278, L = 0$	0.16	0.27	0.35	0.70	0.22	0.60	0.35	0.97	0.43	0.55	0.15
	LCM ($K = 11, L = 277$)	3.58	8.88	5.35	2.18	5.39	3.02	5.70	5.38	5.10	8.94	4.26

Table 7.1: Target registrations resulting from experiments where a localization error was introduced to one of the 11 major LMs.

7.3.2 3D Analogue of LCM Registration for Cardiac Volumes

We now present the results of the modified version of the LCM model specifically designed for 3D cardiac registration.

Exemplary results of both TPS and LCM registration are shown in Figures 7.8c-7.8d and 7.9c-7.9d, along with cross sections of the template, registered templates, and their corresponding difference images with respect to the reference image. TPS-registered images exhibit deformities similar to what we have observed in the 2D hands experiments. Such deformities are more noticeable when viewing short-axis slices of the TPS-registered images, whose edges exhibit ridges even when the original template edges are smooth (Figures 7.8f and 7.9f). In contrast, the registered images obtained through LCM registration (Figures 7.8g and 7.9g) are free from such deformities and instead possess smoother edges.

Target registration errors before and after performing LCM registration are displayed in Tables 7.2 and 7.3, respectively, to measure the accuracy of the 3D LCM model with

the proposed setup. The average pre-registration TRE decreased from 27.2952mm to 0.0053mm after LCM registration. The maximum post-LCM TRE across all possible reference-template pairings is 0.0977mm. We also report a 129%-average improvement in Dice similarity coefficients after implementing the proposed method.

(a) Heart w/ Surface Vectors   **(b)** 3D LCM Setup - Heart 1   **(c)** 3D LCM Setup - Heart 2
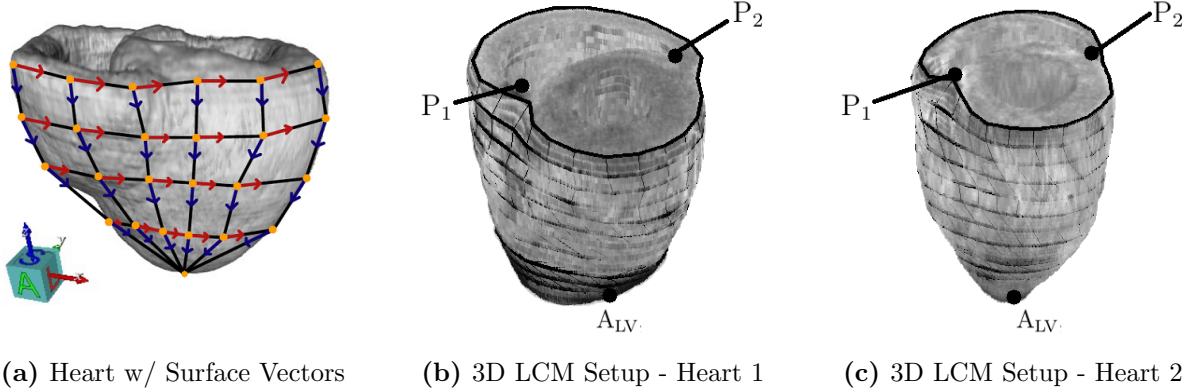
Figure 7.7: Landmark and Surface-Matching (LCM) Model requisites. (a) Details of the required setup for 3D LCM registration: Heart with longitudinal and latitudinal vectors at each surface point, (b)-(c) actual LCM setup for 2 hearts in the dataset with latitudinal and longitudinal segments connecting adjacent surface points with the repeatable landmarks P_1, P_2, and A_{LV}.

7.4 Conclusions and Future Work

We proposed a new registration model that uses contour-approximating landmarks to supplement missing edge information in between defined landmarks. We demonstrated that the model was able to circumvent drawbacks associated with the straightforward application of the TPS registration technique.

The LCM model was shown to increase the post-registration Dice similarity between the reference and registered template by improving the image overlap away from major landmarks. Consequently, this reduced the appearance of the unnatural bending in image regions bordered by the data interpolation points (major landmark locations).

(a) Reference $\mathcal{R}$ **(b)** Template $\mathcal{T}$ **(c)** $\mathcal{T}[f_{\mathrm{TPS}}]$ **(d)** $\mathcal{T}[f_{\mathrm{LCM}}]$

(e) Cross sections of template $\mathcal{T}$ and pre-registration difference images $|\mathcal{R} - \mathcal{T}|$

(f) Cross sections of TPS-registered template $\mathcal{T}[f_{\mathrm{TPS}}]$ and post-TPS registration images $|\mathcal{R} - \mathcal{T}[f_{\mathrm{TPS}}]|$

(g) Cross sections of LCM-registered template $\mathcal{T}[f_{\mathrm{LCM}}]$ and post-LCM registration images $|\mathcal{R} - \mathcal{T}[f_{\mathrm{LCM}}]|$
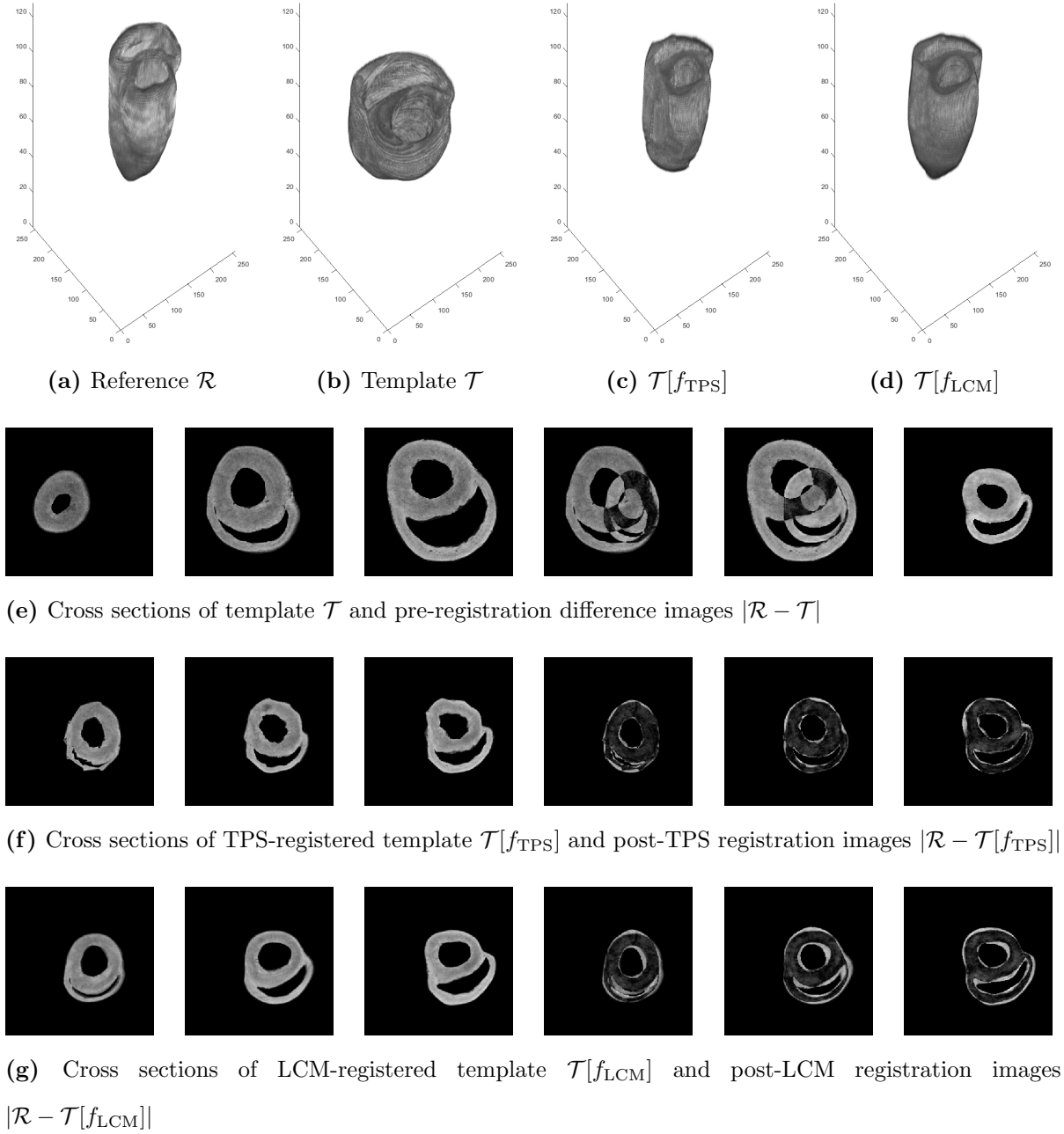
Figure 7.8: Exemplary results obtained from 3D LCM registration of cardiac volumes. (a)-(d) 3D view of the reference, template, TPS-registered image, and LCM-registered image, (e) short-axis slices of the template and pre-registration difference images, (f) short-axis slices of the TPS-transformed template and difference images with respect to the reference, (g) short-axis slices of the LCM-transformed template and difference images with respect to the reference.

(a) Reference $\mathcal{R}$ **(b)** Template $\mathcal{T}$ **(c)** $\mathcal{T}[f_{\mathrm{TPS}}]$ **(d)** $\mathcal{T}[f_{\mathrm{LCM}}]$

(e) Cross sections of template $\mathcal{T}$ and pre-registration difference images $|\mathcal{R} - \mathcal{T}|$

(f) Cross sections of TPS-registered template $\mathcal{T}[f_{\mathrm{TPS}}]$ and post-TPS registration images $|\mathcal{R} - \mathcal{T}[f_{\mathrm{TPS}}]|$

(g) Cross sections of LCM-registered template $\mathcal{T}[f_{\mathrm{LCM}}]$ and post-LCM registration images $|\mathcal{R} - \mathcal{T}[f_{\mathrm{LCM}}]|$
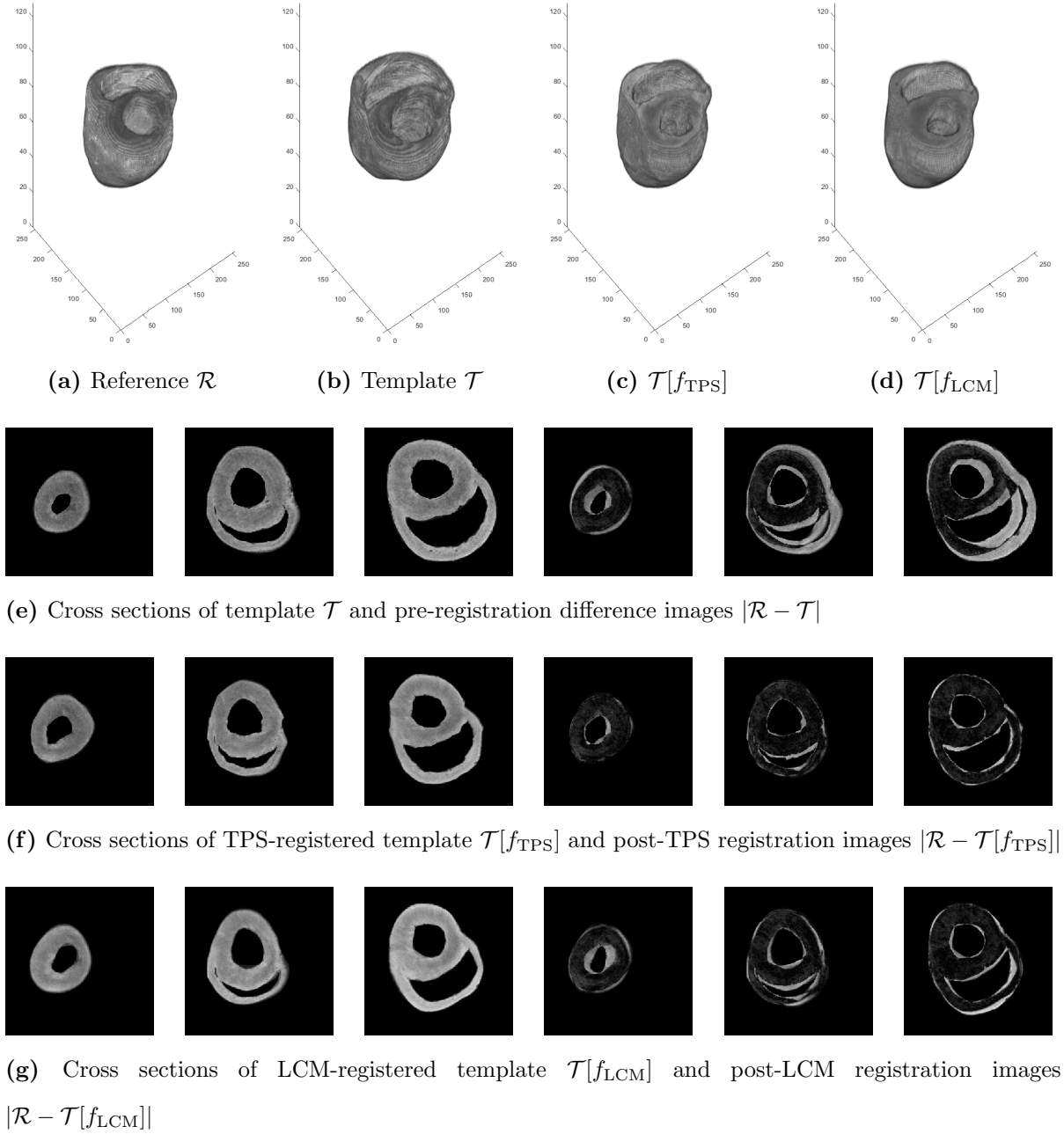
Figure 7.9: Exemplary results obtained from 3D LCM registration of cardiac volumes. (a)-(d) 3D view of the reference, template, TPS-registered image, and LCM-registered image, (e) short-axis slices of the template and pre-registration difference images, (f) short-axis slices of the TPS-transformed template and difference images with respect to the reference, (g) short-axis slices of the LCM-transformed template and difference images with respect to the reference.

		Target Registration Error Pre-LCM Registration							
		Template Heart							
		Heart1	Heart2	Heart3	Heart4	Heart5	Heart6	Heart7	Heart8
Reference Heart	Heart1	0	21.7859	19.5421	40.1476	23.7721	23.6332	30.2411	17.2793
	Heart2	21.7859	0	12.2054	48.3597	28.8880	40.2077	47.5277	22.0665
	Heart3	19.5421	12.2054	0	44.9596	20.7178	35.1230	41.8842	20.0262
	Heart4	40.1476	48.3597	44.9596	0	40.2792	40.5403	40.7324	54.0938
	Heart5	23.7721	28.8880	20.7178	40.2792	0	27.0913	33.4896	21.1585
	Heart6	23.6332	40.2077	35.1230	40.5403	27.0913	0	10.2923	29.4274
	Heart7	30.2411	47.5277	41.8842	40.7324	33.4896	10.2923	0	37.9757
	Heart8	17.2793	22.0665	20.0262	54.0938	21.1585	29.4274	37.9757	0

Table 7.2: Target registration errors before performing 3D cardiac LCM registration. TREs are expressed in terms of the voxel locations of the repeatable landmarks.

		Target Registration Error Post-LCM Registration							
		Template Heart							
		Heart1	Heart2	Heart3	Heart4	Heart5	Heart6	Heart7	Heart8
Reference Heart	Heart1	0	0.0005	0.0012	0.0006	0.0019	0.0007	0.0006	0.0023
	Heart2	0.0977	0	0.0110	0.0606	0.0078	0.0027	0.0009	0.0014
	Heart3	0.0155	0.0241	0	0.0290	0.0005	0.0019	0.0009	0.0091
	Heart4	0.0012	0.0016	0.0025	0	0.0022	0.0032	0.0020	0.0026
	Heart5	0.0030	0.0013	0.0025	0.0013	0	0.0031	0.0014	0.0016
	Heart6	0.0018	0.0013	0.0029	0.0017	0.0020	0	0.0015	0.0029
	Heart7	0.0016	0.0015	0.0019	0.0014	0.0016	0.0019	0	0.0027
	Heart8	0.0047	0.0018	0.0023	0.0005	0.0017	0.0022	0.0014	0

Table 7.3: Target registration errors after performing 3D cardiac LCM registration. TREs are expressed in terms of the voxel locations of the repeatable landmarks.

We also showed that naively increasing the number of interpolation conditions does not always guarantee a clinically accurate registration result. Doing so resulted to an ill-conditioned problem, made the TPS technique computationally more expensive, and also caused visual deformities in the transformed template. As with addressing the first TPS issue, we showed that solving the LCM registration problem with less exact landmarks and additional approximate contour information provided accurate results.

The LCM model also produced physically accurate registration results with improved Dice similarity indices even when landmark localization errors were present in the data.

Additionally, a technique for approximate surface-matching of 3D cardiac images was proposed. The cardiac interest point and surface-approximating method proposed in the previous chapter, together with a 3D extension of the 2D LCM model, provides a complete framework for cardiac image registration that reduces the need to manually delineate anatomical landmarks and supply a dense collection of reference-template point clouds to facilitate accurate pairwise registration.

Overall, the LCM model increases the flexibility of the TPS approach especially when only a few repeatable landmarks can be defined, when defining too many landmarks leads to high oscillations in the registration transformations, or when the identification of exact landmarks is susceptible to human error.

We remark that our methods are currently limited to high-contrast medical images that can be easily segmented through intensity thresholding. In the future, we would like to extend the applicability of the LCM model to other datasets. We also plan to come up with more efficient ways to approximate surfaces in order to perform the proposed landmark- and contour-based registration on other 3D images.

Chapter 8

Summary and Concluding Remarks

This thesis highlights the central role that image registration plays in biomedical research – from producing clinically relevant image-based predictive models, to enabling accurate patient diagnosis and treatment response.

A concise overview of the various computational components necessary in solving a registration problem was provided in Chapter 2. The distance measures commonly used in intensity-based and landmark-based methods were discussed. The issues surrounding both approaches drove the development of various registration algorithms in this thesis.

In Chapter 3, we explored the use of a classical framework for atlas-building to obtain an average geometry for a dataset of diffusion-weighted MR images. While this was a relatively straightforward use of an existing intensity-based registration framework on a new dataset, the cardiac fiber atlas that we constructed from explanted healthy porcine hearts could advance our understanding of the correlation between fiber structural organization and its electrophysiology. Ultimately, this could translate to a better understanding of our own cardiac functions.

In Chapter 4, we took on the challenge of aligning multi-temporal images to eliminate motion in DCE-MR sequences. Our main contribution here is the development of two novel registration methods for images with locally varying intensities. First is the coupling of the Normalized Gradient Field distance measure with the same groupwise approach presented in Chapter 3. The role of groupwise registration, however, is different this time. While we still obtained an average geometry, what we ultimately needed was a motionless sequence of images. In the groupwise scheme, this motionless sequence was given by the final set of registered images aligning each frame to the average geometry. The second motion correction approach that we proposed involved the use of both structural and

temporal information (refined through a pharmacokinetic model) to simplify the image alignment process. Both methods were effective in eliminating motion and performed better than existing motion correction methods in terms of both local and global measures of accuracy.

A means of comparing registration results from significantly different methods (e.g., pairwise vs. groupwise) with significantly different reference images was also provided in Chapter 4. We identified a common reference frame through the composition of the appropriate transformations.

The nature of the medical applications of the inter- and intra-subject registration problems discussed in Chapters 3 and 4 demanded good post-registration image overlaps across the entire image domain. For this reason, we decided to use intensity-based methods, consequently prioritizing accuracy over computational efficiency. However, the slow convergence of intensity-based registration algorithms left much to be desired.

We then started devising novel ways to speed up the alignment process. Landmark information was incorporated in Chapter 5 to the cardiac registration problem discussed in Chapter 3 in order to eliminate the need for a pre-registration step. Also, the solution space was restricted to that of thin plate spline transformations, essentially converting the problem to a parametric registration problem. This led to an increase in image similarity and it also increased the flexibility of Thin Plate Spline interpolation in catering to data with landmark localization errors.

Chapter 6 signified a transition from a hybrid landmark- and intensity-based approach to a purely landmark-based one. We made this possible by formulating a fast and complete registration pipeline that only requires minimal user input. Its first intended use was for cardiac registration. As such, it involved the automatic segmentation and classification of myocardial segments based on ventricular shape priors. Subsequently, a technique to automatically detect interest points and assign contour point correspondences was presented. This allowed the use of a point-based registration method, which

produced accurate registration results that were comparable to those obtained from multilevel elastic registration. The entire pipeline was shown to be significantly faster than the benchmark method. The applicability of the interest point detection method to other medical images was also demonstrated in this chapter.

In Chapter 7, data generated from the interest point detection method was used in the setup of a novel landmark- and contour-matching model. This model was designed to increase the flexibility of traditional landmark-based methods in handling data with landmark localization errors, provide accurate registration results comparable to those of intensity-based methods, and reduce computational runtime. We validated the LCM model on 2D medical images and also discussed how to extend it to accommodate 3D cardiac images.

Additionally, we provided all the implementation details of the novel registration methods that were proposed in Chapters 5 through 7. For Chapters 5 and 7, this entailed the mathematical theory as well as the derivation of all the computational components necessary to find a descent direction such as the Jacobian and exact Hessian of each term in the Hybrid model (Eq. 5.1) and the LCM model (Eq. 7.1). For Chapter 6, this included the physical interpretation (Figures 6.1, 6.3, and 6.4) of the mathematical tools (Equations 6.1-6.3) used in the fast registration pipeline.

Lastly, the current reality is that there is not a lot of publicly available medical data for testing. This makes the use existing state-of-the-art registration methods using convolutional neural networks (CNN) impractical. Perhaps the most significant contribution of this research is the provision of classical yet still effective techniques to address some existing problems in medical image analysis – even for small datasets.

Appendices

Appendix A

Software

Following are the different software that we employed in our work.

A.1   Image Registration and Landmark Detection

Due to its flexibility and wide array of resources for image registration, Jan Modersitzki's Flexible Algorithms for Image Registration (FAIR) [107] toolkit specifically built for MATLAB[1] was used to solve the registration problems in Chapters 3 and 4 (i.e., for the pairwise alignment of cardiac MR volumes and abdominal DCE-MR images).

Groupwise registration, tensor reorientation through Finite Strain as described in Chapter 3, as well as our own landmark detection and image registration codes for Chapters 5-7 were also implemented on MATLAB for simplicity.

A.2   Tensor Visualization

The transformed diffusion tensor fields and the associated average cardiac fiber tractography were visualized using MedInria [165]. Properties of the fiber atlas that were used for cross-validation, such as the mean fractional anisotropy and fiber lengths, were extracted through MedInria and DTI Studio [71].

A.3   Image Segmentation

Cardiac segmentation was performed in ITK-SNAP [181] as a pre-processing step for the hybrid registration problem in Chapter 5 and the interest point detection method in

---

[1]®2018 The MathWorks, Inc. MATLAB and Simulink are registered trademarks of The MathWorks, Inc. See `mathworks.com/trademarks` for a list of additional trademarks.

Chapter 6.

A.4 Image Visualization

Other image visualization software were also used at different stages of our work. These include the Statistical Parametric Mapping Software [128] and RadiAnt DICOM Viewer [102].

Appendix B

Runtimes

Listed herein are the computational runtimes (in seconds), sorted according to the type of medical data used in different processes involved in this thesis. The following process were implemented in MATLAB on a machine running on Intel(R) Core(TM) i5-8250U CPU @ 1.80GHz with 16GB of RAM. All tensors were reoriented and averaged using a workstation with Intel(R) Xeon(R) CPU E5-1620 v2 @ 3.70GHz and 16GB of RAM.

B.1 Cardiac MR Images

The porcine cardiac magnetic resonance volumes used in our experiments were provided by Dr. Mihaela Pop of Sunnybrook Research Institute. Each heart has resolution Image resolution was 0.5mm $\times$ 0.5mm $\times$ 1.6mm. The 3D volumes and 2D short-axis images from said volumes were used in the experiments listed in Table B.1 along with their corresponding computational runtimes.

B.2 Abdominal DCE-MR Images

Indicated in Table B.2 are the runtimes of the experiments discussed in Chapter 4 that focused on correcting motion in a sequence of 80 abdominal dynamic contrast-enhanced images (each of matrix size 128 $\times$ 128). This image sequence was provided by Dr. Anne Martel of Sunnybrook and was also used in [83].

3D Anatomical Cardiac Data for Atlas Construction	
Pairwise elastic registration	507.24
Computation of a mean reference image	0.02
5-Iteration groupwise registration	20289.40
3D Diffusion-Weighted Cardiac Data for Atlas Construction	
Diffusion tensor reorientation	21600
3D Anatomical Cardiac Data for Landmark-Based Registration	
TPS Registration	198.72
LCM Registration	153.51
2D Short-Axis Cardiac Data for Landmark Detection	
Myocardial segment classification	0.01
Interest point detection	0.09

2D Short-Axis Cardiac Data for Landmark-Based or Hybrid Registration						
	Number of Landmarks (for TPS) or Contour-Approximating Points (for LCM)					
	16	24	40	62	124	152
TPS Registration	11.88	18.78	25.42	37.24	50.53	57.73
LCM Registration	10.61	13.66	24.53	35.29	51.85	59.70

Table B.1: Runtimes (in seconds) of different experiments involving 3D cardiac MR data.

2D Abdominal Data	
SSDIC registration	336.95
5-Iteration groupwise SSDIC registration	620.73
NGF registration	253.72
5-Iteration groupwise NGF registration	834.57
Floating reference registration	446.86
Generating the synthetic motionless image sequence (for PK reg)	145.25
Pharmacokinetic registration	708.21

Table B.2: Runtimes (in seconds) of different experiments involving 2D abdominal DCE-MR data.

B.3 Hand Xrays

Compiled in Table B.3 are the runtimes of experiments using a pair of hand Xrays from [107]. These 2D images of size 128×128 were used in Chapters 6 and 7.

2D Hand Data						
		Number of Landmarks (for TPS) or Contour-Approximating Points (for LCM)				
		37	55	93	185	278
0 Error	TPS Registration	65.13	74.91	141.53	207.45	390.71
	LCM Registration	64.31	75.45	125.05	121.13	172.18
1 Error	TPS Registration	22.623	32.92	46.37	67.21	121.83
	LCM Registration	27.28	31.58	41.53	59.28	77.05
2 Errors	TPS Registration	45.72	62.87	108.23	198.47	397.44
	LCM Registration	67.58	74.24	86.25	144.62	194.06

Table B.3: Runtimes (in seconds) of different experiments involving 2D hand Xray data.

Appendix C

Hybrid Registration: Discretized Model and Derivatives

Mathematical Model for Combined Landmark- and Intensity-Based Registration with Thin Plate Spline Transformations:

$$\min_f \mathcal{J}[f] = \mathcal{D}^{\text{LM}}[f] + \alpha \mathcal{D}^{\text{INT}}[f] + \beta \mathcal{S}^{\text{TPS}}[f],$$

where

$$f^i(x) = \sum_{j=1}^{K} c_j^i \rho\left(\|x - t_j\|\right) + w_0^i + w_1^i x^1 + \ldots + w_d^i x^d, \ \ i = 1, \ldots, d,$$

and

$$\rho(t) = \begin{cases} t^2 \log t & \text{if } d = 2 \\ t & \text{if } d = 3 \end{cases}.$$

C.1   3D Hybrid Registration

Let $\mathcal{R}, \mathcal{T} : \Omega \subset \mathbb{R}^3 \to \mathbb{R}$ be the reference and template images defined on an $m \times n \times p$ grid X, and let $\{r_j\}_{j=1}^{K}$ and $\{t_j\}_{j=1}^{K}$ be K reference and template landmarks, respectively. Then the 3D hybrid registration problem is given by

$$\min_f \mathcal{J}[f] = \mathcal{D}^{\text{LM}}[f] + \alpha \mathcal{D}^{\text{INT}}[f] + \beta \mathcal{S}^{\text{TPS}}[f]$$

$$= \sum_{j=1}^{K} \sum_{i=1}^{3} \left[f^i(t_j) - r_j^i\right]^2 + h\alpha \sum_{j=1}^{mnp} \frac{1}{2} \left[\mathcal{T}[f(x_j)] - \mathcal{R}(x_j)\right]^2 + h\beta \sum_{j=1}^{mnp} \sum_{i=1}^{3} \left\langle \nabla^2 f^i(x_j), \nabla^2 f^i(x_j) \right\rangle,$$

where

- $\|\cdot\|$ denotes the Euclidean norm

- $f^i(x) = \sum\limits_{j=1}^{K} c_j^i \, \|x - t_j\| + w_0^i + w_1^i x^1 + w_2^i x^2 + w_3^i x^3,$

- $v = [v^1, v^2, v^3]^T \in \mathbb{R}^{3(K+4)}$ is the vector of transformation parameters, with components

- $v^i = [c_1^i, \ \ldots, \ c_K^i, \ w_0^i, \ w_1^i, \ w_2^i, \ w_3^i]^T \in \mathbb{R}^{k+4}$, for $i = 1, 2, 3$.

To find the optimal transformation, we need to compute the discrete derivative of the components of the above functional with respect to the parameters v of the transformation f at every gradient descent iteration.

C.1.1 Landmark Term $\mathcal{D}^{\mathbf{LM}}$

The Jacobian of

$$\mathcal{D}^{\mathrm{LM}}[f] = \sum_{j=1}^{K} \sum_{i=1}^{3} \left[f^i(t_j) - r_j^i \right]^2$$

with respect to the parameters of the thin plate spline transformation is

C.1.2 Intensity Term $\mathcal{D}^{\mathbf{INT}}$

The derivative of

$$\mathcal{D}^{\mathrm{INT}}[f] = h \sum_{j=1}^{mnp} \frac{1}{2} \left[\mathcal{T}[f(x_j)] - \mathcal{R}(x_j) \right]^2$$

with respect to the parameters of the thin plate spline transformation is

$$\mathbf{J}\mathcal{D}^{\mathrm{INT}}[f] = h \sum_{j=1}^{mnp} \left(\mathcal{T}[f(x_j)] - \mathcal{R}(x_j) \right) \left[\mathcal{T}_{x_j^1}[f(x_j)] \quad \mathcal{T}_{x_j^2}[f(x_j)] \quad \mathcal{T}_{x_j^3}[f(x_j)] \right] \cdot \frac{\partial f(x_j)}{\partial v},$$

where $\frac{\partial f(x_j)}{\partial v} \in \mathbb{R}^{3 \times 3(K+4)}$ and

$$\frac{\partial f(x_j)}{\partial v} = \begin{bmatrix} \frac{\partial f^1}{\partial c_1^1} & \frac{\partial f^2}{\partial c_1^1} & \frac{\partial f^3}{\partial c_1^1} \\[4pt] \frac{\partial f^1}{\partial c_2^1} & \frac{\partial f^2}{\partial c_2^1} & \frac{\partial f^3}{\partial c_2^1} \\[4pt] \vdots & \vdots & \vdots \\[4pt] \frac{\partial f^1}{\partial c_K^1} & \frac{\partial f^2}{\partial c_K^1} & \frac{\partial f^3}{\partial c_K^1} \\[4pt] \frac{\partial f^1}{\partial w_0^1} & \frac{\partial f^2}{\partial w_0^1} & \frac{\partial f^3}{\partial w_0^1} \\[4pt] \frac{\partial f^1}{\partial w_1^1} & \frac{\partial f^2}{\partial w_1^1} & \frac{\partial f^3}{\partial w_1^1} \\[4pt] \frac{\partial f^1}{\partial w_2^1} & \frac{\partial f^2}{\partial w_2^1} & \frac{\partial f^3}{\partial w_2^1} \\[4pt] \frac{\partial f^1}{\partial w_3^1} & \frac{\partial f^2}{\partial w_3^1} & \frac{\partial f^3}{\partial w_3^1} \\[4pt] \frac{\partial f^1}{\partial c_1^2} & \frac{\partial f^2}{\partial c_1^2} & \frac{\partial f^3}{\partial c_1^2} \\[4pt] \frac{\partial f^1}{\partial c_2^2} & \frac{\partial f^2}{\partial c_2^2} & \frac{\partial f^3}{\partial c_2^2} \\[4pt] \vdots & \vdots & \vdots \\[4pt] \frac{\partial f^1}{\partial c_K^2} & \frac{\partial f^2}{\partial c_K^2} & \frac{\partial f^3}{\partial c_K^2} \\[4pt] \frac{\partial f^1}{\partial w_0^2} & \frac{\partial f^2}{\partial w_0^2} & \frac{\partial f^3}{\partial w_0^2} \\[4pt] \frac{\partial f^1}{\partial w_1^2} & \frac{\partial f^2}{\partial w_1^2} & \frac{\partial f^3}{\partial w_1^2} \\[4pt] \frac{\partial f^1}{\partial w_2^2} & \frac{\partial f^2}{\partial w_2^2} & \frac{\partial f^3}{\partial w_2^2} \\[4pt] \frac{\partial f^1}{\partial w_3^2} & \frac{\partial f^2}{\partial w_3^2} & \frac{\partial f^3}{\partial w_3^2} \\[4pt] \frac{\partial f^1}{\partial c_1^3} & \frac{\partial f^2}{\partial c_1^3} & \frac{\partial f^3}{\partial c_1^3} \\[4pt] \frac{\partial f^1}{\partial c_2^3} & \frac{\partial f^2}{\partial c_2^3} & \frac{\partial f^3}{\partial c_2^3} \\[4pt] \vdots & \vdots & \vdots \\[4pt] \frac{\partial f^1}{\partial c_K^3} & \frac{\partial f^2}{\partial c_K^3} & \frac{\partial f^3}{\partial c_K^3} \\[4pt] \frac{\partial f^1}{\partial w_0^3} & \frac{\partial f^2}{\partial w_0^3} & \frac{\partial f^3}{\partial w_0^3} \\[4pt] \frac{\partial f^1}{\partial w_1^3} & \frac{\partial f^2}{\partial w_1^3} & \frac{\partial f^3}{\partial w_1^3} \\[4pt] \frac{\partial f^1}{\partial w_2^3} & \frac{\partial f^2}{\partial w_2^3} & \frac{\partial f^3}{\partial w_2^3} \\[4pt] \frac{\partial f^1}{\partial w_3^3} & \frac{\partial f^2}{\partial w_3^3} & \frac{\partial f^3}{\partial w_3^3} \end{bmatrix}^T = \begin{bmatrix} \|x_j - t_1\| & 0 & 0 \\[4pt] \|x_j - t_2\| & 0 & 0 \\[4pt] \vdots & \vdots & \vdots \\[4pt] \|x_j - t_K\| & 0 & 0 \\[4pt] 1 & 0 & 0 \\[4pt] x_j^1 & 0 & 0 \\[4pt] x_j^2 & 0 & 0 \\[4pt] x_j^3 & 0 & 0 \\[4pt] 0 & \|x_j - t_1\| & 0 \\[4pt] 0 & \|x_j - t_2\| & 0 \\[4pt] \vdots & \vdots & \vdots \\[4pt] 0 & \|x_j - t_K\| & 0 \\[4pt] 0 & 1 & 0 \\[4pt] 0 & x_j^1 & 0 \\[4pt] 0 & x_j^2 & 0 \\[4pt] 0 & x_j^3 & 0 \\[4pt] 0 & 0 & \|x_j - t_1\| \\[4pt] 0 & 0 & \|x_j - t_2\| \\[4pt] \vdots & \vdots & \vdots \\[4pt] 0 & 0 & \|x_j - t_K\| \\[4pt] 0 & 0 & 1 \\[4pt] 0 & 0 & x_j^1 \\[4pt] 0 & 0 & x_j^2 \\[4pt] 0 & 0 & x_j^3 \end{bmatrix}^T .$$

C.1.3 Smoothing Term $\mathcal{S}^{\mathbf{TPS}}$

The smoothing term $\mathcal{S}^{\mathrm{TPS}}$ is given by

$$\mathcal{S}^{\mathrm{TPS}}[f] = h \sum_{i=1}^{3} \mathcal{S}^{\mathrm{TPS}}[f^i]$$

$$= h \sum_{i=1}^{3} \sum_{j=1}^{mnp} \left\langle \nabla^2 f^i(x_j), \nabla^2 f^i(x_j) \right\rangle,$$

where

- $\nabla f^i(x) = \begin{bmatrix} \sum_{j=1}^{K} c_j^i \left[(x^1 - t_j^1)^2 + (x^2 - t_j^2)^2 + (x^3 - t_j^3)^2 \right]^{-1/2} \cdot \left(x^1 - t_j^1 \right) + 0 + w_1^i + 0 + 0 \\ \sum_{j=1}^{K} c_j^i \left[(x^1 - t_j^1)^2 + (x^2 - t_j^2)^2 + (x^3 - t_j^3)^2 \right]^{-1/2} \cdot \left(x^2 - t_j^2 \right) + 0 + 0 + w_2^i + 0 \\ \sum_{j=1}^{K} c_j^i \left[(x^1 - t_j^1)^2 + (x^2 - t_j^2)^2 + (x^3 - t_j^3)^2 \right]^{-1/2} \cdot \left(x^3 - t_j^3 \right) + 0 + 0 + 0 + w_3^i \end{bmatrix},$

- $\nabla^2 f^i(x) = \begin{bmatrix} \frac{\partial^2 f^i}{\partial [x^1]^2} & \frac{\partial^2 f^i}{\partial x^1 \partial x^2} & \frac{\partial^2 f^i}{\partial x^1 \partial x^3} \\ \frac{\partial^2 f^i}{\partial x^2 \partial x^1} & \frac{\partial^2 f^i}{\partial [x^2]^2} & \frac{\partial^2 f^i}{\partial x^2 \partial x^3} \\ \frac{\partial^2 f^i}{\partial x^3 \partial x^1} & \frac{\partial^2 f^i}{\partial x^3 \partial x^2} & \frac{\partial^2 f^i}{\partial [x^3]^2} \end{bmatrix}$, and

- $i \in \{1, 2, 3\}$.

For simplicity, denote $H^i(x) := \nabla^2 f^i(x)$. It is a symmetric matrix whose entries are

- $[H^i(x)]_{1,1} = \sum_{j=1}^{K} c_j^i \left(\frac{1}{\|x - t_j\|} - \frac{(x^1 - t_j^1)^2}{\|x - t_j\|^3} \right)$

- $[H^i(x)]_{2,2} = \sum_{j=1}^{K} c_j^i \left(\frac{1}{\|x - t_j\|} - \frac{(x^2 - t_j^2)^2}{\|x - t_j\|^3} \right)$

- $[H^i(x)]_{3,3} = \sum_{j=1}^{K} c_j^i \left(\frac{1}{\|x - t_j\|} - \frac{(x^3 - t_j^3)^2}{\|x - t_j\|^3} \right)$

- $[H^i(x)]_{1,2} = -\sum_{j=1}^{K} \frac{c_j^i (x^1 - t_j^1)(x^2 - t_j^2)}{\|x - t_j\|^3} = \left[H^i(x) \right]_{2,1}$

- $[H^i(x)]_{1,3} = -\sum_{j=1}^{K} \frac{c_j^i (x^1 - t_j^1)(x^3 - t_j^3)}{\|x - t_j\|^3} = \left[H^i(x) \right]_{3,1}$

- $[H^i(x)]_{2,3} = -\sum_{j=1}^{K} \dfrac{c_j^i(x^2 - t_j^2)(x^3 - t_j^3)}{\|x - t_j\|^3} = [H^i(x)]_{3,2}.$

Finally, we get

$$\mathcal{S}^{\mathrm{TPS}}[f^i(x)] = \left([H^i(x)]_{1,1}\right)^2 + \left([H^i(x)]_{2,2}\right)^2 + \left([H^i(x)]_{3,3}\right)^2$$
$$+ 2\left([H^i(x)]_{1,2}\right)^2 + 2\left([H^i(x)]_{1,3}\right)^2 + 2\left([H^i(x)]_{2,3}\right)^2.$$

Its derivative with respect to the parameters of the thin plate spline transformation

$$\mathbf{J}\mathcal{S}^{\mathrm{TPS}}[f^i] = \left[\begin{array}{ccccccccc} \dfrac{\partial f^i}{\partial c_1^1} & \dfrac{\partial f^i}{\partial c_2^1} & \cdots & \dfrac{\partial f^i}{\partial c_K^1} & \dfrac{\partial f^i}{\partial w_0^1} & \dfrac{\partial f^i}{\partial w_1^1} & \dfrac{\partial f^i}{\partial w_2^1} & \dfrac{\partial f^i}{\partial w_3^1} \\[2mm] \dfrac{\partial f^i}{\partial c_1^2} & \dfrac{\partial f^i}{\partial c_2^2} & \cdots & \dfrac{\partial f^i}{\partial c_K^2} & \dfrac{\partial f^i}{\partial w_0^2} & \dfrac{\partial f^i}{\partial w_1^2} & \dfrac{\partial f^i}{\partial w_2^2} & \dfrac{\partial f^i}{\partial w_3^2} \\[2mm] \dfrac{\partial f^i}{\partial c_1^3} & \dfrac{\partial f^i}{\partial c_2^3} & \cdots & \dfrac{\partial f^i}{\partial c_K^3} & \dfrac{\partial f^i}{\partial w_0^3} & \dfrac{\partial f^i}{\partial w_1^3} & \dfrac{\partial f^i}{\partial w_2^3} & \dfrac{\partial f^i}{\partial w_3^3} \end{array} \right],$$

where

- $\dfrac{\partial f^i}{\partial c_j^a} = \begin{cases} 2[H^i(x)]_{1,1}\left(\dfrac{1}{\|x-t_j\|} - \dfrac{(x^1-t_j^1)^2}{\|x-t_j\|^3}\right) \\[3mm] +2[H^i(x)]_{2,2}\left(\dfrac{1}{\|x-t_j\|} - \dfrac{(x^2-t_j^2)^2}{\|x-t_j\|^3}\right) \\[3mm] +2[H^i(x)]_{3,3}\left(\dfrac{1}{\|x-t_j\|} - \dfrac{(x^2-t_j^2)^2}{\|x-t_j\|^3}\right) & \text{if } i = a \\[3mm] -4[H^i(x)]_{1,2}\dfrac{(x_1-t_j^1)(x_2-t_j^2)}{\|x-t_j\|^3} \\[3mm] -4[H^i(x)]_{1,3}\dfrac{(x_1-t_j^1)(x_3-t_j^3)}{\|x-t_j\|^3} \\[3mm] -4[H^i(x)]_{2,3}\dfrac{(x_2-t_j^2)(x_3-t_j^3)}{\|x-t_j\|^3} \\[6mm] 0 & \text{otherwise} \end{cases}$

- $\dfrac{\partial f^i}{\partial w_j^i} = 0$ for $j = 0, 1, 2, 3, \ i = 1, 2, 3.$

C.2 2D Hybrid Registration

Let $\mathcal{R}, \mathcal{T} : \Omega \subset \mathbb{R}^2 \to \mathbb{R}$ be the reference and template images defined on an $m \times n$ grid X, and let $\{r_j\}_{j=1}^K$ and $\{t_j\}_{j=1}^K$ be K reference and template landmarks, respectively. Then the 2D hybrid registration problem is given by

$$
\min_f \mathcal{J}[f] = \mathcal{D}^{\mathrm{LM}}[f] + \alpha \mathcal{D}^{\mathrm{INT}}[f] + \beta \mathcal{S}^{\mathrm{TPS}}[f]
$$

$$
= \sum_{j=1}^K \sum_{i=1}^2 \left[f^i(t_j) - r_j^i \right]^2 + h\alpha \sum_{j=1}^{mn} \frac{1}{2} \left[\mathcal{T}[f(x_j)] - \mathcal{R}(x_j) \right]^2 + h\beta \sum_{j=1}^{mn} \sum_{i=1}^2 \left\langle \nabla^2 f^i(x_j), \nabla^2 f^i(x_j) \right\rangle,
$$

where

- $f^i(x) = \sum_{j=1}^K c_j^i \|x - t_j\|^2 \log(\|x - t_j\|) + w_0^i + w_1^i x^1 + w_2^i x^2,$

- $v = [v^1, v^2]^T \in \mathbb{R}^{2(K+3)}$ is the vector of transformation parameters, with components

- $v^i = [c_1^i, \ \ldots, \ c_K^i, \ w_0^i, \ w_1^i, \ w_2^i]^T \in \mathbb{R}^{K+3}$, for $i = 1, 2$.

Similar to the 3D problem, we need to compute the discrete derivative of the components of the above functional with respect to the parameters v of the transformation f at every gradient descent iteration.

C.2.1 Landmark Term $\mathcal{D}^{\mathrm{LM}}$

The Jacobian of

$$
\mathcal{D}^{\mathrm{LM}}[f] = \sum_{j=1}^K \sum_{i=1}^2 \left[f^i(t_j) - r_j^i \right]^2
$$

with respect to the parameters of the thin plate spline transformation is

$$
\mathbf{J}\mathcal{D}^{\mathrm{LM}}[f] = \sum_{j=1}^K \sum_{i=1}^2 2 \left[f^i(t_j) - r_j^i \right] \cdot \frac{\partial f^i(t_j)}{\partial v}. \tag{C.1}
$$

In Equation C.1,

$$\frac{\partial f^i(t_j)}{\partial v} = \left[\begin{array}{cccccc|ccccc} \frac{\partial f^i}{\partial c_1^1} & \cdots & \frac{\partial f^i}{\partial c_K^1} & \frac{\partial f^i}{\partial w_0^1} & \frac{\partial f^i}{\partial w_1^1} & \frac{\partial f^i}{\partial w_2^1} & \frac{\partial f^i}{\partial c_1^2} & \cdots & \frac{\partial f^i}{\partial c_K^2} & \frac{\partial f^i}{\partial w_0^2} & \frac{\partial f^i}{\partial w_1^2} & \frac{\partial f^i}{\partial w_2^2} \end{array} \right]$$

with

- $\dfrac{\partial f^i(t_j)}{\partial c_m^n} = \begin{cases} \|t_j - t_m\|^2 \log \|t_j - t_m\| & \text{if } i = n \\ 0 & \text{otherwise} \end{cases}$

- $\dfrac{\partial f^i(t_j)}{\partial w_0^n} = \begin{cases} 1 & \text{if } i = n \\ 0 & \text{otherwise} \end{cases}$

- $\dfrac{\partial f^i(t_j)}{\partial w_1^n} = \begin{cases} t_j^1 & \text{if } i = n \\ 0 & \text{otherwise} \end{cases}$

- $\dfrac{\partial f^i(t_j)}{\partial w_2^n} = \begin{cases} t_j^2 & \text{if } i = n \\ 0 & \text{otherwise.} \end{cases}$

That is,

$$\mathbf{J}\mathcal{D}^{\text{LM}}[f]$$

$$= \sum_{j=1}^{k} \sum_{i=1}^{2} 2 \left[f^i(t_j) - r_j^i \right] \left[\begin{array}{ccccccc} \frac{\partial f^i}{\partial c_1^1} & \frac{\partial f^i}{\partial c_2^1} & \cdots & \frac{\partial f^i}{\partial c_K^1} & \frac{\partial f^i}{\partial w_0^1} & \frac{\partial f^i}{\partial w_1^1} & \frac{\partial f^i}{\partial w_2^1} \\[2mm] \frac{\partial f^i}{\partial c_1^2} & \frac{\partial f^i}{\partial c_2^2} & \cdots & \frac{\partial f^i}{\partial c_K^2} & \frac{\partial f^i}{\partial w_0^2} & \frac{\partial f^i}{\partial w_1^2} & \frac{\partial f^i}{\partial w_2^2} \end{array} \right]$$

$$= \sum_{j=1}^{k} 2 \left[f^1(t_j) - r_j^1 \right] \left[\begin{array}{ccccccc} \|t_j - t_1\|^2 \log \|t_j - t_1\| & \|t_j - t_2\|^2 \log \|t_j - t_2\| & \cdots & \|t_j - t_K\|^2 \log \|t_j - t_K\| & 1 & t_j^1 & t_j^2 \\[2mm] 0 & 0 & 0 & 0 & 0 & 0 & 0 \end{array} \right]$$

$$+ \quad 2 \left[f^2(t_j) - r_j^2 \right] \left[\begin{array}{ccccccc} 0 & 0 & 0 & 0 & 0 & 0 & 0 \\[2mm] \|t_j - t_1\|^2 \log \|t_j - t_1\| & \|t_j - t_2\|^2 \log \|t_j - t_2\| & \cdots & \|t_j - t_K\|^2 \log \|t_j - t_K\| & 1 & t_j^1 & t_j^2 \end{array} \right].$$

C.2.2 Intensity Term $\mathcal{D}^{\text{INT}}$

The Jacobian of

$$\mathcal{D}^{\text{INT}}[f] = h \sum_{j=1}^{mn} \frac{1}{2} \left[\mathcal{T}[f(x_j)] - \mathcal{R}(x_j) \right]^2$$

with respect to the parameters of the thin plate spline transformation is

$$\mathbf{JD}^{\mathrm{INT}}[f] = h \sum_{j=1}^{mn} \left(\mathcal{T}\left[f(x_j)\right] - \mathcal{R}(x_j) \right) \left[\mathcal{T}_{x_j^1}\left[f\left(x_j\right)\right] \mathcal{T}_{x_j^2}\left[f\left(x_j\right)\right] \right] \cdot \frac{\partial f(x_j)}{\partial v},$$

where $\frac{\partial f}{\partial v} \in \mathbb{R}^{2 \times 2(K+3)}$ is the same as in C.1.

C.2.3 Smoothing Term $\mathcal{S}^{\mathrm{TPS}}$

$$\mathcal{S}^{\mathrm{TPS}}[f] = h \sum_{i=1}^{2} \mathcal{S}^{\mathrm{TPS}}[f^i]$$

$$= h \sum_{i=1}^{2} \sum_{j=1}^{mn} \left\langle \nabla^2 f^i(x_j), \nabla^2 f^i(x_j) \right\rangle,$$

where

- $\nabla f^i(x) = \begin{bmatrix} \sum_{j=1}^{K} c_j^i \left(x^1 - t_j^1 + 2(x^1 - t_j^1) \log \|x - t_j\| \right) + 0 + w_1^i + 0 \\ \sum_{j=1}^{K} c_j^i \left(x^2 - t_j^2 + 2(x^2 - t_j^2) \log \|x - t_j\| \right) + 0 + 0 + w_2^i \end{bmatrix}$

- $\nabla^2 f^i(x) = \begin{bmatrix} \frac{\partial^2 f^i}{\partial [x^1]^2} & \frac{\partial^2 f^i}{\partial x^1 \partial x^2} \\ \frac{\partial^2 f^i}{\partial x^2 \partial x^1} & \frac{\partial^2 f^i}{\partial [x^2]^2} \end{bmatrix}.$

For simplicity, let $H^i(x) := \nabla^2 f^i(x)$. $H^i(x)$ is symmetric, and its upper triangular entries are given by

- $[H^i(x)]_{1,1} = \sum_{j=1}^{K} c_j^i \left(1 + \frac{2(x^1 - t_j^1)^2}{\|x - t_j\|^2} + 2 \log \|x - t_j\| \right)$

- $[H^i(x)]_{1,2} = \sum_{j=1}^{K} \frac{2c_j^i(x^1 - t_j^1)(x^2 - t_j^2)}{\|x - t_j\|^2} = \left[H^i(x) \right]_{2,1}$

- $[H^i(x)]_{2,2} = \sum_{j=1}^{K} c_j^i \left(1 + \frac{2(x^2 - t_j^2)^2}{\|x - t_j\|^2} + 2 \log \|x - t_j\| \right).$

Therefore,

$$\mathcal{S}^{\text{TPS}}\left[f^i(x)\right] = \left\langle H^i(x), H^i(x)\right\rangle$$

$$= \left(\left[H^i(x)\right]_{1,1}\right)^2 + 2\left(\left[H^i(x)\right]_{1,2}\right)^2 + \left(\left[H^i(x)\right]_{2,2}\right)^2$$

$$= \left[\sum_{j=1}^{K} c_j^i\left(1 + \frac{2(x^1 - t_j^1)^2}{\|x - t_j\|^2} + 2\log\|x - t_j\|\right)\right]^2 + 2\left[\sum_{j=1}^{K}\frac{2c_j^i(x^1 - t_j^1)(x^2 - t_j^2)}{\|x - t_j\|^2}\right]^2$$

$$+ \left[\sum_{j=1}^{K} c_j^i\left(1 + \frac{2(x^2 - t_j^2)^2}{\|x - t_j\|^2} + 2\log\|x - t_j\|\right)\right]^2$$

and its derivative with respect to the parameters of the thin plate spline transformation is

$$\mathbf{J}\mathcal{S}^{\text{TPS}}[f^i] = \left[\begin{array}{ccccccc|cccccc} \frac{\partial f^i}{\partial c_1^1} & \frac{\partial f^i}{\partial c_2^1} & \cdots & \frac{\partial f^i}{\partial c_K^1} & \frac{\partial f^i}{\partial w_0^1} & \frac{\partial f^i}{\partial w_1^1} & \frac{\partial f^i}{\partial w_2^1} & \frac{\partial f^i}{\partial c_1^2} & \frac{\partial f^i}{\partial c_2^2} & \cdots & \frac{\partial f^i}{\partial c_K^2} & \frac{\partial f^i}{\partial w_0^2} & \frac{\partial f^i}{\partial w_1^2} & \frac{\partial f^i}{\partial w_2^2} \end{array}\right],$$

where

- $$\frac{\partial f^i}{\partial c_j^a} = \begin{cases} 2\left(\sum_{l=1}^{K} c_l^i\left[1 + \frac{2(x^1 - t_l^1)^2}{\|x - t_l\|}\right]\right)\left(1 + \frac{2(x^1 - t_j^1)^2}{\|x - t_j\|}\right) \\ +4\left(\sum_{l=1}^{K}\frac{2c_l^i(x^1 - t_l^1)(x^2 - t_l^2)}{\|x - t_l\|}\right)\left(\frac{2(x^1 - t_j^1)(x^2 - t_j^2)}{\|x - t_j\|}\right) \quad \text{if } i = a \\ +2\left(\sum_{l=1}^{K} c_l^i\left[1 + \frac{2(x^2 - t_l^2)^2}{\|x - t_l\|}\right]\right)\left(1 + \frac{2(x^2 - t_j^2)^2}{\|x - t_j\|}\right) \\ \\ 0 \qquad\qquad\qquad\qquad\qquad\qquad\qquad\qquad\qquad\qquad \text{otherwise} \end{cases}$$

- $\frac{\partial f^i}{\partial w_j^i} = 0$ for $j = 0, 1, 2$, $i = 1, 2$.

Appendix D

Landmark and Contour Matching: Discretized Model and Derivatives

Landmark- and Contour-Based Registration with Thin Plate Spline Transformations

$$\min_f \mathcal{J}[f] = \mathcal{D}^{\text{LM}}[f] + \alpha \mathcal{C}[f],$$

where

- $\mathcal{D}^{\text{LM}}$ denotes sum of squared landmark distances,

- $\mathcal{C}$ denotes the contour matching term,

- $f^i(x)$ is a thin plate spline transformation (2.19), and

- $v = [v^1, \cdots, v^d]^T \in \mathbb{R}^{d(K+d+1)}$ is the vector of TPS transformation parameters.

D.1   2D Landmark and Contour Registration

D.1.1   Landmark Term $\mathcal{D}^{\text{LM}}$

Recall that

$$\frac{\partial \mathcal{D}^{\text{LM}}[f]}{\partial v}$$

$$= \sum_{j=1}^{k} \sum_{i=1}^{2} 2\left[f^i(t_j) - r_j^i\right] \left[\begin{array}{cccccccc} \frac{\partial f^i}{\partial c_1^1} & \frac{\partial f^i}{\partial c_2^1} & \cdots & \frac{\partial f^i}{\partial c_K^1} & \frac{\partial f^i}{\partial w_0^1} & \frac{\partial f^i}{\partial w_1^1} & \frac{\partial f^i}{\partial w_2^1} \\[2mm] \frac{\partial f^i}{\partial c_1^2} & \frac{\partial f^i}{\partial c_2^2} & \cdots & \frac{\partial f^i}{\partial c_K^2} & \frac{\partial f^i}{\partial w_0^2} & \frac{\partial f^i}{\partial w_1^2} & \frac{\partial f^i}{\partial w_2^2} \end{array}\right]$$

$$= \sum_{j=1}^{K} 2\left[f^1(t_j) - r_j^1\right] \left[\begin{array}{cccccccc} \|t_j - t_1\|^2 \log\|t_j - t_1\| & \|t_j - t_2\|^2 \log\|t_j - t_2\| & \cdots & \|t_j - t_K\|^2 \log\|t_j - t_K\| & 1 & t_j^1 & t_j^2 \\[2mm] 0 & 0 & 0 & 0 & 0 & 0 & 0 \end{array}\right]$$

$$+ \; 2\left[f^2(t_j) - r_j^2\right] \left[\begin{array}{cccccccc} 0 & 0 & 0 & 0 & 0 & 0 & 0 \\[2mm] \|t_j - t_1\|^2 \log\|t_j - t_1\| & \|t_j - t_2\|^2 \log\|t_j - t_2\| & \cdots & \|t_j - t_K\|^2 \log\|t_j - t_K\| & 1 & t_j^1 & t_j^2 \end{array}\right]$$

$$\tag{D.1}$$

Let

$$
A = \begin{bmatrix}
\|t_1 - t_1\|^2 \log \|t_1 - t_1\| & \|t_1 - t_2\|^2 \log \|t_1 - t_2\| & \cdots & \|t_1 - t_K\|^2 \log \|t_1 - t_K\| & 1 & t_1^1 & t_1^2 \\
\|t_2 - t_1\|^2 \log \|t_2 - t_1\| & \|t_2 - t_2\|^2 \log \|t_2 - t_2\| & \cdots & \|t_2 - t_K\|^2 \log \|t_2 - t_K\| & 1 & t_2^1 & t_2^2 \\
\vdots & \vdots & \ddots & \vdots & \vdots & \vdots & \vdots \\
\|t_K - t_1\|^2 \log \|t_K - t_1\| & \|t_K - t_2\|^2 \log \|t_K - t_2\| & \cdots & \|t_K - t_K\|^2 \log \|t_K - t_K\| & 1 & t_K^1 & t_K^2
\end{bmatrix}.
$$

The exact Hessian of $\mathcal{D}^{\text{LM}}$ with respect to the TPS transformation parameters is given by the block matrix

$$
H^{\text{LM}} = \begin{bmatrix} \mathbf{H}_{\text{base}} & \mathbf{0} \\ \mathbf{0} & \mathbf{H}_{\text{base}} \end{bmatrix}
$$

where the (i, j) entry of $\mathbf{H}_{\text{base}}$ is given by the dot product of the ith and j^{th} columns of A, i.e.,

$$
\mathbf{H}_{\text{base}}(i, j) = 2 \left\langle A_{*j}, A_{*i} \right\rangle.
$$

D.1.2   Contour Matching Term $\mathcal{C}$

$$
C[f] = \alpha \sum_{i=1}^{L} \frac{1}{2} \left[1 - \left(v\left[f\left(\overset{*}{t}_i \right) \right] \cdot v\left[\overset{*}{r}_i \right] \right)^2 \right]
$$

where

- $v\left[\overset{*}{r}_i \right] = \dfrac{\overrightarrow{\overset{*}{r}_i \overset{*}{r}_{i+1}}}{\left\| \overrightarrow{\overset{*}{r}_i \overset{*}{r}_{i+1}} \right\|} = \dfrac{\left\langle \overset{*1}{r}_{i+1} - \overset{*1}{r}_i, \overset{*2}{r}_{i+1} - \overset{*2}{r}_i \right\rangle}{\left\| \left\langle \overset{*1}{r}_{i+1} - \overset{*1}{r}_i, \overset{*2}{r}_{i+1} - \overset{*2}{r}_i \right\rangle \right\|}$

- $v\left[f\left(\overset{*}{t}_i \right) \right] = \dfrac{\overrightarrow{f\left(\overset{*}{t}_i \right) f\left(\overset{*}{t}_{i+1} \right)}}{\left\| \overrightarrow{f\left(\overset{*}{t}_i \right) f\left(\overset{*}{t}_{i+1} \right)} \right\|} = \dfrac{\left\langle f^1\left(\overset{*}{t}_{i+1} \right) - f^1\left(\overset{*}{t}_i \right), f^2\left(\overset{*}{t}_{i+1} \right) - f^2\left(\overset{*}{t}_i \right) \right\rangle}{\left\| \left\langle f^1\left(\overset{*}{t}_{i+1} \right) - f^1\left(\overset{*}{t}_i \right), f^2\left(\overset{*}{t}_{i+1} \right) - f^2\left(\overset{*}{t}_i \right) \right\rangle \right\|}$

- $f\left(\overset{*}{t}_i \right) = \begin{bmatrix} \sum_{j=1}^{K} c_i^1 \left\| \overset{*}{t}_i - t_j \right\|^2 \log \left\| \overset{*}{t}_i - t_j \right\| + w_0^1 + w_1^1 \overset{*1}{t}_i + w_2^1 \overset{*2}{t}_i \\ \sum_{j=1}^{K} c_i^2 \left\| \overset{*}{t}_i - t_j \right\|^2 \log \left\| \overset{*}{t}_i - t_j \right\| + w_0^2 + w_1^2 \overset{*1}{t}_i + w_2^2 \overset{*2}{t}_i \end{bmatrix} =: \begin{bmatrix} f^1\left(\overset{*}{t}_i \right) \\ f^2\left(\overset{*}{t}_i \right) \end{bmatrix}$

- $v\left[f\left(\overset{*}{t_i}\right)\right]\cdot v\left[\overset{*}{r_i}\right] = \dfrac{\left[f^1\left(\overset{*}{t_{i+1}}\right)-f^1\left(\overset{*}{t_i}\right)\right]\left[\overset{*1}{r_{i+1}}-\overset{*1}{r_i}\right]+\left[f^2\left(\overset{*}{t_{i+1}}\right)-f^2\left(\overset{*}{t_i}\right)\right]\left[\overset{*2}{r_{i+1}}-\overset{*2}{r_i}\right]}{\left\|\left\langle f^1\left(\overset{*}{t_{i+1}}\right)-f^1\left(\overset{*}{t_i}\right),f^2\left(\overset{*}{t_{i+1}}\right)-f^2\left(\overset{*}{t_i}\right)\right\rangle\right\|\left\|\left\langle\overset{*1}{r_{i+1}}-\overset{*1}{r_i},\overset{*2}{r_{i+1}}-\overset{*2}{r_i}\right\rangle\right\|}$

For $d=1,2$, let

- $R_i^d := \overset{*d}{r_{i+1}} - \overset{*d}{r_i}$ and

- $T_i^d := f^d\left(\overset{*}{t_{i+1}}\right) - f^d\left(\overset{*}{t_i}\right)$

$$= \sum_{j=1}^{K} c_j^d\left(\left\|\overset{*}{t_{i+1}}-t_j\right\|^2\log\left\|\overset{*}{t_{i+1}}-t_j\right\| - \left\|\overset{*}{t_i}-t_j\right\|^2\log\left\|\overset{*}{t_i}-t_j\right\|\right)$$

$$+(w_0^d-w_0^d)+w_1^d(\overset{*1}{t_{i+1}}-\overset{*1}{t_i})+w_2^d(\overset{*2}{t_{i+1}}-\overset{*2}{t_i}).$$

Also, define

- $C_i = \dfrac{\alpha}{2}\left[1-\left(v\left[f\left(\overset{*}{t_i}\right)\right]\cdot v\left[\overset{*}{r_i}\right]\right)^2\right]$

- $C_i^{\text{left}} = \left[(T_i^1)^2+(T_i^2)^2\right]^{-1/2}$

- $C_i^{\text{right}} = \dfrac{T_i^1R_i^1+T_i^2R_i^2}{\left\|\overrightarrow{\overset{*}{r_i}\,\overset{*}{r_{i+1}}}\right\|}.$

Then

- $\left\|\overrightarrow{\overset{*}{r_i}\,\overset{*}{r_{i+1}}}\right\| = \left[(R_i^1)^2+(R_i^2)^2\right]^{1/2}$

- $\left\|\overrightarrow{f\left(\overset{*}{t_i}\right)f\left(\overset{*}{t_{i+1}}\right)}\right\| = \left[(T_i^1)^2+(T_i^2)^2\right]^{1/2}$

- $v\left[f\left(\overset{*}{t_i}\right)\right]\cdot v\left[\overset{*}{r_i}\right] = \dfrac{T_i^1R_i^1+T_i^2R_i^2}{\left[(T_i^1)^2+(T_i^2)^2\right]^{1/2}\left[(R_i^1)^2+(R_i^2)^2\right]^{1/2}}$

And the contour matching term C is

$$C[f] = \alpha \sum_{i=1}^{L} \frac{1}{2} \left[1 - \left(v \left[f \left(\overset{*}{t}_i \right) \right] \cdot v \left[\overset{*}{r}_i \right] \right)^2 \right]$$

$$= \alpha \sum_{i=1}^{L} \frac{1}{2} \left[1 - \left(\frac{T_i^1 R_i^1 + T_i^2 R_i^2}{\left[(T_i^1)^2 + (T_i^2)^2 \right]^{1/2} \left\| \overrightarrow{\overset{*}{r}_i \overset{*}{r}_{i+1}} \right\|} \right)^2 \right]$$

$$= \alpha \sum_{i=1}^{L} \frac{1}{2} \left[1 - \left(\overbrace{\left[(T_i^1)^2 + (T_i^2)^2 \right]^{-1/2}}^{C_i^{\text{left}}} \cdot \overbrace{\frac{T_i^1 R_i^1 + T_i^2 R_i^2}{\left\| \overrightarrow{\overset{*}{r}_i \overset{*}{r}_{i+1}} \right\|}}^{C_i^{\text{right}}} \right)^2 \right]$$

The derivative of the ith contour-matching term C_i with respect to the parameters $v = [v^1, v^2]^T \in \mathbb{R}^{2(K+3)}$ of the thin plate spline transformation is

$$\nabla C_i[f] = -\frac{\alpha}{2} \cdot 2 \left(C_i^{\text{left}} C_i^{\text{right}} \right) \left[\nabla \left(C_i^{\text{left}} C_i^{\text{right}} \right) \right]$$

$$= -\alpha C_i^{\text{left}} C_i^{\text{right}}$$

$$\cdot \left[C_i^{\text{left}} \left(\begin{bmatrix} \frac{\partial C_i^{\text{right}}}{\partial c_1^1} & \cdots & \frac{\partial C_i^{\text{right}}}{\partial c_K^1} & \frac{\partial C_i^{\text{right}}}{\partial w_0^1} & \frac{\partial C_i^{\text{right}}}{\partial w_1^1} & \frac{\partial C_i^{\text{right}}}{\partial w_2^1} \\ \frac{\partial C_i^{\text{right}}}{\partial c_1^2} & \cdots & \frac{\partial C_i^{\text{right}}}{\partial c_K^2} & \frac{\partial C_i^{\text{right}}}{\partial w_0^2} & \frac{\partial C_i^{\text{right}}}{\partial w_1^2} & \frac{\partial C_i^{\text{right}}}{\partial w_2^2} \end{bmatrix} \right) \right.$$

$$+ \left(-\frac{C_i^{\text{right}} \left(C_i^{\text{left}} \right)^{-3/2}}{2} \right) \left[2T_i^1 \left(\begin{bmatrix} \frac{\partial T_i^1}{\partial c_1^1} & \cdots & \frac{\partial T_i^1}{\partial c_K^1} & \frac{\partial T_i^1}{\partial w_0^1} & \frac{\partial T_i^1}{\partial w_1^1} & \frac{\partial T_i^1}{\partial w_2^1} \\ \frac{\partial T_i^1}{\partial c_1^2} & \cdots & \frac{\partial T_i^1}{\partial c_K^2} & \frac{\partial T_i^1}{\partial w_0^2} & \frac{\partial T_i^1}{\partial w_1^2} & \frac{\partial T_i^1}{\partial w_2^2} \end{bmatrix} \right) \right.$$

$$\left. \left. + 2T_i^2 \left(\begin{bmatrix} \frac{\partial T_i^2}{\partial c_1^1} & \cdots & \frac{\partial T_i^2}{\partial c_K^1} & \frac{\partial T_i^2}{\partial w_0^1} & \frac{\partial T_i^2}{\partial w_1^1} & \frac{\partial T_i^2}{\partial w_2^1} \\ \frac{\partial T_i^2}{\partial c_1^2} & \cdots & \frac{\partial T_i^2}{\partial c_K^2} & \frac{\partial T_i^2}{\partial w_0^2} & \frac{\partial T_i^2}{\partial w_1^2} & \frac{\partial T_i^2}{\partial w_2^2} \end{bmatrix} \right) \right] \right]$$

$$= -\alpha \left[\overbrace{C_i^{\text{right}} \left[\left(T_i^1 \right)^2 + \left(T_i^2 \right)^2 \right]^{-1} \left(\begin{bmatrix} \frac{\partial C_i^{\text{right}}}{\partial c_1^1} & \cdots & \frac{\partial C_i^{\text{right}}}{\partial c_K^1} & \frac{\partial C_i^{\text{right}}}{\partial w_0^1} & \frac{\partial C_i^{\text{right}}}{\partial w_1^1} & \frac{\partial C_i^{\text{right}}}{\partial w_2^1} \\ \frac{\partial C_i^{\text{right}}}{\partial c_1^2} & \cdots & \frac{\partial C_i^{\text{right}}}{\partial c_K^2} & \frac{\partial C_i^{\text{right}}}{\partial w_0^2} & \frac{\partial C_i^{\text{right}}}{\partial w_1^2} & \frac{\partial C_i^{\text{right}}}{\partial w_2^2} \end{bmatrix} \right)}^{D_1} \right.$$

$$\overbrace{- \left(C_i^{\text{right}} \right)^2 \left[\left(T_i^1 \right)^2 + \left(T_i^2 \right)^2 \right]^{-2} T_i^1 \left(\begin{bmatrix} \frac{\partial T_i^1}{\partial c_1^1} & \cdots & \frac{\partial T_i^1}{\partial c_K^1} & \frac{\partial T_i^1}{\partial w_0^1} & \frac{\partial T_i^1}{\partial w_1^1} & \frac{\partial T_i^1}{\partial w_2^1} \\ \frac{\partial T_i^1}{\partial c_1^2} & \cdots & \frac{\partial T_i^1}{\partial c_K^2} & \frac{\partial T_i^1}{\partial w_0^2} & \frac{\partial T_i^1}{\partial w_1^2} & \frac{\partial T_i^1}{\partial w_2^2} \end{bmatrix} \right)}^{D_2}$$

$$\overbrace{- \left(C_i^{\text{right}} \right)^2 \left[\left(T_i^1 \right)^2 + \left(T_i^2 \right)^2 \right]^{-2} T_i^2 \left(\begin{bmatrix} \frac{\partial T_i^2}{\partial c_1^1} & \cdots & \frac{\partial T_i^2}{\partial c_K^1} & \frac{\partial T_i^2}{\partial w_0^1} & \frac{\partial T_i^2}{\partial w_1^1} & \frac{\partial T_i^2}{\partial w_2^1} \\ \frac{\partial T_i^2}{\partial c_1^2} & \cdots & \frac{\partial T_i^2}{\partial c_K^2} & \frac{\partial T_i^2}{\partial w_0^2} & \frac{\partial T_i^2}{\partial w_1^2} & \frac{\partial T_i^2}{\partial w_2^2} \end{bmatrix} \right)}^{D_3} \left. \right]$$

$$\text{(D.2)}$$

where

- $\frac{\partial C_i^{\text{right}}}{\partial c_j^k} = \frac{\overset{*k}{r}_{i+1} - \overset{*k}{r}_i}{\left\| \overrightarrow{\overset{*}{r}_i \overset{*}{r}_{i+1}} \right\|} \left(\left\| \overset{*}{t}_{i+1} - t_j \right\|^2 \log \left\| \overset{*}{t}_{i+1} - t_j \right\| - \left\| \overset{*}{t}_i - t_j \right\|^2 \log \left\| \overset{*}{t}_i - t_j \right\| \right)$ for $k = 1, 2$

- $\frac{\partial C_i^{\text{right}}}{\partial w_0^i} = 0$

- $\dfrac{\partial C_i^{\text{right}}}{\partial w_1^k} = \dfrac{\overset{*k}{r}_{i+1} - \overset{*k}{r}_i}{\left\|\overrightarrow{\overset{*}{r}_i \overset{*}{r}_{i+1}}\right\|}\left(\overset{*1}{t}_{i+1} - \overset{*1}{t}_i\right)$

- $\dfrac{\partial C_i^{\text{right}}}{\partial w_2^i} = \dfrac{\overset{*k}{r}_{i+1} - \overset{*k}{r}_i}{\left\|\overrightarrow{\overset{*}{r}_i \overset{*}{r}_{i+1}}\right\|}\left(\overset{*2}{t}_{i+1} - \overset{*2}{t}_i\right)$

- $\dfrac{\partial T_i^m}{\partial c_j^k} = \begin{cases} \left\|\overset{*}{t}_{i+1} - t_j\right\|^2 \log\left\|\overset{*}{t}_{i+1} - t_j\right\| - \left\|\overset{*}{t}_i - t_j\right\|^2 \log\left\|\overset{*}{t}_i - t_j\right\| & \text{if } m = k \\ 0 & \text{if } m \neq k \end{cases}$

- $\dfrac{\partial T_i^m}{\partial w_0^k} = 0$

- $\dfrac{\partial T_i^m}{\partial w_1^k} = \begin{cases} \overset{*1}{t}_{i+1} - \overset{*1}{t}_i & \text{if } m = k \\ 0 & \text{if } m \neq k \end{cases}$

- $\dfrac{\partial T_i^m}{\partial w_2^k} = \begin{cases} \overset{*2}{t}_{i+1} - \overset{*2}{t}_i & \text{if } m = k \\ 0 & \text{if } m \neq k \end{cases}$

To simplify the computation of the Hessian of the **i^{th} addend** of the CM term, we instead compute the sum of the Hessians $H_1, H_2, H_3 \in \mathbb{R}^{2(K+3)\times 2(K+3)}$ corresponding to the components $D_1, D_2, D_3 \in \mathbb{R}^{1\times 2(K+3)}$ of $\frac{\partial C_i}{\partial v}$.

First, we have

$$H_1(m,n) = \frac{\partial \overbrace{D_1(1,n)}^{n^{\text{th}}\text{entry of } D_1}}{\partial \underbrace{D_1(1,m)}_{m^{\text{th}}\text{entry of } D_1}} = \begin{bmatrix} A & B \\ F & G \end{bmatrix}$$

where

- $A(m,n) = A_1(m,n)\left(-C_i^{\text{right}}\left[(T_i^1)^2 + (T_i^2)^2\right]^{-2}(2T_i^1 A_2(m,n)) + \left[(T_i^1)^2 + (T_i^2)^2\right]^{-1} A_3(m,n)\right)$

- $B(m,n) = B_1(m,n)\left(-C_i^{\text{right}}\left[(T_i^1)^2 + (T_i^2)^2\right]^{-2}(2T_i^1 B_2(m,n)) + \left[(T_i^1)^2 + (T_i^2)^2\right]^{-1} B_3(m,n)\right)$

- $F(m,n) = F_1(m,n)\left(-C_i^{\text{right}}\left[(T_i^1)^2 + (T_i^2)^2\right]^{-2}(2T_i^2 F_2(m,n)) + \left[(T_i^1)^2 + (T_i^2)^2\right]^{-1} F_3(m,n)\right)$

- $G(m,n) = G_1(m,n)\left(-C_i^{\text{right}}\left[(T_i^1)^2 + (T_i^2)^2\right]^{-2}(2T_i^2 G_2(m,n)) + \left[(T_i^1)^2 + (T_i^2)^2\right]^{-1} G_3(m,n)\right)$

with

- $A_1(m,n) = \begin{cases} \dfrac{\overset{*1}{r}_{i+1} - \overset{*1}{r}_i}{\|\overrightarrow{r_i r_{i+1}}\|}\left(\begin{array}{l}\left\|\overset{*}{t}_{i+1} - t_n\right\|^2 \log\left\|\overset{*}{t}_{i+1} - t_n\right\| \\ -\left\|\overset{*}{t}_i - t_n\right\|^2 \log\left\|\overset{*}{t}_i - t_n\right\|\end{array}\right) & n \le K \\[18pt] 0 & n = K+1 \\[8pt] \dfrac{\overset{*1}{r}_{i+1} - \overset{*1}{r}_i}{\|\overrightarrow{r_i r_{i+1}}\|}\left(\overset{*1}{t}_{i+1} - \overset{*1}{t}_i\right) & n = K+2 \\[12pt] \dfrac{\overset{*1}{r}_{i+1} - \overset{*1}{r}_i}{\|\overrightarrow{r_i r_{i+1}}\|}\left(\overset{*2}{t}_{i+1} - \overset{*2}{t}_i\right) & n = K+3 \end{cases}$

- $A_2(m,n) = \begin{cases} \left\|\overset{*}{t}_{i+1} - t_m\right\|^2 \log\left\|\overset{*}{t}_{i+1} - t_m\right\| - \left\|\overset{*}{t}_i - t_m\right\|^2 \log\left\|\overset{*}{t}_i - t_m\right\| & m \le K \\[12pt] 0 & m = K+1 \\[6pt] \overset{*1}{t}_{i+1} - \overset{*1}{t}_i & m = K+2 \\[8pt] \overset{*2}{t}_{i+1} - \overset{*2}{t}_i & m = K+3 \end{cases}$

- $A_3(m,n) = \begin{cases} \dfrac{\overset{*1}{r}_{i+1} - \overset{*1}{r}_i}{\|\overrightarrow{r_i r_{i+1}}\|}\left(\left\|\overset{*}{t}_{i+1} - t_m\right\|^2 \log\left\|\overset{*}{t}_{i+1} - t_m\right\| - \left\|\overset{*}{t}_i - t_m\right\|^2 \log\left\|\overset{*}{t}_i - t_m\right\|\right) & m \le K \\[18pt] 0 & m = K+1 \\[8pt] \dfrac{\overset{*1}{r}_{i+1} - \overset{*1}{r}_i}{\|\overrightarrow{r_i r_{i+1}}\|}\left(\overset{*1}{t}_{i+1} - \overset{*1}{t}_i\right) & m = K+2 \\[12pt] \dfrac{\overset{*1}{r}_{i+1} - \overset{*1}{r}_i}{\|\overrightarrow{r_i r_{i+1}}\|}\left(\overset{*2}{t}_{i+1} - \overset{*2}{t}_i\right) & m = K+3 \end{cases}$

- $B_1(m,n) = \begin{cases} \dfrac{\overset{*2}{r}_{i+1} - \overset{*2}{r}_i}{\|\overrightarrow{r_i r_{i+1}}\|}\left(\begin{array}{l}\left\|\overset{*}{t}_{i+1} - t_n\right\|^2 \log\left\|\overset{*}{t}_{i+1} - t_n\right\| \\ -\left\|\overset{*}{t}_i - t_n\right\|^2 \log\left\|\overset{*}{t}_i - t_n\right\|\end{array}\right) & n \le K \\[18pt] 0 & n = K+1 \\[8pt] \dfrac{\overset{*2}{r}_{i+1} - \overset{*2}{r}_i}{\|\overrightarrow{r_i r_{i+1}}\|}\left(\overset{*1}{t}_{i+1} - \overset{*1}{t}_i\right) & n = K+2 \\[12pt] \dfrac{\overset{*2}{r}_{i+1} - \overset{*2}{r}_i}{\|\overrightarrow{r_i r_{i+1}}\|}\left(\overset{*2}{t}_{i+1} - \overset{*2}{t}_i\right) & n = K+3 \end{cases}$

- $B_2(m,n) = A_2(m,n)$

- $B_3(m,n) = A_3(m,n)$

- $F_1(m, n) = A_1(m, n)$

- $F_2(m, n) = A_2(m, n)$

- $F_3(m, n) = \begin{cases} \dfrac{\overset{*2}{r}_{i+1} - \overset{*2}{r}_i}{\|\overrightarrow{r_i r_{i+1}}\|} \left(\left\| \overset{*}{t}_{i+1} - t_m \right\|^2 \log \left\| \overset{*}{t}_{i+1} - t_m \right\| - \left\| \overset{*}{t}_i - t_m \right\|^2 \log \left\| \overset{*}{t}_i - t_m \right\| \right) & m \leq K \\[2ex] 0 & m = K+1 \\[2ex] \dfrac{\overset{*2}{r}_{i+1} - \overset{*2}{r}_i}{\|\overrightarrow{r_i r_{i+1}}\|} \left(\overset{*1}{t}_{i+1} - \overset{*1}{t}_i \right) & m = K+2 \\[2ex] \dfrac{\overset{*2}{r}_{i+1} - \overset{*2}{r}_i}{\|\overrightarrow{r_i r_{i+1}}\|} \left(\overset{*2}{t}_{i+1} - \overset{*2}{t}_i \right) & m = K+3 \end{cases}$

- $G_1(m, n) = B_1(m, n)$

- $G_2(m, n) = A_2(m, n)$

- $G_3(m, n) = C_3(m, n)$

for $m, n = 1, \ldots, K + 3$.

Now,

$$H_2(m, n) = \frac{\partial \overbrace{D_2(1, n)}^{n^{\text{th}}\text{entry of } D_2}}{\partial \underbrace{D_2(1, m)}_{m^{\text{th}}\text{entry of } D_2}} = \begin{bmatrix} J & \mathbf{0} \\ K & \mathbf{0} \end{bmatrix},$$

where

- $\begin{aligned} J(m, n) = \ & -J_1(m, n) \left[\left(C_i^{\text{right}} \right)^2 \left[(T_i^1)^2 + (T_i^2)^2 \right]^{-2} J_2(m, n) \right. \\ & \left. - 4 \left(C_i^{\text{right}} \right)^2 T_i^1 T_i^1 \left[(T_i^1)^2 + (T_i^2)^2 \right]^{-3} J_2(m, n) \right. \\ & \left. + \left[(T_i^1)^2 + 2 (T_i^2)^2 \right]^{-2} T_i^1 C_i^{\text{right}} J_3(m, n) \right] \end{aligned}$

- $\begin{aligned} K(m, n) = \ & -K_1(m, n) \left[-4 \left(C_i^{\text{right}} \right)^2 T_i^1 T_i^2 \left[(T_i^1)^2 + (T_i^2)^2 \right]^{-3} K_2(m, n) \right. \\ & \left. + \left[(T_i^1)^2 + 2 (T_i^2)^2 \right]^{-2} T_i^1 C_i^{\text{right}} K_3(m, n) \right] \end{aligned}$

- $J_1(m, n) = \begin{cases} \left\| \overset{*}{t}_{i+1} - t_n \right\|^2 \log \left\| \overset{*}{t}_{i+1} - t_n \right\| - \left\| \overset{*}{t}_i - t_n \right\|^2 \log \left\| \overset{*}{t}_i - t_n \right\| & n \leq K \\[2ex] 0 & n = K+1 \\[2ex] \overset{*1}{t}_{i+1} - \overset{*1}{t}_i & n = K+2 \\[2ex] \overset{*2}{t}_{i+1} - \overset{*2}{t}_i & n = K+3 \end{cases}$

- $J_2(m, n) = A_2(m, n)$

- $J_3(m, n) = A_3(m, n)$

- $K_1(m, n) = J_1(m, n)$

- $K_2(m, n) = A_2(m, n)$

- $K_3(m, n) = F_3(m, n)$

Finally,

$$H_3(m, n) = \frac{\partial \overbrace{D_3(1, n)}^{n^{\text{th}}\text{entry of } D_3}}{\partial \underbrace{D_3(1, m)}_{m^{\text{th}}\text{entry of } D_3}} = \begin{bmatrix} \mathbf{0} & L \\ \mathbf{0} & M \end{bmatrix}$$

where

- $L(m, n) = -L_1(m, n) \left[-4 \left(C_i^{\text{right}} \right)^2 T_i^2 T_i^1 \left[(T_i^1)^2 + (T_i^2)^2 \right]^{-3} L_2(m, n) \right.$
  $\left. + \left[(T_i^1)^2 + 2 (T_i^2)^2 \right]^{-2} T_i^2 C_i^{\text{right}} L_3(m, n) \right]$

- $M(m, n) = -M_1(m, n) \left[\left(C_i^{\text{right}} \right)^2 \left[(T_i^1)^2 + (T_i^2)^2 \right]^{-2} M_2(m, n) \right.$
  $-4 \left(C_i^{\text{right}} \right)^2 T_i^2 T_i^2 \left[(T_i^1)^2 + (T_i^2)^2 \right]^{-3} M_2(m, n)$
  $\left. + \left[(T_i^1)^2 + 2 (T_i^2)^2 \right]^{-2} T_i^2 C_i^{\text{right}} M_3(m, n) \right]$

- $L_1(m, n) = J_1(m, n)$

- $L_2(m, n) = A_2(m, n)$

- $L_3(m, n) = A_3(m, n)$

- $M_1(m, n) = J_1(m, n)$

- $M_2(m, n) = A_2(m, n)$

- $M_3(m, n) = F_3(m, n)$.

Bibliography

[1] Cardiovascular diseases. `http://www.who.int/mediacentre/factsheets/fs317/en`. Accessed: 26-January-2018.

[2] Khadijeh Aghajani, Mohammad T Manzuri, and Rohollah Yousefpour. A robust image registration method based on total variation regularization under complex illumination changes. *Computer methods and programs in biomedicine*, 134:89–107, 2016.

[3] Daniel C Alexander, Carlo Pierpaoli, Peter J Basser, and James C Gee. Spatial transformations of diffusion tensor magnetic resonance images. *IEEE transactions on medical imaging*, 20(11):1131–1139, 2001.

[4] Yali Amit. A nonlinear variational problem for image matching. *SIAM Journal on Scientific Computing*, 15(1):207–224, 1994.

[5] Howard Anton, Irl Bivens, Stephen Davis, and Thomas Polaski. *Calculus: Early transcendentals*. Wiley Hoboken, NJ, 2010.

[6] Vincent Arsigny, Olivier Commowick, Nicholas Ayache, and Xavier Pennec. A fast and log-euclidean polyaffine framework for locally linear registration. *Journal of Mathematical Imaging and Vision*, 33(2):222–238, 2009.

[7] Vincent Arsigny, Pierre Fillard, Xavier Pennec, and Nicholas Ayache. Log-Euclidean metrics for fast and simple calculus on diffusion tensors. *Magnetic Resonance in Medicine: An Official Journal of the International Society for Magnetic Resonance in Medicine*, 56(2):411–421, 2006.

[8] Haruo Asada and Michael Brady. The curvature primal sketch. *IEEE transactions on pattern analysis and machine intelligence*, (1):2–14, 1986.

[9] John Ashburner. A fast diffeomorphic image registration algorithm. *Neuroimage*, 38(1):95–113, 2007.

[10] Andrew J Asman, Frederick W Bryan, Seth A Smith, Daniel S Reich, and Bennett A Landman. Groupwise multi-atlas segmentation of the spinal cord's internal structure. *Medical image analysis*, 18(3):460–471, 2014.

[11] Brian Avants and James C Gee. Shape averaging with diffeomorphic flows for atlas creation. In *Biomedical Imaging: Nano to Macro, 2004. IEEE International Symposium on*, pages 595–598. IEEE, 2004.

[12] Brian B Avants, Charles L Epstein, Murray Grossman, and James C Gee. Symmetric diffeomorphic image registration with cross-correlation: evaluating automated labeling of elderly and neurodegenerative brain. *Medical image analysis*, 12(1):26–41, 2008.

[13] Stephanie L Barnes, Jennifer G Whisenant, Xia Li, and Thomas E Yankeelov. Techniques and applications of dynamic contrast enhanced magnetic resonance imaging in cancer. In *2014 36th Annual International Conference of the IEEE Engineering in Medicine and Biology Society*, pages 4264–4267. IEEE, 2014.

[14] Mirza Faisal Beg, Patrick A Helm, Elliot McVeigh, Michael I Miller, and Raimond L Winslow. Computational cardiac anatomy using MRI. *Magnetic resonance in medicine*, 52(5):1167–1174, 2004.

[15] Maurizio Bergamino, Laura Saitta, Laura Barletta, Laura Bonzano, Giovanni Luigi Mancardi, Lucio Castellan, Jean Louis Ravetti, and Luca Roccatagliata. Measurement of blood-brain barrier permeability with t1-weighted dynamic contrast-enhanced mri in brain tumors: a comparative study with two different algorithms. *International Scholarly Research Notices*, 2013, 2013.

[16] Kanwal K Bhatia, Paul Aljabar, James P Boardman, Latha Srinivasan, Maria Murgasova, Serena J Counsell, Mary A Rutherford, Joseph V Hajnal, A David Edwards, and Daniel Rueckert. Groupwise combined segmentation and registration for atlas construction. In *International Conference on Medical Image Computing and Computer-Assisted Intervention*, pages 532–540. Springer, 2007.

[17] Fred L. Bookstein. Principal warps: Thin-plate splines and the decomposition of deformations. *IEEE Transactions on pattern analysis and machine intelligence*, 11(6):567–585, 1989.

[18] Michael Brady, Jean Ponce, Alan Yuille, and Haruo Asada. Describing surfaces. *Computer Vision, Graphics, and Image Processing*, 32(1):1–28, 1985.

[19] Gunnar Brix, Wolfhard Semmler, Rüdiger Port, Lothar R Schad, Günter Layer, and Walter J Lorenz. Pharmacokinetic parameters in CNS Gd-DTPA enhanced MR imaging. *Journal of computer assisted tomography*, 15(4):621–628, 1991.

[20] David L Buckley. Uncertainty in the analysis of tracer kinetics using dynamic contrast-enhanced t1-weighted mri. *Magnetic Resonance in Medicine: An Official Journal of the International Society for Magnetic Resonance in Medicine*, 47(3):601–606, 2002.

[21] Martin Buhmann. A new class of radial basis functions with compact support. *Mathematics of Computation*, 70(233):307–318, 2001.

[22] Giovanni A Buonaccorsi, Caleb Roberts, Sue Cheung, Yvonne Watson, James PB O'Connor, Karen Davies, Alan Jackson, Gordon C Jayson, and Geoff JM Parker. Comparison of the performance of tracer kinetic model-driven registration for dynamic contrast enhanced MRI using different models of contrast enhancement. *Academic radiology*, 13(9):1112–1123, 2006.

[23] Martin Burger and Stefanie Kälz. Anisotropic conduction in electrocardiology.

[24] John Canny. A computational approach to edge detection. *IEEE Transactions on pattern analysis and machine intelligence*, (6):679–698, 1986.

[25] Manuel D Cerqueira et al. Standardized myocardial segmentation and nomenclature for tomographic imaging of the heart. *Circulation*, 105(4):539–542, 2002.

[26] Ching Shyang Chen, Mahadevan Ganesh, Michael A Golberg, and AH-D Cheng. Multilevel compact radial functions based computational schemes for some elliptic problems. *Computers & Mathematics with Applications*, 43(3-5):359–378, 2002.

[27] Yufeng Chen, Fengxia Li, and Tianyu Huang. Curvature feature based shape analysis. In *International Conference on Intelligent Computing*, pages 414–421. Springer, 2008.

[28] Yunmei Chen and Xiaojing Ye. Inverse consistent deformable image registration. In *The Legacy of Alladi Ramakrishnan in the Mathematical Sciences*, pages 419–440. Springer, 2010.

[29] Andrew Chernih, Ian H Sloan, and Robert S Womersley. Wendland functions with increasing smoothness converge to a Gaussian. *Advances in Computational Mathematics*, 40(1):185–200, 2014.

[30] Toru Chikui, Makoto Obara, Arjan W Simonetti, Masahiro Ohga, Shoichi Koga, Shintaro Kawano, Yoshio Matsuo, Takeshi Kamintani, Tomoko Shiraishi, Erina Kitamoto, et al. The principal of dynamic contrast enhanced MRI, the method of pharmacokinetic analysis, and its application in the head and neck region. *International journal of dentistry*, 2012, 2012.

[31] Gary E Christensen and Hans J Johnson. Consistent image registration. *IEEE transactions on medical imaging*, 20(7):568–582, 2001.

[32] Ben R Dickie, Chris J Rose, Lucy E Kershaw, Stephanie B Withey, Bernadette M Carrington, Susan E Davidson, Gillian Hutchison, and Catharine ML West. The prognostic value of dynamic contrast-enhanced MRI contrast agent transfer constant Ktrans in cervical cancer is explained by plasma flow rather than vessel permeability. *British journal of cancer*, 116(11):1436, 2017.

[33] Gianluca Donato and Serge Belongie. Approximate thin plate spline mappings. In *European conference on computer vision*, pages 21–31. Springer, 2002.

[34] Marc Droske and Martin Rumpf. *A variational approach to non-rigid morphological registration*. Zentrum für Technomathematik, 2002.

[35] Jean Duchon. Splines minimizing rotation-invariant semi-norms in Sobolev spaces. In *Constructive theory of functions of several variables*, pages 85–100. Springer, 1977.

[36] Mehran Ebrahimi, Anthony Lausch, and Anne Martel. A Gauss–Newton approach to joint image registration and intensity correction. *Computer methods and programs in biomedicine*, 112(3):398–406, 2013.

[37] Mehran Ebrahimi and Anne Martel. A general PDE-framework for registration of contrast enhanced images. In *International Conference on Medical Image Computing and Computer-Assisted Intervention*, pages 811–819. Springer, 2009.

[38] Anders P Eriksson and Kalle Astrom. Bijective image registration using thin-plate splines. In *18th International Conference on Pattern Recognition (ICPR'06)*, volume 3, pages 798–801. IEEE, 2006.

[39] James R Ewing, Robert A Knight, Tavarekere N Nagaraja, John S Yee, Vijaya Nagesh, Polly A Whitton, Lian Li, and Joseph D Fenstermacher. Patlak plots of gd-dtpa mri data yield blood–brain transfer constants concordant with those of

14c-sucrose in areas of blood–brain opening. *Magnetic Resonance in Medicine: An Official Journal of the International Society for Magnetic Resonance in Medicine*, 50(2):283–292, 2003.

[40] Bernd Fischer and Jan Modersitzki. Combining landmark and intensity driven registrations. In *PAMM: Proceedings in Applied Mathematics and Mechanics*, volume 3, pages 32–35. Wiley Online Library, 2003.

[41] Bernd Fischer and Jan Modersitzki. Ill-posed medicine—an introduction to image registration. *Inverse Problems*, 24(3):034008, 2008.

[42] P Thomas Fletcher and Sarang Joshi. Principal geodesic analysis on symmetric spaces: Statistics of diffusion tensors. In *Computer Vision and Mathematical Methods in Medical and Biomedical Image Analysis*, pages 87–98. Springer, 2004.

[43] P Thomas Fletcher, Conglin Lu, and Sarang Joshi. Statistics of shape via principal geodesic analysis on Lie groups. In *Computer Vision and Pattern Recognition, 2003. Proceedings. 2003 IEEE Computer Society Conference on*, volume 1, pages I–I. IEEE, 2003.

[44] P Thomas Fletcher, Conglin Lu, Stephen M Pizer, and Sarang Joshi. Principal geodesic analysis for the study of nonlinear statistics of shape. *IEEE transactions on medical imaging*, 23(8):995–1005, 2004.

[45] Dimitra Flouri. *Tracer-Kinetic Model-Driven Motion Correction with Application to Renal DCE-MRI*. PhD thesis, University of Leeds, 2016.

[46] Mike Fornefett, Karl Rohr, and H Siegfried Stiehl. Elastic registration of medical images using radial basis functions with compact support. In *Proceedings. 1999 IEEE Computer Society Conference on Computer Vision and Pattern Recognition (Cat. No PR00149)*, volume 1, pages 402–407. IEEE, 1999.

[47] Jerome Friedman, Trevor Hastie, and Robert Tibshirani. *The elements of statistical learning*, volume 1. Springer series in statistics New York, 2001.

[48] Victoria Furer, Zahi A Fayad, Venkatesh Mani, Claudia Calcagno, Michael E Farkouh, and Jeffrey D Greenberg. Noninvasive cardiovascular imaging in rheumatoid arthritis: current modalities and the emerging role of magnetic resonance and positron emission tomography imaging. In *Seminars in arthritis and rheumatism*, volume 41, pages 676–688. Elsevier, 2012.

[49] Roberta Fusco, Mario Sansone, Silvio Maffei, Nicola Raiano, and Antonella Petrillo. Dynamic contrast-enhanced MRI in breast cancer: A comparison between distributed and compartmental tracer kinetic models. *Journal of Biomedical Graphics and Computing*, 2(2):23, 2012.

[50] Jean Gallier and Jocelyn Quaintance. Notes on differential geometry and lie groups. *University of Pennsylvannia*, 4:3–1, 2012.

[51] Wenshuo Gao, Xiaoguang Zhang, Lei Yang, and Huizhong Liu. An improved sobel edge detection. In *2010 3rd International conference on computer science and information technology*, volume 5, pages 67–71. IEEE, 2010.

[52] HP Gavin. The Levenberg-Marquardt algorithm for nonlinear least squares curve-fitting problems, 2019.

[53] Xiujuan Geng, Gary E Christensen, Hong Gu, Thomas J Ross, and Yihong Yang. Implicit reference-based group-wise image registration and its application to structural and functional MRI. *Neuroimage*, 47(4):1341–1351, 2009.

[54] Rafael C Gonzalez, Richard Eugene Woods, and Steven L Eddins. *Digital image processing using MATLAB*. Pearson Education India, 2004.

[55] Alexandre Guimond, Jean Meunier, and Jean-Philippe Thirion. Average brain models: A convergence study. *Computer vision and image understanding*, 77(2):192–210, 2000.

[56] Morton E Gurtin. *An introduction to continuum mechanics*, volume 158. Academic press, 1982.

[57] Patric Hagmann, Lisa Jonasson, Philippe Maeder, Jean-Philippe Thiran, Van J Wedeen, and Reto Meuli. Understanding diffusion MR imaging techniques: from scalar diffusion-weighted imaging to diffusion tensor imaging and beyond. *Radiographics*, 26(suppl_1):S205–S223, 2006.

[58] George Haller. Dynamic rotation and stretch tensors from a dynamic polar decomposition. *Journal of the Mechanics and Physics of Solids*, 86:70–93, 2016.

[59] Per Christian Hansen. *Discrete inverse problems: insight and algorithms*. SIAM, 2010.

[60] Christopher G Harris, Mike Stephens, et al. A combined corner and edge detector. In *Alvey vision conference*, volume 15, pages 10–5244. Citeseer, 1988.

[61] Patrick Helm, Mirza Faisal Beg, Michael I Miller, and Raimond L Winslow. Measuring and mapping cardiac fiber and laminar architecture using diffusion tensor MR imaging. *Annals of the New York Academy of Sciences*, 1047(1):296–307, 2005.

[62] Patrick A Helm. A novel technique for quantifying variability of cardiac anatomy: Application to the dyssynchronous failing heart. 2004.

[63] Patrick A Helm, Hsiang-Jer Tseng, Laurent Younes, Elliot R McVeigh, and Raimond L Winslow. Ex vivo 3D diffusion tensor imaging and quantification of cardiac laminar structure. *Magnetic resonance in medicine*, 54(4):850–859, 2005.

[64] Patrick A Helm, Laurent Younes, Mirza F Beg, Daniel B Ennis, Christophe Leclercq, Owen P Faris, Elliot McVeigh, David Kass, Michael I Miller, and Raimond L Winslow. Evidence of structural remodeling in the dyssynchronous failing heart. *Circulation research*, 98(1):125–132, 2006.

[65] Darren A Hooks, Karl A Tomlinson, Scott G Marsden, Ian J LeGrice, Bruce H Smaill, Andrew J Pullan, and Peter J Hunter. Cardiac microstructure: implications for electrical propagation and defibrillation in the heart. *Circulation research*, 91(4):331–338, 2002.

[66] EW Hsu, AL Muzikant, SA Matulevicius, RC Penland, and CS Henriquez. Magnetic resonance myocardial fiber-orientation mapping with direct histological correlation. *American Journal of Physiology-Heart and Circulatory Physiology*, 274(5):H1627–H1634, 1998.

[67] Zhaohui Huang and Fernand S Cohen. Affine-invariant b-spline moments for curve matching. *IEEE Transactions on image processing*, 5(10):1473–1480, 1996.

[68] TAGM Huisman. Diffusion-weighted and diffusion tensor imaging of the brain, made easy. *Cancer Imaging*, 10(1A):S163, 2010.

[69] Wyke Huizinga, Dirk HJ Poot, J-M Guyader, Remy Klaassen, Bram F Coolen, Matthijs van Kranenburg, RJM Van Geuns, André Uitterdijk, Mathias Polfliet, Jef Vandemeulebroucke, et al. PCA-based groupwise image registration for quantitative MRI. *Medical image analysis*, 29:65–78, 2016.

[70] MJA Jansen, HJ Kuijf, WB Veldhuis, FJ Wessels, MS Van Leeuwen, and JPW Pluim. Evaluation of motion correction for clinical dynamic contrast enhanced MRI of the liver. *Physics in Medicine & Biology*, 62(19):7556, 2017.

[71] Hangyi Jiang, Peter CM Van Zijl, Jinsuh Kim, Godfrey D Pearlson, and Susumu Mori. DTIStudio: resource program for diffusion tensor computation and fiber

bundle tracking. *Computer methods and programs in biomedicine*, 81(2):106–116, 2006.

[72] Jieqing Jiao, Graham E Searle, Andri C Tziortzi, Cristian A Salinas, Roger N Gunn, and Julia A Schnabel. Spatial-temporal pharmacokinetic model based registration of 4d brain pet data. In *International Workshop on Spatio-temporal Image Analysis for Longitudinal and Time-Series Image Data*, pages 100–112. Springer, 2012.

[73] Sarang Joshi, Brad Davis, Matthieu Jomier, and Guido Gerig. Unbiased diffeomorphic atlas construction for computational anatomy. *NeuroImage*, 23:S151–S160, 2004.

[74] Anthony Kanai and Guy Salama. Optical mapping reveals that repolarization spreads anisotropically and is guided by fiber orientation in guinea pig hearts. *Circulation Research*, 77(4):784–802, 1995.

[75] Minjeong Kim, Guorong Wu, and Dinggang Shen. Hierarchical alignment of breast DCE-MR images by groupwise registration and robust feature matching. *Medical physics*, 39(1):353–366, 2012.

[76] Peter B Kingsley. Introduction to diffusion tensor imaging mathematics: Part I. tensors, rotations, and eigenvectors. *Concepts in Magnetic Resonance Part A*, 28(2):101–122, 2006.

[77] Peter B Kingsley. Introduction to diffusion tensor imaging mathematics: Part II. anisotropy, diffusion-weighting factors, and gradient encoding schemes. *Concepts in Magnetic Resonance Part A*, 28(2):123–154, 2006.

[78] Peter B Kingsley. Introduction to diffusion tensor imaging mathematics: Part III. tensor calculation, noise, simulations, and optimization. *Concepts in Magnetic Resonance Part A*, 28(2):155–179, 2006.

[79] Kazuhiro Koshino, Hiroshi Watabe, Shinji Hasegawa, Takuya Hayashi, Jun Hatazawa, and Hidehiro Iida. Development of motion correction technique for cardiac 15 o-water pet study using an optical motion tracking system. *Annals of nuclear medicine*, 24(1):1–11, 2010.

[80] Ka Chun Lam and Lok Ming Lui. Landmark-and intensity-based registration with large deformations via quasi-conformal maps. *SIAM Journal on Imaging Sciences*, 7(4):2364–2392, 2014.

[81] Thomas Lange, Nils Papenberg, Stefan Heldmann, Jan Modersitzki, Bernd Fischer, Hans Lamecker, and Peter M Schlag. 3D ultrasound-CT registration of the liver using combined landmark-intensity information. *International journal of computer assisted radiology and surgery*, 4(1):79–88, 2009.

[82] Anthony Lausch. *Nonrigid registration of dynamic contrast-enhanced MRI data using motion informed intensity corrections.* PhD thesis, 2011.

[83] Anthony Lausch, Mehran Ebrahimi, and Anne Martel. Image registration for abdominal dynamic contrast-enhanced magnetic resonance images. In *Biomedical Imaging: From Nano to Macro, 2011 IEEE International Symposium on*, pages 561–565. IEEE, 2011.

[84] Keith S St Lawrence and Ting-Yim Lee. An adiabatic approximation to the tissue homogeneity model for water exchange in the brain: I. theoretical derivation. *Journal of Cerebral Blood Flow & Metabolism*, 18(12):1365–1377, 1998.

[85] Keith S St Lawrence and Ting-Yim Lee. An adiabatic approximation to the tissue homogeneity model for water exchange in the brain: II. experimental validation. *Journal of Cerebral Blood Flow & Metabolism*, 18(12):1378–1385, 1998.

[86] Jimmie Lawson and Yongdo Lim. Weighted means and Karcher equations of positive operators. *Proceedings of the National Academy of Sciences*, page 201313640, 2013.

[87] Denis Le Bihan and Peter Van Zijl. From the diffusion coefficient to the diffusion tensor. *NMR in Biomedicine: An International Journal Devoted to the Development and Application of Magnetic Resonance In Vivo*, 15(7-8):431–434, 2002.

[88] Mathieu Lepot, Jean-Baptiste Aubin, and François HLR Clemens. Interpolation in time series: An introductive overview of existing methods, their performance criteria and uncertainty assessment. *Water*, 9(10):796, 2017.

[89] Hui Li, BS Manjunath, and Sanjit K Mitra. A contour-based approach to multisensor image registration. *IEEE transactions on image processing*, 4(3):320–334, 1995.

[90] Sonia P Li, Anwar R Padhani, and Andreas Makris. Dynamic contrast-enhanced magnetic resonance imaging and blood oxygenation level-dependent magnetic resonance imaging for the assessment of changes in tumor biology with treatment. *Journal of the National Cancer Institute Monographs*, 2011(43):103–107, 2011.

[91] Mark E Lobatto, Claudia Calcagno, Josbert M Metselaar, Gert Storm, Erik SG Stroes, Zahi A Fayad, and Willem JM Mulder. Imaging the efficacy of anti-inflammatory liposomes in a rabbit model of atherosclerosis by non-invasive imaging. In *Methods in enzymology*, volume 508, pages 211–228. Elsevier, 2012.

[92] Herve Lombaert, Jean-Marc Peyrat, Pierre Croisille, Stanislas Rapacchi, Laurent Fanton, Farida Cheriet, Patrick Clarysse, Isabelle Magnin, Hervé Delingette, and Nicholas Ayache. Human atlas of the cardiac fiber architecture: study on a healthy population. *IEEE transactions on medical imaging*, 31(7):1436–1447, 2012.

[93] Richard GP Lopata, Walter H Backes, Paul PJ van Den Bosch, and Natal AW van Riel. On the identifiability of pharmacokinetic parameters in dynamic contrast-enhanced imaging. *Magnetic Resonance in Medicine: An Official Journal of the International Society for Magnetic Resonance in Medicine*, 58(2):425–429, 2007.

[94] Lok Wan Lorraine Ma. *Mathematical methods for 2D-3D cardiac image registration.* PhD thesis, 2016.

[95] Frederik Maes, Andre Collignon, Dirk Vandermeulen, Guy Marchal, and Paul Suetens. Multimodality image registration by maximization of mutual information. *IEEE transactions on Medical Imaging*, 16(2):187–198, 1997.

[96] JB Antoine Maintz and Max A Viergever. An overview of medical image registration methods. In *Symposium of the Belgian hospital physicists association (SBPH/BVZF)*, volume 12, pages 1–22. Citeseer, 1996.

[97] Timo Makela, Patrick Clarysse, Outi Sipila, Nicoleta Pauna, Quoc Cuong Pham, Toivo Katila, and Isabelle E Magnin. A review of cardiac image registration methods. *IEEE Transactions on medical imaging*, 21(9):1011–1021, 2002.

[98] A Martel, MS Froh, KK Brock, DB Plewes, and DC Barber. Evaluating an optical-flow-based registration algorithm for contrast-enhanced magnetic resonance imaging of the breast. *Physics in Medicine & Biology*, 52(13):3803, 2007.

[99] Anne L Martel. A fast method of generating pharmacokinetic maps from dynamic contrast-enhanced images of the breast. In *International Conference on Medical Image Computing and Computer-Assisted Intervention*, pages 101–108. Springer, 2006.

[100] Asif Masood, Adil Masood Siddiqui, and Muhammad Saleem. A radial basis function for registration of local features in images. In *Pacific-Rim Symposium on Image and Video Technology*, pages 651–663. Springer, 2007.

[101] James Mattiello, Peter J Basser, and Denis Le Bihan. The b matrix in diffusion tensor echo-planar imaging. *Magnetic Resonance in Medicine*, 37(2):292–300, 1997.

[102] Medixant. Radiant dicom viewer. `https://www.radiantviewer.com`.

[103] A Melbourne, D Atkinson, MJ White, D Collins, M Leach, and D Hawkes. Registration of dynamic contrast-enhanced MRI using a progressive principal component registration (PPCR). *Physics in Medicine & Biology*, 52(17):5147, 2007.

[104] Robert Mifflin and Claudia Sagastizábal. A vu-algorithm for convex minimization. *Mathematical programming*, 104(2-3):583–608, 2005.

[105] Michael I Miller, Alain Trouvé, and Laurent Younes. On the metrics and Euler-Lagrange equations of computational anatomy. *Annual review of biomedical engineering*, 4(1):375–405, 2002.

[106] Jan Modersitzki. *Numerical methods for image registration*. Oxford University Press on Demand, 2004.

[107] Jan Modersitzki. *FAIR: flexible algorithms for image registration*, volume 6. SIAM, 2009.

[108] Mia Mojica and Mehran Ebrahimi. An unbiased groupwise registration algorithm for correcting motion in dynamic contrast-enhanced magnetic resonance images. In *Image Analysis for Moving Organ, Breast, and Thoracic Images*, pages 42–52. Springer, 2018.

[109] Mia Mojica and Mehran Ebrahimi. A hybrid landmark and contour-matching image registration model. *Journal of Computational Vision and Imaging Systems*, 6(1):1–4, 2020.

[110] Mia Mojica and Mehran Ebrahimi. Motion correction in dynamic contrast-enhanced magnetic resonance images using pharmacokinetic modeling. In *Med-*

ical Imaging 2021: Image Processing, volume 11596, page 115962S. International Society for Optics and Photonics, 2021.

[111] Mia Mojica, Mihaela Pop, and Mehran Ebrahimi. Automatic detection of landmarks for fast cardiac MR image registration. In *International Workshop on Statistical Atlases and Computational Models of the Heart*, pages 87–96. Springer, 2020.

[112] Mia Mojica, Mihaela Pop, Maxime Sermesant, and Mehran Ebrahimi. Multilevel non-parametric groupwise registration in cardiac MRI: Application to explanted porcine hearts. In *International Workshop on Statistical Atlases and Computational Models of the Heart*, pages 60–69. Springer, 2017.

[113] Mia Mojica, Mihaela Pop, Maxime Sermesant, and Mehran Ebrahimi. Constructing an average geometry and diffusion tensor magnetic resonance field from freshly explanted porcine hearts. In *Medical Imaging 2019: Image Processing*, volume 10949, page 109493C. International Society for Optics and Photonics, 2019.

[114] Mia Mojica, Mihaela Pop, Maxime Sermesant, and Mehran Ebrahimi. Novel atlas of fiber directions built from ex-vivo diffusion tensor images of porcine hearts. *Computer Methods and Programs in Biomedicine*, 187:105200, 2020.

[115] Farzin Mokhtarian. Silhouette-based isolated object recognition through curvature scale space. *IEEE Transactions on Pattern Analysis and Machine Intelligence*, 17(5):539–544, 1995.

[116] Michael Mongillo. Choosing basis functions and shape parameters for radial basis function methods. *SIAM undergraduate research online*, 4(190-209):2–6, 2011.

[117] Todd K Moon. The expectation-maximization algorithm. *IEEE Signal processing magazine*, 13(6):47–60, 1996.

[118] Susumu Mori and Jiangyang Zhang. Principles of diffusion tensor imaging and its applications to basic neuroscience research. *Neuron*, 51(5):527–539, 2006.

[119] Pratik Mukherjee, JI Berman, SW Chung, CP Hess, and RG Henry. Diffusion tensor MR imaging and fiber tractography: theoretic underpinnings. *American journal of neuroradiology*, 29(4):632–641, 2008.

[120] Marrick C Neri. Primal-dual methods in total variation regularized l_1 and l_2 functionals arising in image denoising. 2008.

[121] PM Nielsen, IJ Le Grice, BH Smaill, and PJ Hunter. Mathematical model of geometry and fibrous structure of the heart. *American Journal of Physiology-Heart and Circulatory Physiology*, 260(4):H1365–H1378, 1991.

[122] Jorge Nocedal and Stephen Wright. *Numerical optimization*. Springer Science & Business Media, 2006.

[123] JPB O'Connor, PS Tofts, KA Miles, LM Parkes, G Thompson, and A Jackson. Dynamic contrast-enhanced imaging techniques: CT and MRI. *The British journal of radiology*, 84(special_issue_2):S112–S120, 2011.

[124] Lauren J O'Donnell and Carl-Fredrik Westin. An introduction to diffusion tensor image analysis. *Neurosurgery Clinics*, 22(2):185–196, 2011.

[125] Clifford S Patlak, Ronald G Blasberg, and Joseph D Fenstermacher. Graphical evaluation of blood-to-brain transfer constants from multiple-time uptake data. *Journal of Cerebral Blood Flow & Metabolism*, 3(1):1–7, 1983.

[126] Xavier Pennec. Barycentric subspaces and affine spans in manifolds. In *International Conference on Networked Geometric Science of Information*, pages 12–21. Springer, 2015.

[127] Xavier Pennec, Nicholas Ayache, and Jean-Philippe Thirion. Landmark-based registration using features identified through differential geometry, 2000.

[128] William D Penny, Karl J Friston, John T Ashburner, Stefan J Kiebel, and Thomas E Nichols. *Statistical parametric mapping: the analysis of functional brain images*. Elsevier, 2011.

[129] Jean-Marc Peyrat, Maxime Sermesant, Xavier Pennec, Hervé Delingette, Chenyang Xu, Elliot R McVeigh, and Nicholas Ayache. A computational framework for the statistical analysis of cardiac diffusion tensors: application to a small database of canine hearts. *IEEE transactions on medical imaging*, 26(11):1500–1514, 2007.

[130] Emmanuel Piuze, Paul G Kry, and Kaleem Siddiqi. Generalized helicoids for modeling hair geometry. In *Computer Graphics Forum*, volume 30, pages 247–256. Wiley Online Library, 2011.

[131] Emmanuel Piuze, Herve Lombaert, Jon Sporring, Gustav J Strijkers, Adrianus J Bakermans, and Kaleem Siddiqi. Atlases of cardiac fiber differential geometry. In *International Conference on Functional Imaging and Modeling of the Heart*, pages 442–449. Springer, 2013.

[132] Emmanuel Piuze, Jon Sporring, and Kaleem Siddiqi. Moving frames for heart fiber geometry. In *International Conference on Information Processing in Medical Imaging*, pages 524–535. Springer, 2013.

[133] Emmanuel Piuze-Phaneuf. *The Geometry of Cardiac Myofibers*. PhD thesis, McGill University Libraries, 2015.

[134] Mihaela Pop, Nilesh R Ghugre, Venkat Ramanan, Lily Morikawa, Greg Stanisz, Alexander J Dick, and Graham A Wright. Quantification of fibrosis in infarcted swine hearts by ex vivo late gadolinium-enhancement and diffusion-weighted MRI methods. *Physics in medicine and biology*, 58(15):5009, 2013.

[135] Mihaela Pop, Maxime Sermesant, Damien Lepiller, Michael V Truong, Elliot R McVeigh, Eugene Crystal, Alexander Dick, Herve Delingette, Nicholas Ayache, and Graham A Wright. Fusion of optical imaging and MRI for the evaluation and adjustment of macroscopic models of cardiac electrophysiology: a feasibility study. *Medical image analysis*, 13(2):370–380, 2009.

[136] Mihaela Pop, Maxime Sermesant, Garry Liu, Jatin Relan, Tommaso Mansi, Alan Soong, Jean-Marc Peyrat, Michael V Truong, Paul Fefer, Elliot R McVeigh, et al. Construction of 3D MR image-based computer models of pathologic hearts, augmented with histology and optical fluorescence imaging to characterize action potential propagation. *Medical image analysis*, 16(2):505–523, 2012.

[137] Mihaela Pop, Maxime Sermesant, Tommaso Mansi, Eugene Crystal, Sudip Ghate, Jean-Marc Peyrat, Ilan Lashevsky, Beiping Qiang, Elliot McVeigh, Nicholas Ayache, et al. Correspondence between simple 3-D MRI-based computer models and in-vivo EP measurements in swine with chronic infarctions. *IEEE Transactions on Biomedical Engineering*, 58(12):3483, 2011.

[138] V Rajagopalan, Z Jiang, J Stojanovic-Radic, GH Yue, EP Pioro, et al. Ea basic introduction to diffusion tensor imaging mathematics and image processing steps. *Brain Disord Ther*, 6(229):2, 2017.

[139] Timothy Owen Ramsay. A bivariate finite element smoothing spline applied to image registration. 2001.

[140] Marc-Michel Rohé, Maxime Sermesant, and Xavier Pennec. Low-dimensional representation of cardiac motion using barycentric subspaces: A new group-wise paradigm for estimation, analysis, and reconstruction. *Medical image analysis*, 45:1–12, 2018.

[141] Karl Rohr, H Siegfried Stiehl, Rainer Sprengel, Thorsten M Buzug, Jürgen Weese, and MH Kuhn. Landmark-based elastic registration using approximating thin-plate splines. *IEEE Transactions on medical imaging*, 20(6):526–534, 2001.

[142] Idan Roifman, Nilesh R Ghugre, Tasnim Vira, Mohammad I Zia, Anna Zavodni, Mihaela Pop, Kim A Connelly, and Graham A Wright. Assessment of the longitudinal changes in infarct heterogeneity post myocardial infarction. *BMC cardiovascular disorders*, 16(1):198, 2016.

[143] Dan Ruan, Jeffrey A Fessler, Michael Roberson, James Balter, and Marc Kessler. Nonrigid registration using regularization that accommodates local tissue rigidity. In *Medical Imaging 2006: Image Processing*, volume 6144, page 614412. International Society for Optics and Photonics, 2006.

[144] Frank Sauer. Image registration: enabling technology for image guided surgery and therapy. In *2005 IEEE engineering in medicine and biology 27th annual conference*, pages 7242–7245. IEEE, 2006.

[145] Annarita Savi, Maria Carla Gilardi, Giovanna Rizzo, Mauro Pepi, Claudio Landoni, Claudio Rossetti, Giovanni Lucignani, Antonio Bartorelli, and Ferruccio Fazio. Spatial registration of echocardiographic and positron emission tomographic heart studies. *European journal of nuclear medicine*, 22(3):243–247, 1995.

[146] Robert Schaback. A practical guide to radial basis functions. *Electronic Resource*, 11:1–12, 2007.

[147] Otmar Scherzer. *Handbook of mathematical methods in imaging*. Springer Science & Business Media, 2010.

[148] David F Scollan, Alex Holmes, Raimond Winslow, and John Forder. Histological validation of myocardial microstructure obtained from diffusion tensor magnetic

resonance imaging. *American Journal of Physiology-Heart and Circulatory Physiology*, 275(6):H2308–H2318, 1998.

[149] Zhimin Shao and Josef Kittler. Estimating angles and curvature features in grey scale images. In *BMVC*, pages 1–10, 1994.

[150] Robin Sibson and Glenn Stone. Computation of thin-plate splines. *SIAM Journal on Scientific and Statistical Computing*, 12(6):1304–1313, 1991.

[151] Irwin Sobel and Gary Feldman. A 3x3 isotropic gradient operator for image processing. *a talk at the Stanford Artificial Project in*, pages 271–272, 1968.

[152] Aristeidis Sotiras, Nikos Paragios, et al. Deformable image registration: a survey. *Rapport de recherche RR-7919, INRIA*, 2012.

[153] Yin Sun, Chye Hwang Yan, Sim-Heng Ong, Ek Tsoon Tan, and Shih-Chang Wang. Intensity-based volumetric registration of contrast-enhanced MR breast images. In *International Conference on Medical Image Computing and Computer-Assisted Intervention*, pages 671–678. Springer, 2006.

[154] Yoriyasu Suzuki, Alan C Yeung, and Fumiaki Ikeno. The representative porcine model for human cardiovascular disease. *BioMed Research International*, 2011, 2010.

[155] Salvatore Tabbone and CI Lorraine. Corner detection using laplacian of gaussian operator. In *Proceedings of the Scandinavian Conference on Image Analysis*, volume 2, pages 1055–1055. Citeseer, 1993.

[156] Abdel Aziz Taha and Allan Hanbury. Metrics for evaluating 3D medical image segmentation: analysis, selection, and tool. *BMC medical imaging*, 15(1):29, 2015.

[157] Lisa Tang, Ghassan Hamarneh, and K Iniewski. Medical image registration: A review. *Medical imaging: technology and applications*, 1:619–660, 2013.

[158] Paul S Tofts. Modeling tracer kinetics in dynamic Gd-DTPA MR imaging. *Journal of magnetic resonance imaging*, 7(1):91–101, 1997.

[159] Paul S Tofts, Bruce Berkowitz, and Mitchell D Schnall. Quantitative analysis of dynamic Gd-DTPA enhancement in breast tumors using a permeability model. *Magnetic resonance in medicine*, 33(4):564–568, 1995.

[160] Paul S Tofts, Gunnar Brix, David L Buckley, Jeffrey L Evelhoch, Elizabeth Henderson, Michael V Knopp, Henrik BW Larsson, Ting-Yim Lee, Nina A Mayr, Geoffrey JM Parker, et al. Estimating kinetic parameters from dynamic contrast-enhanced T1-weighted MRI of a diffusable tracer: standardized quantities and symbols. *Journal of Magnetic Resonance Imaging: An Official Journal of the International Society for Magnetic Resonance in Medicine*, 10(3):223–232, 1999.

[161] Paul S Tofts and Allan G Kermode. Measurement of the blood-brain barrier permeability and leakage space using dynamic MR imaging. 1. fundamental concepts. *Magnetic resonance in medicine*, 17(2):357–367, 1991.

[162] P.S. Tofts. T1-weighted DCE imaging concepts: Modelling, acquisition and analysis. *MAGNETOM Flash*, 3:30–39, 01 2010.

[163] Carlo Tomasi and Takeo Kanade. Detection and tracking of point features. 1991.

[164] Nicolas Toussaint, Maxime Sermesant, Christian T Stoeck, Sebastian Kozerke, and Philip G Batchelor. In vivo human 3D cardiac fibre architecture: reconstruction using curvilinear interpolation of diffusion tensor images. In *International Conference on Medical Image Computing and Computer-Assisted Intervention*, pages 418–425. Springer, 2010.

[165] Nicolas Toussaint, Jean-Christophe Souplet, Pierre Fillard, et al. Medinria: Medical image navigation and research tool by INRIA. In *Proc. of MICCAI*, volume 7, page 280, 2007.

[166] Nicolas Toussaint, Christian T Stoeck, Tobias Schaeffter, Sebastian Kozerke, Maxime Sermesant, and Philip G Batchelor. In vivo human cardiac fibre architecture estimation using shape-based diffusion tensor processing. *Medical image analysis*, 17(8):1243–1255, 2013.

[167] David S Trossman, LuAnne Thompson, and Susan L Hautala. Application of thin-plate splines in two dimensions to oceanographic tracer data. *Journal of Atmospheric and Oceanic Technology*, 28(11):1522–1538, 2011.

[168] Wen-Yih I Tseng, Van J Wedeen, Timothy G Reese, R Neal Smith, and Elkan F Halpern. Diffusion tensor MRI of myocardial fibers and sheets: correspondence with visible cut-face texture. *Journal of Magnetic Resonance Imaging: An Official Journal of the International Society for Magnetic Resonance in Medicine*, 17(1):31–42, 2003.

[169] Piotr Urban. *Investigation of Intensity Correction in the Context of Image Registration*. PhD thesis, University of Central Lancashire, 2010.

[170] Wim Van Hecke, Louise Emsell, and Stefan Sunaert. *Diffusion tensor imaging: a practical handbook*. Springer, 2015.

[171] Catherina SP van Rijswijk, Edwin van der Linden, Henk-Jan van der Woude, Jari M van Baalen, and Johan L Bloem. Value of dynamic contrast-enhanced mr imaging in diagnosing and classifying peripheral vascular malformations. *American Journal of Roentgenology*, 178(5):1181–1187, 2002.

[172] Tom Vercauteren, Xavier Pennec, Aymeric Perchant, and Nicholas Ayache. Symmetric log-domain diffeomorphic registration: A demons-based approach. *Medical Image Computing and Computer-Assisted Intervention–MICCAI 2008*, pages 754–761, 2008.

[173] Anna Vilanova, Song Zhang, Gordon Kindlmann, and D Laidlaw. An introduction to visualization of diffusion tensor imaging and its applications. *Visualization and Processing of Tensor Fields*, pages 121–153, 2006.

[174] Christian Wachinger and Nassir Navab. Entropy and Laplacian images: Structural representations for multi-modal registration. *Medical image analysis*, 16(1):1–17, 2012.

[175] Grace Wahba. *Spline models for observational data*, volume 59. Siam, 1990.

[176] Yue Wang and Eam Khwang Teoh. 2d affine-invariant contour matching using b-spline model. *IEEE Transactions on Pattern Analysis and Machine Intelligence*, 29(10):1853–1858, 2007.

[177] Joachim Weickert and Christoph Schnörr. A theoretical framework for convex regularizers in PDE-based computation of image motion. *International Journal of Computer Vision*, 45(3):245–264, 2001.

[178] Eric W. Weisstein. Shear. `https://mathworld.wolfram.com/Shear.html`. Accessed: 1-December-2020.

[179] Holger Wendland. Piecewise polynomial, positive definite and compactly supported radial functions of minimal degree. *Advances in computational Mathematics*, 4(1):389–396, 1995.

[180] Ruiyi Wu, Song Zhang, and Allen Crow. Towards constructing a fiber bundle atlas on porcine hearts with diffusion tensor imaging.

[181] Paul A. Yushkevich, Joseph Piven, Heather Cody Hazlett, Rachel Gimpel Smith, Sean Ho, James C. Gee, and Guido Gerig. User-guided 3D active contour segmentation of anatomical structures: Significantly improved efficiency and reliability. *Neuroimage*, 31(3):1116–1128, 2006.

[182] Dengsheng Zhang and Guojun Lu. A comparison of shape retrieval using fourier descriptors and short-time fourier descriptors. In *Pacific-Rim Conference on Multimedia*, pages 855–860. Springer, 2001.